UNIVERSIDAD NACIONAL AUTONOMA DE MEXICO
PROGRAMA DE POSGRADO EN ASTROFISICA
Instituto de Radioastronomía y Astrofísica

Dust around late WN stars as a fingerprint of the stellar evolution

Polvo en el entorno de las estrellas WN tardías como

firma de evolución estelar

Tesis
Para optar por el grado de

Doctor en Ciencias
(Astrofísica)

Presenta
Palmira Jiménez Hernández

Tutores
Dra. S. Jane Arthur, Instituto de Radioastronomía y Astrofísica
Dr. Jesús A. Toalá, Instituto de Radioastronomía y Astrofísica

Morelia, Michoacán Septiembre del 2022

Resumen

Las estrellas Wolf-Rayet (WR) son muy calientes y luminosas, además sus espectros están caracterizados por líneas de emisión anchas que indican la presencia de vientos fuertes y rápidos. El cociente de estas líneas es clásicamente usado para la subclasificación de las estrellas WR en: WN (ricas en nitrógeno), WC (ricas en carbono), y WO (ricas en oxígeno). Las estrellas WN que presentan líneas de emisión de hidrógeno son etiquetadas como WNh y se distinguen por ser las más luminosas. Actualmente se acepta que las estrellas WR clásicas son descendientes de las estrellas masivas tipo O en una etapa evolutiva avanzada.

Algunas estrellas WNh tipo tardías (con fracciones de Hidrógeno $X_H \lesssim 40\,\%$) están rodeadas por nebulosas, lo que sugiere que se formaron mediante un episodio violento de pérdida de masa. Las propiedades del material nebular pueden ser usadas para inferir la historia de pérdida de masa de estrellas masivas en las últimas etapas de su evolución.

En esta tesis usamos observaciones de telescopios IR de *WISE*, *Spitzer* y *Herschel* para construir las distribuciones espectrales de energía (SED's por sus siglas en inglés) de M 1-67 y RCW 58, las cuales rodean a WR 124 y WR 40, estrellas WN 8h. Modelando con el código de síntesis espectral CLOUDY mostramos que en ambas nebulosas las SED infrarrojas y las propiedades del gas ionizado pueden reproducirse con una cáscara de polvo constituido por dos poblaciones de granos de polvo y con una razón de masa de polvo a gas alta.

El tamaño más grande de granos en ambas nebulosas, es tan grande como 0.9 μm, y la distribución del material nebular sugiere una historia en común de formación de polvo eruptiva para ambos objetos. Tomando en cuenta la masa inicial estimada de las estrellas centrales, la morfología y la cinématica de las nebulosas, proponemos que M 1-67 y RCW 58 pueden representar las primeras evidencias observacionales de un escenario post- envolvente común en estrellas masivas. Lo anterior, debido a que la evolución de la envolvente común (CE, por sus siglas en inglés) puede resultar en la eyección de la CE y una binaria compacta. Cabe recalcar que la posibilidad de que WR 124 y WR 40 tengan una compañera binaria oculta por sus fuertes vientos no ha sido descartado en la literatura actual.

A partir de los resultados obtenidos del modelado con CLOUDY, mostramos nuestra investigación (aún en desarrollo) empleando simulaciones hidródinamicas desarrolladas con el código de evolución estelar MESA. En este estudio examinamos las propiedades dinámicas de objetos con envolvente común durante la fase *slow spiral-in* usando modelos 1D de calentamiento por disipación orbital. En esta investigación se buscan las

condiciones bajo las cuales el objeto, una estrella binaria masiva que evolucione por una CE, puede eyectar la masa suficiente para formar nebulosas como M 1-67 y RCW 58.

Este documento está constituido por un total de 7 capítulos. En el Capítulo 1 presentamos una breve introducción donde se describen las estrellas WR como fase evolutiva tardía de estrellas masivas, así como las nebulosas que se pueden observar alrededor de ellas. El Capítulo 2 describe las observaciones y la manera en como fueron usadas en este trabajo. A continuación, en el Capítulo 3 se describe la forma de empleo de CLOUDY y la libreria de python PYCLOUDY para modelar las propiedades del las nebulosas WR estudiadas. Los Capítulos 4 y 5 presentan el modelado detallado y los resultado obtenidos de las nebulosas M 1-67 y RCW 58, respectivamente. En el Capítulo 6 se exponen los modelos y resultados preliminares de las simulaciones hidrodinámicas de los objetos CE elaboradas con MESA. Finalmente, el Capítulo 7 expone las conclusiones y el panorama general de acuerdo a nuestros resultados del proyecto.

Abstract

Wolf-Rayet (WR) stars are very hot and luminous, and their spectra are characterized by broad emission lines that indicate the presence of strong and fast winds. The ratio of these lines is classically used for the subclassification of WR stars into: WN (Nitrogen-rich), WC (Carbon-rich), and WO (Oxygen-rich). WN stars that exhibit hydrogen emission lines are labeled WNh and are distinguished by being the most luminous. It is now accepted that classical WR stars are descendants of massive O-type stars at an advanced evolutionary stage.

Some late-type WNh stars (with fractions of Hydrogen $X_H \lesssim 40\%$) are surrounded by nebulae, suggesting that they were formed by a violent episode of mass loss. The properties of the nebular material can be used to infer the mass loss histories of massive stars in the later stages of their evolution.

In this thesis, we use IR telescope observations from *WISE*, *Spitzer* and *Herschel* to construct the spectral energy distributions (SED's) of M 1-67 and RCW 58, which surround the WN8h stars WR 124 and WR 40. Modelling with the spectral synthesis code CLOUDY we show that in both nebulae the infrared SEDs and ionized gas properties can be reproduced by a dust shell consisting of two populations of dust grains and with a high dust-to-gas mass ratio.

The largest grain size in both nebulae is as large as 0.9 μm, and the distribution of nebular material suggests a common history of eruptive dust formation for both objects. Taking into account the estimated initial mass of the central stars, the morphology and the kinematics of the nebulae, we propose that M 1-67 and RCW 58 may represent the first observational evidence of a post- Common Envelope scenario in massive stars. This is because the evolution of the common envelope (CE) can result in the ejection of the CE and a compact binary. It should be noted that the possibility that WR 124 and WR 40 have a binary companion hidden by their strong winds has not been ruled out in the current literature.

From the results obtained from CLOUDY modelling, we show our research (still under development) using hydrodynamic simulations developed with the stellar evolution code MESA. In this study, we examine the dynamical properties of common envelope objects during the *slow spiral-in* phase using 1D models of orbital dissipative heating. In this investigation, the conditions under which the object, a massive binary star evolving by a CE, can eject enough mass to form nebulae such as M 1-67 and RCW 58 are sought.

This document consists of a total of 7 chapters. In Chapter 1 we present a brief introduction where WR stars are described as late evolutionary phase of massive stars, as well as the nebulae that can be observed around them. Chapter 2 describes the

observations and how they were used in this work. Next, Chapter 3 describes how to use CLOUDY and the python library PYCLOUDY to model the properties of the WR nebulae studied. Chapters 4 and 5 present the detailed modelling and the results obtained for the nebulae M 1-67 and RCW 58, respectively. In Chapter 6 the models and preliminary results of the hydrodynamic simulations of CE objects elaborated with MESA are presented. Finally, Chapter 7 presents the conclusions and the general panorama according to our project results.

Acknowledgments

To my family,
parents, brother and sister-in-law, who supported me all the time.

To my advisors,
I would like to thank Dra. Jane Arthur and Dr. Jesus Toalá for their support and guidance during this research.

To thesis jury,
I am very grateful to Dr. Anthony P. Marston, Dr. Christophe Roger Morisset, Dra. Gloria Koenigsberger Horowitz, Dr. Sundar Srinivasan and, Dra. Mónica Rodríguez Guillén for their comments that have improved this document.

To my friends,
I am most grateful to my IRyA friends and CCM friend, who supported me hard.

To IRyA-UNAM,
to those who make up the staff of the institute.

To CONACyT,
I would like to acknowledge the financial support by a research student grant.

To DGAPA-UNAM-PAPIIT,
I am grateful for the financial support provided by the grants IA100720 and IN107019.

Contents

1   Introduction

1.1   Evolution of massive stars

The evolution of massive stars, with an initial mass above 8 $M_\odot$, is strongly sensitive to the mass, metallicity, and multiplicity of the system. The mass-loss rate and rotation are the main parameters that determine the evolutionary track of the star because they change its initial mass and surface abundance. These physical parameters dominate the evolution of the star at masses below 30 $M_\odot$ (e.g. Maeder & Meynet, 2000). However, as the star becomes more massive (above 30 $M_\odot$), its evolution is dictated mainly by mass loss (e.g. Langer, 2012; Vink & Gräfener, 2012). In this thesis, we have a particular interest in Wolf-Rayet (WR) stars, which represent the most advanced evolutionary stage of very massive stars with initial mass $M_i \gtrsim 25$ $M_\odot$, prior to supernova explosion (Langer, 1995; Ekström et al., 2012).

From evolutionary models we know that mass determines lifetime during the Main Sequence (MS) and the final phases of the star; consequently, changes in the star's mass should not be ignored when modelling the star's evolution. There are two different mass-loss processes in single massive stars according to their evolutionary state: Wind mechanisms and dynamical mass loss mechanisms. In wind mechanisms, a star exerts radiation pressure on the material in its atmosphere (gas or dust) and produces constant outflows that remove matter from the star's surface. On the other hand, dynamical mass loss originates from wave-driven eruptions and pulsations and produces inertial, semi-ballistic outflows, which are launched in violent and short ejection events (Smith, 2014). In addition, massive stars in binary systems that are undergoing Roche-Lobe Overflow (RLOF) can lose large amounts of mass through mass transfer at late evolutionary stages.

Mass loss is important at all stages of a massive star's life since it not only affects the evolution of the stars themselves but also interacts with the circumstellar environment. In the single massive star scenario an O star spends a few 10^6 years in MS. In this stage, stars exhibit stellar winds driven by radiation pressure on UV lines which can cause the star to lose up to 10 $M_\odot$ (Ekström et al., 2012). Furthermore, because of its high ionizing photon flux, the interstellar medium (ISM) around such stars is photoionized. Both effects, wind and ionizing photons result in a stellar wind bubble surrounded by an H II region.

According to its initial mass, a star can go down different evolutionary paths. After finishing the MS phase, O stars with initial masses 25 $M_\odot < M_i < 60$ $M_\odot$ evolve into a

red supergiant (RSG) stage. A RSG star is cooler than its previous stage and exhibits slow (10–30 km s^{-1}) and dense winds with $\dot{M} = 10^{-7} - 10^{-4}$ M$_\odot$ yr^{-1} (Beasor & Davies, 2018, and references therein). However, O stars with initial masses $M_i > 60$M$_\odot$ evolve into a relatively hot star called a luminous blue variable (LBV) star (Georgy et al., 2012). In this stage, because of its high luminosity, the LBV star experiences eruptive mass-loss episodes with $\dot{M} \gtrsim 10^{-3}$ M$_\odot$ yr^{-1} (Bohannan, 1997; Weis, 2001, and references therein). The evolutionary stages after MS are shorter, RSG stars have a life of $\sim 10^5$ years and LBVs only $\sim 10^4$ years. The star continually loses mass during the RSG or LBV phase and when the star loses its hydrogen-rich envelope and exposes its He-rich core, it becomes a WR star. This phase lasts $\sim 10^5$ years. WR stars are characterized by their powerful line-driven winds ($v_\infty > 1000$ km s^{-1}, $\dot{M} \approx 10^{-5}$ M$_\odot$ yr^{-1}; Hamann et al., 2006) and high number of ionizing photons for H ($Q_H > 5 \times 10^{48}$ s^{-1}). A WR star can photoionize its surroundings and sweeps up the material ejected in previous evolutionary phases (Garcia-Segura & Mac Low, 1995). In the end, the WR star will end its life as a type Ib or Ic supernova (Crowther, 2007).

From the above, depending on the initial parameters (initial mass, metallicity, rotation, etc.) single massive stars go through different evolutionary stages (e.g. Crowther, 2007), however, we can summarize those possible evolutionary scenarios in a general outline:

$$O \rightarrow \text{LBV / RSG} \rightarrow \text{WR} \rightarrow \text{SN Ib/c}\ ^{[1]}.$$

Since most O stars are born in star-forming regions, it is common to find them in binary and multiple systems. Sana et al. (2012) estimated that over 70% of O stars are in these types of systems. The proximity between the components that make up these systems can give rise to an interaction between them during their evolution. For example, in the binary scenario, when a close binary exhibits Roche lobe overflow, it transfers mass from the primary to the secondary; this process alters the lifetime and evolutionary trajectories of both stars (e.g. Paczyński, 1976; van den Heuvel & Heise, 1972; de Mink et al., 2014). In some cases, mass transfer via Roche lobe overflow can lead (depending on the luminosity ratio [L_2/L_1], orbital period, orbital velocities, etc.) to one of the components becoming a WR star (e.g. Wellstein, Langer & Braun, 2001).

1.2 WR stars

Wolf-Rayet stars are characterized by being very hot ($T_{\text{eff}} = 30 - 140$ K) and luminous (L$\sim 10^4 - 10^6 L_\odot$), and have strong stellar winds. Their high velocities and mass-loss rate are estimated from P-Cygni profiles in UV, optical, near-infrared (near-IR) and mid-infrared (mid-IR). Depending on the predominance of nitrogen, carbon and oxygen emission lines, WR stars are divided into a nitrogen sequence (WN stars), a carbon

---

1 Conti scenario (Conti, 1975)

sequence (WC stars) and an oxygen sequence (WO). Comparing physical properties and ratios between WR sequences it has been suggested that they are consecutive evolutionary stages, that is: WN → WC → WO.

WN-type stars are considered the first phase of the WR stage. Furthermore, WN stars are subdivided into early-type (WNE) and late-type (WNL), with Hydrogen abundances X_H 10% and X_H 40%, respectively. If the spectrum of the star shows hydrogen emission lines it is called WNh, but if it also exhibits hydrogen absorption lines it is called WNha.

Stellar winds reveal the products of the burning process of the O-type star during its evolution, so, when the star enters into a WR phase after passing through the RSG/LBV phase its surface is H-depleted. Consequently, many authors have considered WN stars which show features of hydrogen in their spectrum as an intermediate phase between MS (O-type star) and LBV phases, for stars with $M_i \gtrsim 75\ M_\odot$ (see Crowther, 2007, and references therein). This evolutionary sequence is suggested to be:

$$O \rightarrow WN\ (\text{H-rich}) \rightarrow LBV \rightarrow WN(\text{H-poor}) \rightarrow WC \rightarrow SN\ I/c.$$

1.2.1 Wolf-Rayet nebulae

In many cases, the interaction between ionizing photons from the WR star with circumstellar material produces optically visible WR nebulae. WR nebulae have been characterized through optical images and spectra. Narrow-band filter images have been used to classify their [O III], Hα and [N II] morphologies into three broad classes: H II regions, ejecta nebulae, and wind-blown bubbles (Chu, 1981). In particular, the ejecta nebulae have clumpy or irregular nebulosity suggesting a violent mass-loss episode and are mainly associated with the late WNh spectral type (Stock & Barlow, 2010), that is, the hydrogen envelope is not completely lost.

When the WR star is immersed in a dense environment, its associated nebula is composed of stellar material ejected in previous stages of the star and swept-up interstellar material. On the other hand, if the star is surrounded by a low-density medium, the associated WR nebula is composed primarily of stellar material.

1.3 Dust in WR nebulae

Since the advent of infrared (IR) astronomy, thermal dust emission has been detected in the vicinity of hot stars and, specifically, in WR nebulae (van Buren & McCray, 1988). In particular, Marston (1991) analysed *IRAS* observations of the WR nebulae NGC 2359, NGC 6888, and RCW 58 around the WNE stars WR 7, and WR 136 and the WN8 star WR 40, respectively, and estimated the dust and their nebular masses in each case from the ratio of the 50 μm to 100 μm (60 μm to 100 μm for NGC 6888 case) intensities. The main conclusion of Marston (1991) is that the nebular masses in each

case are too large to be composed solely of material expelled from the central stars and so a sizable proportion of the nebular mass must be due to swept-up ISM material. However, Mathis et al. (1992) also analysed the *IRAS* data for RCW 58 and NGC 6888 with more sophisticated grain physics and grain spatial distribution and concluded that the nebular mass for RCW 58 is in fact two orders of magnitude lower than that estimated by Marston (1991) and is therefore consistent with all the nebular material having a stellar origin. More recently, Gvaramadze, Kniazev & Fabrika (2010) exploited mid-IR *Spitzer Space Telescope* data to identify compact nebulae around evolved stars. Follow-up spectroscopic identification resulted in an increase in the number of known Galactic LBVs and late-type WN stars. Toalá et al. (2015) analysed the mid-IR morphologies of nebulae around WR stars using *Wide-field Infrared Survey Explorer (WISE)* infrared images and proposed a classification scheme using the W4 22 μm band that is loosely correlated with the spectral type of the central star.

Recently, Rubio et al. (2020) showed a study of the infrared emission of NGC 6888 using used images and spectra from WISE, Spitzer, and Herschel that cover the 3–160 m wavelength range. They modelled the properties of the dust and ionized gas of the nebula with the ionization code CLOUDY. Rubio et al. (2020) propose that nebular dust consists of two populations of grain sizes, one with small-sized grains (0.002–0.008 μm) and another one with large-sized grains (0.05–0.5 mum) and estimated the dust and its nebular mass.

In the current literature, there are several studies about the formation of dust around the WC stars, which are known to be dust formers in a binary system (Usov, 1991). For example, using photometry data from Neowise-R, W1 and W2 bands (3.4 and 4.6 μm), the predecessor survey of the WISE mission, Williams (2019) looked for evidence of circumstellar dust emission in 128 galactic WC stars and 12 stars in the Large Magellanic Cloud (LMC) to identify dust makers. They identified 17 new Galactic WR stars dust makers and a second WR dust maker in the LMC.

1.3.1 Dust formation around massive stars

The condensation of grain species X in a region of pure gas is based on the creation of solid particles from atoms or molecules, called monomers[2]. Furthermore, to form dust grains some special conditions that enable nucleation and growth of the molecular monomers are indispensable. The dust formation region should be shielded from UV radiation because this limits the availability of neutral atomic and molecular monomers, and must have an adequate temperature to allow coagulation of the dust grains. The simplest assumption of dust formation is that the smallest grains are formed, once the temperature is sufficiently low, and the subsequent collisional growth of the grains.

O-stars are a source of UV radiation, so the circumstellar region around these stars

---

2   Individual unit of a species X.
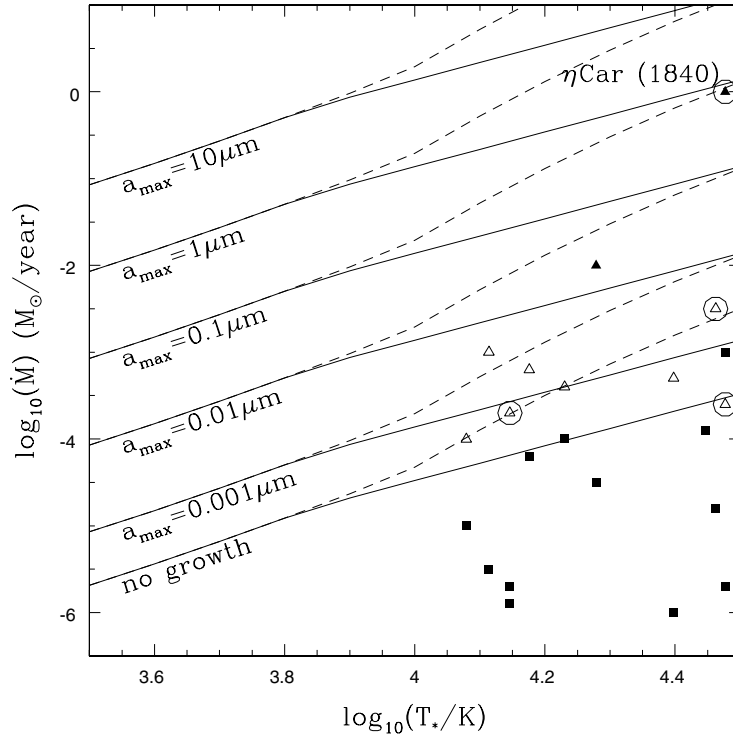
Figure 1.1: Maximum grain size (a_{max}) formed by eruptions from hot stars as a function of the mass-loss rate and stellar temperature, image taken from Kochanek (2011). The figure shows the trend of a_{max} assuming a photosphere temperature (photosphere created by stellar wind where the dust formation takes place) of T_{phot} =min($T_{\star}$,7000 K) and $T_{phot} = T_{\star}$, solid and dash lines, respectively. Scatter points (triangles, squares, etc.) represent galactic objects shown in Table 1 of Kochanek (2011), η Car is shown at the top right of the figure.

is inhospitable for the creation of dust. Nevertheless, after leaving the MS, in an evolutionary stage determined by its initial mass, the star might exhibit high mass-loss and become a source of dust grains, stardust. Even if a star finishes its life as a supernova (SN), it could produce a significant amount of grain material in the condensing ejecta.

Both RSG and LBV stars are known to be copious producers of dust but their production will cease as soon as the star enters the hot WR phase. In RSG stars, the stardust may be O-rich, such as silicates or Al_2O_3. Beyond the chromosphere, the temperature decline with the distance until falls below the condensation temperature of the dominant dust component, ~ 1000 K, at a few stellar radii (see Verhoelst et al., 2009). The outer boundary of the dust nucleation region is reached when the density and temperature of the circumstellar material become comparable with ISM values. Convection cells are thought to play an important role in levitating the molecular gas above the stellar photosphere into the upper atmosphere (Chiavassa et al., 2010). Detailed Very Large Telescope VISIR imaging studies of the nearest RSG, Betelgeuse (Kervella et al., 2011), show that the close circumstellar environment is very clumpy, suggesting inhomogeneous and episodic mass-loss. From optical polarimetric imaging observations of the extreme RSG VY CMa and its clumpy, dusty circumstellar environment, Scicluna et al. (2015) derive an average grain size of ~ 0.5 μm, that is, 50 times larger than grains in the diffuse ISM, with only small variation in grain size.

The condensation of dust in the environments of the much hotter and more luminous LBV stars requires some sort of shielding from the star's UV and optical emission (Gail et al., 2005; Kochanek, 2011). It has been proposed that dust formation in these objects is closely linked to the eruptive state of LBVs because only very high mass-loss rates $\dot{M} > 10^{-2.5}$ $M_\odot$ yr^{-1} can provide the dust-free wind optical depths required to shield the dust formation region. The maximum grain size a_{max} is related to the mass-loss rate in this scenario (Kochanek, 2011). Figure 1.1 shows the maximum size of grains that can form around a star with ejections of material, according to the temperature of the stellar photosphere and the rate of mass loss. Very large grains ($a_{max} > 1\mu$m) have been inferred for η Carinae (Morris et al., 2017).

As an additional fact, the production of dust by stellar material ejected by WR stars is possible if they are of the WC type, which has the lowest temperature among the WR types and belongs to a binary system. However, the high-density regions that allow dust production are produced by the collision of the wind from the WC star and its OB-type binary companion. That is, dust can be produced in the dense interaction region of colliding wind WC binaries. (e.g. Usov, 1991; Lau et al., 2020; Endo et al., 2022).

Studies of very young WR nebulae, or nebulae in low-density environments far from the Galactic plane that are not dominated by swept-up ISM material, should be able to shed some light on the history of the dust formation process in the previous evolutionary stage.

Figure 1.2: *Left panel*: Optical image of M 1-67 around WR 124 using Hα filter. *Middle panel*: Color-composite optical image of RCW 58 around WR 40 using Hα (red) and [O III] (blue) narrow filters. *Right Panel*: Optical image of Nebula around WR 16 using Hα filter.

1.4 WR nebulae sample

In this thesis, we are looking at the evolution of the gas and dust properties in WR nebulae around WNh stars. This will help us understand the formation and evolution process of dust around massive and luminous stars, as well as the evolution of the central star. The WNh stars are characterized by hydrogen emission lines in their spectrum. This suggests that WNh stars are an intermediate evolutionary phase between the main sequence and the RSG or LBV stages. The work in this thesis will contribute to this debate.

In particular, we focus on WN8h stars, these stars have been considered to be the first stage of the WNh phase. In our Galaxy there are 10 WN8h single stars[3], however, only three of them have a surrounding a well-defined nebula (see Figure 1.2). Two of them are stars from our sample: WR 124 and WR 40. The main physical parameters and the location of these WR stars are shown in Table 1.1.

1.4.1 M 1-67

We have selected the iconic WR nebula M 1-67 around the late-type WNh star WR 124 (also known as 209 BAC or Merrill's star) as an ideal object to study the dust properties of the circumstellar nebula. It has Galactic latitude $b = 3.31°$, which places it at $z \sim 370$ pc above the Galactic plane for an assumed distance of 6.4 kpc. At this position, the interstellar medium density is low enough that the nebula is expected to be composed almost entirely of material expelled from the progenitor of WR 124.

M 1-67 and its central star have been objects of many studies. WR 124 was identified as a high-velocity late-type WN star by Merrill (1938), who suggested an association with planetary nebulae based on the high velocity (see Perek & Kohoutek, 1967). Minkowski

---

3   Source: http://pacrowther.staff.shef.ac.uk/WRcat/

Table 1.1: Stellar parameters of the WN8h stars studied in this thesis, see Section 1.4.1 and 1.4.2 for details. Data obtained from Hamann et al. (2019).

WR	Nebula	α_{2000}	δ_{2000}	d (kpc)	z (pc)	$\log L$ ($L_\odot$)	M ($M_\odot$)	T_* (kK)	v_∞ (km s^{-1})	$\log \dot{M}$ ($M_\odot$ yr^{-1})
40	RCW 58	11:06:17.20	-65:30:35.24	3.83[a]	391[†]	5.9	28/26	44.7	650	-4.2
124	M 1-67	19:11:30.88	+16:51:38.20	6.4[b]	370[†]	5.8	22/20	44.7	710	-4.3

[a] From Rate & Crowther (2020).
[b] Estimated for this work (see Jiménez-Hernández, Arthur, & Toalá, 2020).
[†] Calculated based on distance in column 5.

(1946) discovered the clumpy Hα emission nebula on photographic plates and it was denominated M 1-67[4] and classified as a planetary nebula based on appearance. Later, Cohen & Barlow (1975) demonstrated, using primarily extinction arguments, that Merrill's Star and M 1-67 must be, respectively, a Population I WN8 star and its associated ring nebula.

Solf & Carsenty (1982) showed that the Hα, [N II], and [S II] velocity fields of the nebula obtained from long-slit spectra can be explained by a nearly spherical thin shell composed of numerous condensations expanding at 46 km s^{-1} with respect to a common centre. The centre of the expansion has a heliocentric velocity of 158 km s^{-1}, very similar to the radial velocity of the central star (175–200 km s^{-1}). This is consistent with the ejecta nebula scenario proposed by Chu (1981). A more complex dynamical structure, consisting of an expanding hollow spherical shell ($v = 46$ km s^{-1}) and a bipolar outflow ($v = 88$ km s^{-1}), was reported from a long-slit spectrographic study by Sirianni et al. (1998). Although M 1-67 appears symmetric and almost spherical (or hexagonal) in Hα images, with the star at the centre of the $\sim 100''$ diameter nebula (Grosdidier et al., 1998), high contrast coronographic studies (Nota et al., 1995) of the inner regions do reveal a bipolar structure, which is also evident in *Spitzer* 24-μm images (Gvaramadze, Kniazev & Fabrika, 2010). This has been attributed to anisotropic outbursts such as are seen in LBV (Nota, 1999). Recently, Zavala et al. (2022) present a morpho-kinematic analysis of M 1-67 based on modelling high-resolution San Pedro Mártir (SPM) Manchester Echelle Spectrograph (MES) using SHAPE (Steffen et al., 2011), a 3D reconstruction tool for astrophysical objects. They reveal to M 1-67 as a bipolar nebula with three concentric structures, each structure is composed by a torus in expansion with velocities between 30 km s^{-1}–60 km s^{-1}, and a hollow ellipsoidal structure that has maximum velocities of 90 km s^{-1}. Zavala et al. (2022) propose that similar kinematics of the toroidal structures indicates that it is just a structure created through the common envelope (CE) evolution. Furthermore, based on the rate of expansion of the internal structure, they estimate that the CE took place $11.8^{+4.6}_{-0.8}$ kyr ago.

Spectra of M 1-67 show strong [N II] and Hα nebular lines but [O III] is almost

---

4   Object 67 in Table 1 of Minkowski (1946).

completely absent (see e.g. Esteban et al., 1991). Abundance determinations find that N is enhanced, O is deficient, and S has normal H II region abundances. This is further evidence that WR 124 had a massive progenitor since these abundances are an indication of material processed in the CNO cycle (Esteban et al., 1991) and it reinforces the idea that there has been no significant interaction with the ISM. Moreover, the physical conditions in the nebula are found to be consistent with a very low ionization level and an electron temperature $T_e \sim 6200 - 8200$ K (Esteban et al., 1991; Fernández-Martín et al., 2013).

The distance to WR 124 and M 1-67 is not well determined and has been a subject of discussion. Extinction studies put a lower limit to the distance of 2.5 kpc (Esteban et al., 1991), while a spectrophotometric distance of 8.4 kpc was determined by Hamann et al. (2006). On the other hand, Marchenko, Moffat & Crowther (2010) used multi-epoch *Hubble Space Telescope (HST)* images to estimate a geometric distance of 3.35 ± 0.67 kpc to M 1-67. The recent *Gaia* Data Release 2 provides five-parameter astrometric data for WR 124 (positions, parallax, and proper motions), which can be combined to estimate the distance using Bayesian methods (Bailer-Jones et al., 2018; Luri et al., 2018). Recently, Rate & Crowther (2020) presented a method to estimate distances to WR stars using the *Gaia* data including the *G*-band photometry and estimated a distance of $5.9^{+1.48}_{-1.08}$ kpc for WR 124 using a prior based on H II regions and dust extinction. The H II region based prior is not adequate for this star, so we instead performed our own calculation using the *Gaia* data and adopting the Bailer-Jones et al. (2018) geometric prior with a parallax zero-point correction using data from Luri et al. (2018), and we obtained $6.4^{+2.45}_{-0.80}$ kpc. In Appendix A in Jiménez-Hernández, Arthur, & Toalá (2020), we describe the details of this procedure and show that both distances are consistent within the estimated error values. Following our result, in this thesis we adopt 6.4 kpc as the distance to WR 124 and its nebula. At this distance, the 110-arcsec diameter of the nebula corresponds to a spatial size of 3.4 pc.

Vamvatira-Nakou et al. (2016) presented *Herschel* imaging and spectroscopic observations of M 1-67. A comparison of the infrared images with optical images shows that the nebular dust coincides with the ionized gas, indicating that the dust and gas are mixed. Vamvatira-Nakou et al. (2016) used the 2-Dust code (Ueta & Meixner, 2003) to model the dust emission and concluded that two populations of dust grains were required to produce the infrared spectral energy distribution (SED). The total mass of dust resulting from their model is 0.22 $M_\odot$ of which 0.21 $M_\odot$ corresponds to the population of large grains with radii from 2 to 10 μm. They conclude that the progenitor of WR 124 was an RSG with initial mass ~32 $M_\odot$. However, such large grain sizes are not consistent with observations of nearby RSG (Scicluna et al., 2015) and such a low progenitor mass is not consistent with an LBV origin for the nebula, such has been proposed by several authors (see e.g. Sirianni et al., 1998; Fernández-Martín et al., 2013).

1.4.2 RCW 58

The nebula RCW 58 surrounds the WN8h star WR 40 (HD 96548). This WR nebula consists of a clumpy elliptical ring-like structure mostly detected in Hα (see Fig. 1.2 middle panel; Stock & Barlow, 2010) enclosed within faint, extended, smooth [O III] emission detected in narrow-band images. Gruendl et al. (2000) suggested that the offset between the Hα and [O III] emission peaks is a result of radiative cooling behind a shock wave propagating into the circumstellar medium, where the outer [O III] skin traces the position of the expanding shock. The kinematics of RCW 58 is poorly determined. Fabry-Perot spectra obtained by Chu (1982) found chaotic motions consisting of random velocity variations on the order of 30 km s^{-1} and line-broadening or line-splitting of 60 km s^{-1}. High-resolution long-slit spectra taken at the bright south-east edge by Smith et al. (1988) are consistent with a shell expanding at $v_{\mathrm{exp}} = 87$ km s^{-1} containing clumps moving with velocities lower than the shell expansion velocity. Both shell and clumps have linewidths in excess of thermal broadening, indicative of turbulence.

Optical spectroscopic studies of RCW 58 have addressed the chemical abundances and physical properties of this WR nebula (see e.g. Kwitter, 1984; Rosa & Mathis, 1990; Stock, Barlow & Wesson, 2011) and have confirmed strong nitrogen and helium enrichment. This is evidence that CNO-cycle nucleosynthesis products are present in stellar ejecta material. The nebula is low-ionization and low-density. An electron temperature $T_{\mathrm{e}} = 6450 \pm 200$ K and electron density $n_{\mathrm{e}} = 100 \pm 100$ cm^{-3} were derived from high-resolution spectra obtained recently by Esteban et al. (2016) using the Magellan Echelle at the 6.5 m Clay Telescope. The total mass of ionized gas in RCW 58 has been estimated to be of the order of 3 M$_{\odot}$ from 11 cm radio flux measurements (Smith & Batchelor, 1970).

There are not many IR studies addressing the dust properties of RCW 58. Its morphology is very similar to that of the optical image and the dust appears to be correlated with the Hα clumps (see Fig. 2.1). Marston (1991) analysed *IRAS* observations at 50 and 100 μm of RCW 58 along with other two WR nebulae (S 308 and NGC 6888). The main conclusions were that the dust in RCW 58 has temperatures ~ 33 K with a large variation (25–50 K) and that the estimated mass of dust is 0.39 M$_{\odot}$, implying a total nebular gas mass ~ 39 M$_{\odot}$ far too big to have a stellar ejecta origin. As a result, Marston (1991) suggested that RCW 58 was composed mainly of swept up ISM. Mathis et al. (1992) used the same *IRAS* observations but analysed the 25, 60, and 100 μm emission, and found that the IR properties of RCW 58 can be explained by the presence of two populations of grains with size distributions 0.002–0.008 μm and 0.005–0.05 μm for the stellar radiation field and distance they assumed. The estimated mass of dust in their models is $< 10^{-2}$ M$_{\odot}$, with a corresponding total nebular mass of ~ 0.4 M$_{\odot}$. More recently, Toalá et al. (2015) used *Wide-field Infrared Survey Explorer* (*WISE*) observations and showed that RCW 58 is heavily contaminated by background ISM material mainly

detected in the 12 μm band, which was not taken into account by these two previous IR studies.

The optical variability of WR 40, the central star of RCW 58, has been interpreted previously as originating from a WR+compact binary system (Moffat & Isserstedt, 1980). However, Ramiaramanantsoa et al. (2019) presented recent *BRIght Target Explorer* (*BRITE*) constellation of nanosatellites observations of WR 40 and suggest that the variability from this WN8 star is merely due to intrinsic stochastic variations in the wind. Ramiaramanantsoa et al. (2019) showed that starlight scattered by free electrons in a distribution of discrete clumps of different masses and lifetimes in WR 40's wind can account for the variability in the light curve. If WR 40 has a companion, as suggested for WN8 stars, it is well hidden within its dense wind as suggested for WR 124 (see e.g. Toalá et al., 2018).

1.4.3 Objectives of the present thesis

Our specific objective in this thesis is to perform a detailed characterization of the dust in M 1-67 and RCW 58 by analysing *WISE*, *Spitzer*, and *Herschel* observations and using the spectral synthesis code CLOUDY (Ferland et al., 2017) to fit simultaneously the dust photometric data and nebular optical data from the literature. Dust parameters can give us information about mass-loss history of their central star and the origin of these WR nebulae.

From the literature, many authors have studied M 1-67 and RCW 58 in the single star scenario. We were looking for clues in their physical conditions estimated from observations about their formation history.

1.5 Publications

The results presented in this thesis have been published in:

- *Dust in the Wolf-Rayet nebula M 1-67*
  Jiménez-Hernández P., Arthur S. J. & Toalá J. A.; 2020, MNRAS, 497, 4128

- *Dust in RCW 58: Clues to common envelope channel formation?*
  Jiménez-Hernández P., Arthur S. J., Toalá J. A. & Marston, A. P., 2021, MNRAS, 507, 3030

Other publications related to this thesis:

- *Unveiling the stellar origin of the Wolf-Rayet nebula NGC 6888 through infrared observations*
  Rubio, G.; Toalá, J. A., **Jiménez-Hernández, P.**, Ramos-Larios, G., Guerrero, M.

A., Gómez-González, V. M. A. , Santamaría, E. & Quino-Mendoza, J. A., 2020, MNRAS, 499, 415

- *Carbon dust in the evolved born-again planetary nebulae A 30 and A 78*
  Toalá, J. A., **Jiménez-Hernández, P.**, Rodríguez-González, J. B., Estrada-Dorado, S., Guerrero, M. A., Gómez-González, V. M. A., Ramos-Larios, G., García-Hernández, D. A. & Todt, H., 2021, MNRAS, 503, 1543

2 Observations

In order to trace the origins of WR nebulae, we need to model their nebular and dust properties. For this, we studied Infrared (IR) photometric observations from M 1-67 and RCW 58. In this chapter, we present the IR observations and their treatment to obtain Spectral Energy Distributions (SED) from the two nebulae. In addition, we develop a rough analysis of both IR SEDs in the far infrared based on modified blackbody emission. In the last section of this chapter, we present a study of the distribution of the ionized gas of RCW 58 using a radio continuum observation from ATCA.

2.1 Infrared telescopes

Infrared radiation is subdivided into near infrared (near-IR), mid infrared (mid-IR) and far infrared (FIR) encompassing a wide wavelength range ($\sim 1\ \mu$m – 1000 μm). Since IR traces cold gas and dust, IR observations have been useful to study nebulae around Wolf-Rayet (WR) stars. Some bands trace specific material, for example, the *K* band (2.2 μm) of the near-IR and the 12 μm band of the mid-IR mainly trace interstellar matter (Wachter et al., 2010). In this thesis, we are interested in the circum- and inter-stellar dust emission that is easily visible at mid-IR and FIR.

The terrestrial atmosphere can absorb radiation from space. However, there are bands of the electromagnetic spectrum that can pass through it, these bands are called 'windows'. For optical light and radio bands, Earth's atmosphere is almost completely transparent. However, oxygen and water vapour absorb a significant amount of IR radiation, while the other (UV and X-ray) parts of the electromagnetic spectrum are almost fully absorbed. Because of the above, infrared telescopes should be placed at high altitudes, such as high mountains or in space. During the 1960s, balloons and aircraft with attached IR telescopes were put into operation. A modern example of these type of telescopes is SOFIA (Stratospheric Observatory for Infrared Astronomy; Young et al., 2012; Temi et al., 2014) which was launched in 2010 by NASA.

IR telescopes have many challenges, among those, they must be equipped with cryogen tanks in order to avoid contamination by the IR emission from the instruments. For that reason, these telescopes have limited lifetimes. At the same time, IR space telescopes should be positioned to avoid direct observation of the Sun due to their high sensitivity. Some examples of this kind of telescopes are: *IRAS* (Infrared Astronomical Satellite; Neugebauer et al., 1984), *ISO* (Infrared Space Observatory Kessler et al., 1996),

Table 2.1: Characteristics of each band used in this thesis.

λ_c ($\Delta\lambda$) [μm]	Band	FWHM [μm]	PSF ["]	Sensitivity [mJy]
WISE				
12	W3	6.276	6.5	0.8
22	W4	4.7397	12.0	8
Spitzer				
24	MIPS	5.3245	6	0.11
Herschel				
70	PACS	22.0966	5.46 × 5.76	4.7
100	PACS	35.6865	6.69 × 6.89	5.5
160	PACS	74.9540	10.65 × 12.13	10.5
250	SPIRE	65.8930	17.9	9.0
350	SPIRE	93.7199	24.2	7.5
500	SPIRE	184.8041	35.4	10.8

Spitzer (Werner et al., 2004), *Herschel* (Pilbratt et al., 2010) and *WISE* (Wide-field Infrared Survey Explorer; Wright et al., 2010).

In this thesis we used public IR observations from a variety of IR satellites: *Spitzer*, *Herschel* and *WISE*. The Space Telescope *Spitzer*, launched in 2003 by NASA, was deactivated in 2020 and consisted of an 85 cm telescope and 3 infrared instruments: IRAC (Infrared Array Camera), IRS (Infrared Spectrograph), and MIPS (Multiband Imaging Photometer). These three instruments provide imaging and spectroscopy data in a range of 3 μm–180 μm. *Spitzer* used an Earth-trailing heliocentric orbit with a semi-major axis very slightly larger than that of the Earth's orbit.

The *Herschel* Space Observatory had a successful launch in 2009 towards its operational orbit around the Earth-Sun L2 point, this happened as part of the fourth mission of ESA (also with the participation of NASA). *Herschel* carries a 3.5 m diameter telescope, with two cameras of medium resolution (PACS and SPIRE), and a very high resolution heterodyne spectrometer (HIFI). *Herschel* equipment allow us observe in a spectral range from far-infrared to submillimetre (55 μm–671 μm).

WISE was launched at the end of 2009 by NASA, through the MIDEX (Medium Class Explorer) mission operated by the Jet Propulsion Laboratory (JPL). *WISE*'s orbit was Sun-synchronous at 525 km from Earth, with an inclination chosen to give a precession rate of 360° in one year (97.5°). *WISE*'s filters cover a spectral range from 3 μm to 22 μm.

2.2 Observational data

2.2.1 IR photometric data

We obtained IR images of M 1-67 and RCW 58 from *WISE* and *Herschel* (PACS and SPIRE). Additionally, we used a image from *Spitzer* (MIPS) for the M 1-67 case. The combination of all these observations gives us a broad view of the nebulae covering the 12–500 μm wavelength range and enables us to construct a detailed SED. Table 2.1 presents main characteristics of each filter used. Details of the individual observations are provided in Table 2.2. All observations were retrieved from the NASA/IPAC - IRSA (Infrared Science Archive)[5]. Photometric data required to pass through a pipeline to be used for research, in general, IR data product from *WISE*, *Herschel* and *Spitzer* can be classified as level 0 (raw data), level 1-2 (reduced data), and level 3 (combination and/or manipulation of previous level data), accordingly their processing level. In this thesis, we used images with Levels 2 and 3 (see Table 2.2). It should be noted that the IR images were used as they were downloaded from the public archive, without performing any additional procedures for processing the observations.

M 1-67

Figure 2.1 shows all of the IR images obtained from *WISE*, *Spitzer* (MIPS), and *Herschel* (PACS and SPIRE). These IR images clearly show a bipolar morphology (Sirianni et al., 1998), in contrast to the symmetrical nebula seen in deep *HST* WFPC2 Hα image of M 1-67 (Grosdidier et al., 1998). This is appreciated to some extent even in the long wavelength *Herschel* SPIRE images (bottom row of Figure 2.1). Some extended emission can be seen in the WISE 12 μm and *Herschel* SPIRE images, which is very likely to be contribution from material in the line of sight rather than material at the location of M 1-67, given its position above the Galactic plane (see Section 1.4.1).

RCW 58

Fig. 2.2 shows all IR images of RCW 58, together with and Hα image retrieved from the SuperCOSMOS Sky Survey[6] (Parker et al., 2005). RCW 58 is clearly detected in most images except in the *Herschel* SPIRE images, which are dominated by background cold interstellar material. We note that the *Herschel* PACS images do not entirely cover RCW 58. The observations cover the NW, NE, SE and SW regions of the nebula (see Figure 2.2).

---

5 https://irsa.ipac.caltech.edu/frontpage/
6 http://www-wfau.roe.ac.uk/sss/halpha/

Table 2.2: Details of the IR observations used in this thesis.

Instrument	Date [yyyy-mm-dd]	Obs. ID	PI	λ_c or $\Delta\lambda$ [μm]	Duration [s]	Processing level
M 1-67						
WISE	2010-04-11	2876p166_ac51		12 (W3), 22 (W4)	8.8	Level 3
Spitzer MIPS	2006-10-15	30544	Morris, P.	24	3	Level 2
Herschel PACS	2010-04-08	1342194080	Groenewegen, M.A.T.	70, 160	2622	Level 3
		1342194082	Groenewegen, M.A.T.	100, 160	2622	Level 3
Herschel SPIRE	2010-09-21	1342204949	Groenewegen, M.A.T.	250, 350, 500	911	Level 2
Spitzer IRS	2004-04-19	199	Houck, J.R.	7.53−14.73 (SL1)	121.9	Level 2
				14.27−21.05 (LL2)	94.4	
				20.56−38.42 (LL1)	94.4	
RCW 58						
WISE	2010-01-22	1677m652_ac51		12 (W3), 22 (W4)	8.8	Level 3
Herschel PACS	2012-03-22	1342243127	A.P. Marston	70, 160	1096	Level 3
		1342243129	A.P. Marston	100, 160	1096	Level 3
Herschel SPIRE	2012-03-03	1342241089	A.P. Marston	250, 350, 500	1086	Level 2

2.2.2 Extra observational data

In the case of M 1-67, we obtained *Spitzer* Infrared Spectrograph (IRS) low-resolution spectroscopic data, which covers a spectral range of 7−38 μm (see details in Table 2.2). These observations were processed using the CUbe Builder for IRS Spectral Maps (cubism; Smith et al., 2007). The location of the slit is shown schematically in Figure 4.1.

Additionally, we complemented our IR images of RCW 58 with radio observations obtained with the Australian Telescope Compact Array (ATCA) to extend the wavelength range of our study. The ATCA observations have a total exposure time of 44.53 h in the 750 A configuration and were taken on 2010 June 30 under project C2618 (PI: J. A Toalá). We created a 10 cm continuum image with a central frequency ν_0 = 2.735 GHz (10.9 cm), an rms noise from 0.2 to 0.89 mJy beam^{-1}, and a synthesized beam with FWHM = 21.3 × 17.1 arcsec.

2.3 Photometry

In order to extract a SED from M 1-67 and RCW 58 we used the photometric observations mentioned in previous section. For each case we defined a region that encompasses the nebular emission for each individual IR image. We then integrated the flux density for each individual IR image. The background correction was applied to the flux value from each image. The background is not uniform and varies from band to band. Thus, the selected background regions for each IR image are not the same as those for a different image. Backgrounds regions were selected by eye and a set of n-background[7]

---

7   n does not have the same value for each photometric image.
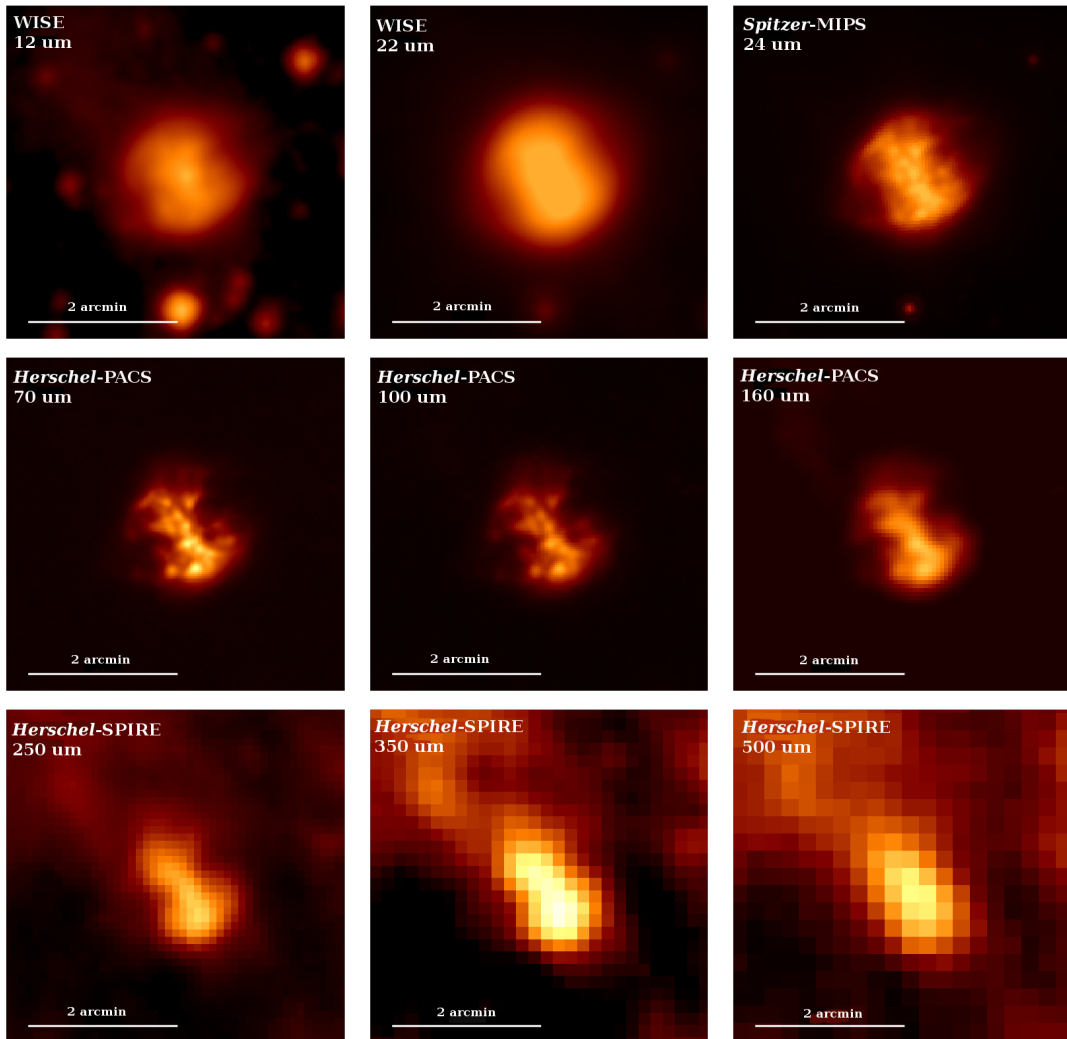
Figure 2.1: Images of the nebula M 1-67 obtained by *WISE*, *Spitzer* and *Herschel*. The different bands are centered at 12, 22, 24, 70, 100, 160, 250, 350 and 500 μm. North is up and east to the left. Figure taken from Jiménez-Hernández, Arthur, & Toalá (2020).
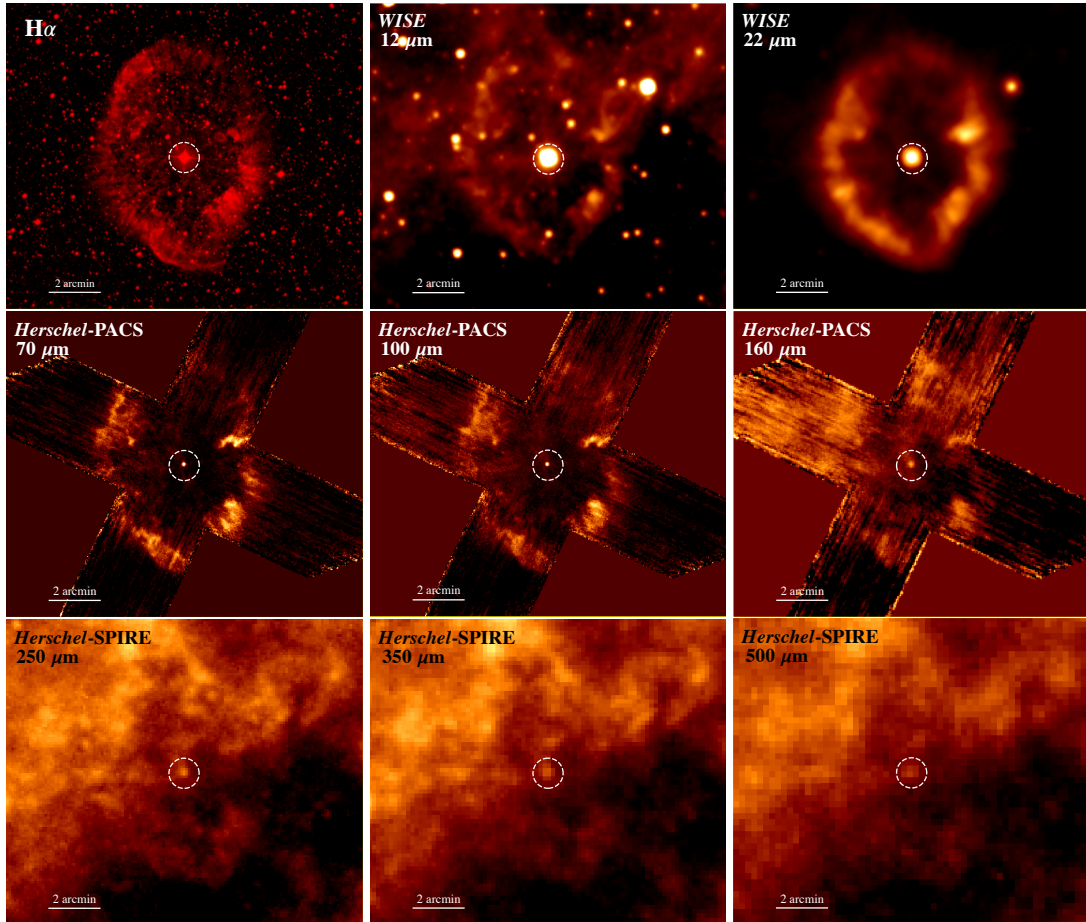
Figure 2.2: Optical (Hα - top left panel) and IR images of the WR nebula RCW 58. The IR images were obtained by *WISE* and *Herschel* PACS and SPIRE. All panel have the same field of view. North is up and east to the left. Figure taken from Jiménez-Hernández et al. (2021).

regions were obtained for each image. We subtracted each background from the nebular flux density in order to obtain *n* background-subtracted fluxes for each IR wavelength image. The mean and standard deviation of these values then give us the final flux value and measurement uncertainty (σ_{Back}), respectively. Fig 2.3 shows an example of the background selection process in M 1-67.

To calculate the total error from each IR band, we combine the different contributions, as well as the uncertainty due to the background subtraction. The calibration uncertainty (σ_{Cal}) from each instrument has to be taken into account, too. Then, the total error is given by

$$\sigma_{\text{Tot}} = \sqrt{\sigma_{\text{Back}}^2 + \sigma_{\text{Cal}}^2}. \tag{2.1}$$

For the *WISE* data, the calibration uncertainty is 4.5 per cent and 5.7% from the W3 and W4 bands[8], respectively. The *Herschel* data calibration uncertainty is 5% for the PACS and 7% for the SPIRE instruments[9], while that for the *Spitzer* MIPS is 4%[10].

Every defined region in IR images was made with the software ds9 and calculations were done using standard PYTHON routines. In particular case of radio observation we employ CASA (McMullin et al., 2007) to extract fluxes from regions of interest.

2.3.1 Bipolar nebula M 1-67

We note that the photometry of the nebula extracted from the *WISE* W3 band has a significant contribution from the central star, WR 124. We carefully subtracted the contribution from WR 124 by comparing the PSF of stars in the field. This produced a clean photometric measure of the W3 12-μm band.

In Table 2.3, we present the final flux estimates for each IR image of M 1-67 with their corresponding uncertainties (σ_{Tot}) associated with the instrument calibration and the background subtraction process. The final IR SED of M 1-67 is presented in Figure 2.4, from this figure, it can be seen that M1-67 has a broad IR SED with a peak around 70 μm.

2.3.2 Ring nebula RCW 58

We attempted to obtain a global spectra energy distribution of RCW 58 by selecting an elliptical region encompassing the nebular emission delimited in the Hα image (see Fig. 2.2 upper left-hand panel). However, at IR wavelengths there is a strong gradient of emission from the north to the south of the image panels in Fig. 2.2, which we attribute to background ISM since it does not appear to attenuate the optical image. Furthermore, the incomplete coverage of the *Herschel* PACS observations severely restricted our

---

8 Explanatory Supplement to the WISE Preliminary Data Release Products.
9 PACS and SPIRE handbook.
10 MIPS Instrument Handbook.
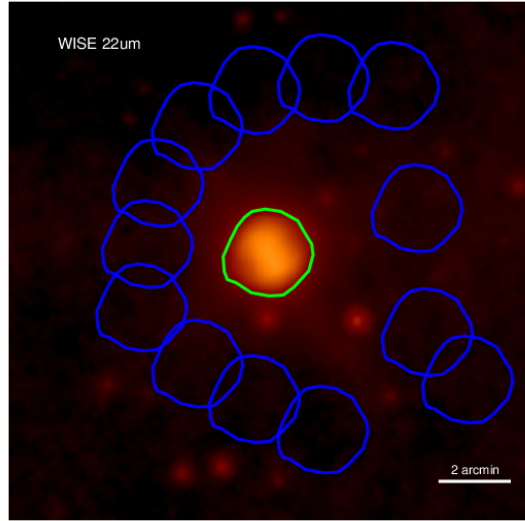
Figure 2.3: Examples of background selection regions around M 1-67. The image shows the *WISE* band 4. The region used for extracting the flux from M 1-67 is shown with a green contour and the background regions are shown in blue. Figure taken from Jiménez-Hernández, Arthur, & Toalá (2020).

Table 2.3: Flux densities and uncertainties of different IR band observations of M 1-67. σ_{Back} is the uncertainty associated with background inhomogeneity, σ_{Cal} is the uncertainty associated with the instrument calibration of each observation and σ_{Tot} is the sum of these uncertainties.

Instrument	λ_{c} [μm]	Flux [Jy]	σ_{Back} [Jy]	σ_{Bal} [Jy]	σ_{Tot} [Jy]
WISE	12	1.36	0.05	0.06	0.08
	22	17.91	0.04	1.02	1.80
Spitzer MIPS	24	17.47	0.08	0.70	0.7
Herschel PACS	70	53.72	0.25	2.69	2.70
	100	39.34	1.62	1.97	2.55
	160	16.55	1.79	0.83	1.98
Herschel SPIRE	250	4.85	1.06	0.34	1.11
	350	1.70	0.53	0.12	0.53
	500	0.49	0.21	0.03	0.21
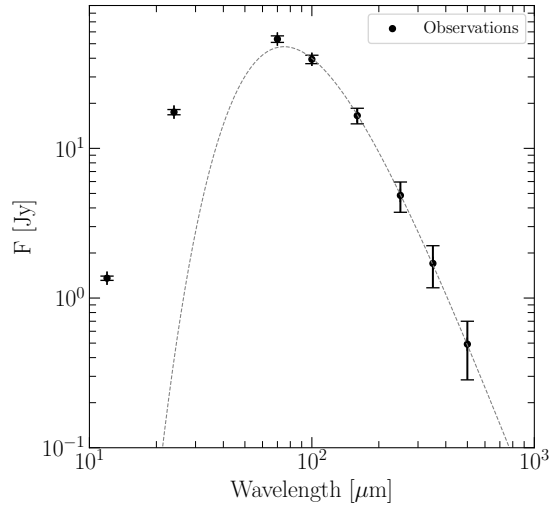
Figure 2.4: SED obtained from the IR observations of M 1-67: (black) dots (see Table 2.3). The error bars take into account uncertainties associated with the instrument calibration and the background subtraction process. The dashed line shows the best fit (for $\lambda \geq 100\mu$m) to the *Herschel* PACS and SPIRE photometry for a modified black body model, see Section 2.3.3 for details.
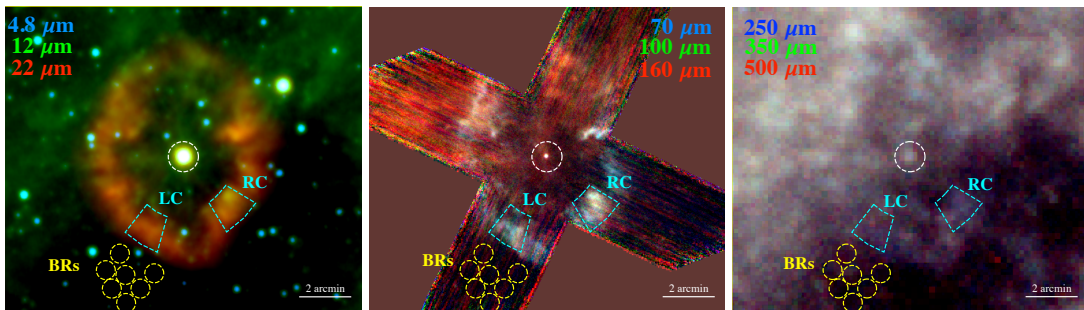
Figure 2.5: Color-composite IR images of RCW 58. The left, middle and right panels correspond to *WISE*,*Herschel* PACS and SPIRE observations, respectively. The selected regions for study in RCW 58 are indicated with cyan polygonal shapes (RC and LC). Background regions are represented by (yellow) dashed-line circular apertures. The position of the central star, WR 40, is indicated in the centre of each panel by a (white) circular region. All images have same the Field of View (FoV). North is up and East is to the left. Figure taken from Jiménez-Hernández et al. (2021).

Table 2.4: Flux densities and uncertainties of different IR band observations of the selected RC and LC regions in RCW 58. σ_{Back} is the uncertainty associated with background inhomogeneity, σ_{Cal} is the uncertainty associated with the instrument calibration of each observation and σ_{Tot} is the sum of these uncertainties.

| Instrument | λ_c | RC region | | | | LC region | | | |
| | | Flux | σ_{Back} | σ_{Cal} | σ_{Tot} | Flux | σ_{Back} | σ_{Cal} | σ_{Tot} |
	[μm]	[Jy]	[Jy]	[Jy]	[Jy]	[Jy]	[Jy]	[Jy]	[Jy]
WISE	12	0.0936	0.0054	0.0042	0.0068	0.0694	0.0046	0.0031	0.0055
	22	0.4471	0.0130	0.0255	0.0286	0.4234	0.0111	0.0241	0.0266
Herschel PACS	70	3.4458	0.1508	0.1723	0.2290	2.5268	0.1292	0.1263	0.1807
	100	3.8710	0.2496	0.1936	0.3158	2.8545	0.2137	0.1427	0.2570
	160	1.9205	0.1507	0.0960	0.1787	1.1943	0.1289	0.0597	0.1420
Herschel SPIRE	250	0.6344	0.1167	0.0444	0.1249	0.5012	0.1006	0.0351	0.1122
	350	0.2351	0.0531	0.0165	0.0556	0.2098	0.0468	0.0147	0.0512
	500	0.0897	0.0319	0.0063	0.0325	0.0968	0.0274	0.0068	0.0291
	[μm]	[mJy]	[mJy]	[mJy]	[mJy]	[mJy]	[mJy]	[mJy]	[mJy]
ATCA	1.09×10^5	10.8	0.295	-	0.295	4.18	0.106	-	0.106

choices for background regions to use in the extraction process. As a result, it proved impossible to produce a satisfactory global SED. This precluded an appropriated analysis of the global properties of RCW 58. Consequently, we decided to restrict our analysis to two specific clumps in the southern part of RCW 58, situated in regions relatively free from background contamination.

We selected two bright clumps located in the nebular ring towards the south-west (SW) and south-east (SE) from the central star WR 40. These clumps are labelled RC and LC and are illustrated in Fig 2.5. This figure also shows the regions used for the background extraction (labelled BRs). These are located external to the nebula towards the SE direction. We note that the background around WR 40 is no homogeneous and to alleviate this issue we created seven independent regions which were used to generate an average background. This situation is similar when extracting fluxes from the ATCA image. The corresponding background regions for the ATCA photometry are shown in Fig. 2.6 with gray dashed-line circular apertures.

In Table 2.4, we present the flux estimates for each IR and radio measurement of RC and LC with their corresponding uncertainties (σ_{Tot}). The final SED of RC and LC regions are presented in Fig 2.7. The SEDs for both clumps are very similar, being broad with peak between 70 and 100 μm.
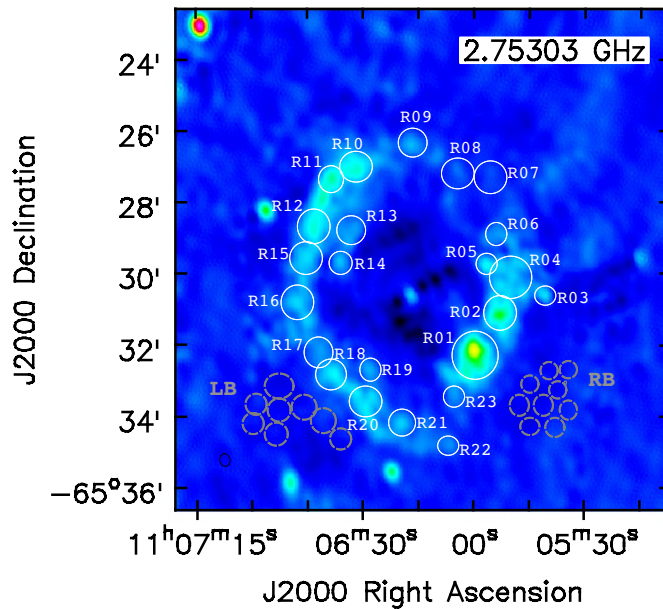
Figure 2.6: ATCA image of 2.75 GHz continuum in Jy/beam units of RCW 58. The synthesized beam FWHM is 21.3 × 17.1 arcsec and the rms noise between 0.2 to 0.89 mJy beam^{-1}. White Regions were used to get a density estimation. RB and LB gray regions were used to estimate the background correction in the RC and LC photometry process, respectively. Figure taken from Jiménez-Hernández et al. (2021).
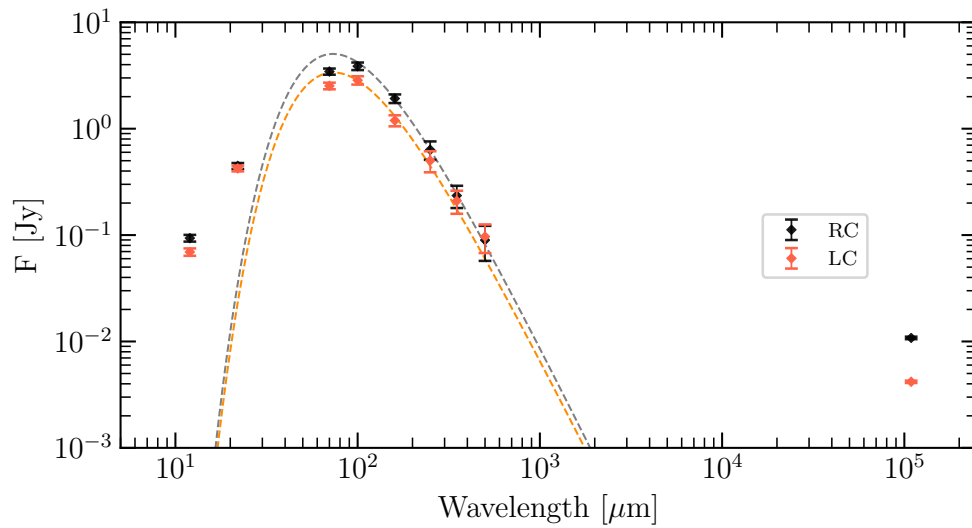
Figure 2.7: SED obtained from the IR and ATCA observations of RCW 58: black and red diamonds correspond to the RC and LC regions, respectively. The error bars were obtained from the instrument calibration and background subtraction process. The gray and orange dashed lines show the best fit (for $\lambda \geq 100$ μm) to the *Herschel* PACS and SPIRE photometry for a modified black body model of the RC and LC regions, respectively (see Section 2.3.3 for details).

2.3.3 Modified blackbody model

Dust grains radiate according to Kirchhoff's law if the underlying assumption is that the dust is optically thin and is in local thermodynamic equilibrium (LTE), that is, the emission coefficient (ϵ_ν, for unit mass or unit volume) is (Kruegel, 2003)

$$\epsilon_\nu = \kappa_\nu B_\nu(T_{\mathrm{D}}), \tag{2.2}$$

where κ_ν is the mass absorption coefficient and $B_\nu(T_{\mathrm{D}})$ is the Planck function. The terms ϵ_ν and $\kappa_\nu B_\nu(T_{\mathrm{D}})$ are referred as emissivity and the modified Planck function (or modified blackbody). On the other hand, in FIR ($\lambda \geq 100\ \mu$m) absorption coefficient has a power-law dependence of frequency, $\kappa_\nu \propto \nu^\beta$ (Kruegel, 2003). From observations we know that β ranges between 0–2, this factor, called emissivity index, depends on the dust properties; for example, $\beta \sim 2$ is representative of crystalline-type grains, while we expect $\beta \sim 1$ for amorphous grains (Tielens & Allamandola, 1987). For a specific case, $\beta = 1.2$ is consistent with amorphous-type carbon dust (Zubko, Krełowski, & Wegner, 1996).

A modified blackbody (MBB) fit to the dust emission in the FIR is a useful tool for estimating the dust mass and mean dust temperature of the coolest, i.e. the largest dust grains in M 1-67 and RCW 58. It is important to note that under this scenario we assume that a single temperature T_{D} and emissivity index β are representative of all the dust grains. The MBB fit to the observed flux densities is (Kruegel, 2003)

$$F_\nu = M_{\mathrm{D}} \kappa_\nu \frac{B_\nu(T_{\mathrm{D}})}{d^2}, \tag{2.3}$$

where d is the distance to the nebula, $B_\nu(T_{\mathrm{D}})$ is the Planck function, and M_{D} is the total dust mass. The dust mass absorption coefficient κ_ν is a function of frequency parameterized by the emissivity index β, that is

$$\kappa_\nu = \kappa_{\nu 0} \left(\frac{\nu}{\nu_0} \right)^\beta. \tag{2.4}$$

The dust opacity normalization for $R_{\mathrm{V}} = 3.1$ Milky Way dust is $\kappa_{\nu 0} = 1.92\ \mathrm{cm^2 g^{-1}}$ at the reference frequency $\nu_0 = 856.5$ GHz ($\lambda_0 = 350\ \mu$m) (Draine, 2003). Overestimates for the dust mass from IR SED fits can be avoided by using a more appropriate value for the dust opacity (Fanciullo et al., 2020). We choose a $\kappa_{\nu 0}$ value for a Galactic environment, Milky Way dust is a mix of carbonaceous and silicate grains in an approximate proportion of 30 to 70%, respectively (Weingartner & Draine, 2001). Additionally, it is thought dust in nebulae around massive stars is mainly compose by silicates (see Section 3.3 for more detail), for that reason, we considered $\kappa_{\nu 0}$ estimated from Milky Way data as a value

acceptable for this analysis. We selected a κ value at $\nu_0 = 856.5$ GHz as a normalization factor because falls to the middle of the range of our photometric data with $\lambda \geq 100$ μm.

The MBB fit returns the dust temperature T_D and the emissivity index β of the grains responsible for the emission at wavelengths $\lambda \geq 100$ μm. If d is known, then M_D provides the normalization of the model.

The fitting procedure minimizes a χ^2 function, which fits the model described in equation 2.3 to the observed SED (see e.g. Fig. 2.4 and Table 2.3). 3000 random flux samples were drawn from a normal distribution centred on the measured values with standard deviation equal to the uncertainty in each photometry measurement. We use only the *Herschel* PACS and SPIRE photometry for the fit, since these measurements have the least contamination from emission lines and cover the $\lambda \geq 100$ μm range.

For the M 1-67 case, the total dust mass resulting from this procedure is $M_D = 0.36 \pm 0.09$ $M_\odot$ and the characteristic dust temperature is $T_D = 37.52 \pm 6.51$ K. The emissivity index returned by the fit is $\beta = 2.02 \pm 0.38$. The obtained β value is sufficiently close to the spectral index of the underlying theoretical dust model (e.g. Andriesse, 1974), $\beta = 2$, suggesting that the emission for $\lambda \geq 100$ μm comes from dust in a very narrow temperature range, i.e. very likely a dust population with a small range of grain sizes. This MBB fit is shown in Figure 2.4 in comparison with the observed SED. This figure shows that the complete SED is too broad to be fit by a single population of grains.

For RC in RCW 58 we obtained $M_D = 0.041 \pm 0.007$ $M_\odot$, $T_D = 44.18 \pm 2.22$ K, and $\beta = 1.5 \pm 0.1$, while for LC we found $M_D = 0.029 \pm 0.006$ $M_\odot$, $T_D = 44.41 \pm 2.10$ K, and $\beta = 1.43 \pm 0.10$. The similarity in the mean temperature and emissivity index of the two clumps suggests that they share general dust properties. As in the M 1-67 case, we note that the SED peak of each clump is too broad to be fit by a single population of grains at a uniform temperature. We conclude that a detailed modelling will therefore be required to give the full picture of the grain populations and their spatial distributions, as has been suggested from previous IR studies of WR nebulae (e.g. Mathis et al., 1992).

It is important to note that the MBB fit gives us no information on the properties of small grains, which absorb most of the stellar radiation and are responsible for the majority of the mid-infrared emission from the nebula. Nevertheless, the value of the T_D estimated in this section will be a useful guide to restrict the large grain temperature in our detailed, self-consistent photoionization model of our nebulae sample.

2.4 Free-free emission of RCW 58

Radio continuum observations have been used in the past to study the distribution of the ionized gas, the electron density, and the ionized gas mass in a sample of WR ring nebulae (Cappa et al., 1999; Cappa, 2006). Our high angular resolution ATCA

observation, presented in Fig. 2.6, displays the elliptical clumpy morphology of RCW 58 and resembles the optical image shown in Fig. 2.2.

The ATCA observation provides an additional photometric measurement, which extends our IR SED to longer wavelengths. We used extraction regions similar to RC and LC described previously (see Fig. 2.5). The 2.75 GHz flux measurements of the RC and LC regions are listed in Table 2.4 and are also plotted alongside the IR photometry in Fig. 2.7, where the corresponding wavelength is $\lambda = 1.09 \times 10^5 \ \mu$m.

The high number of ionized photons estimate of WR 40 ($\log_{10}Q_H \sim 49 \ s^{-1}$) and the low density estimations let us assume that the radio emission in RCW 58 is due to free-free radiation and is optically thin. We calculated n_e for 23 different clumps identified in the main elliptical shell of RCW 58 (see Fig. 2.6). First, we calculated the brightness temperature, T_B, for each clump. T_B is defined as (Wilson, Rohlfs & Hüttemeister, 2009)

$$T_B = \left(\frac{c^2}{2k_B v_0^2} \right) \left(\frac{S}{\Omega} \right) , \tag{2.5}$$

where c is the speed of light, k_B is the Boltzmann constant, S is the measured flux at frequency v_0 and Ω is the angular size of each clump. Next, the emission measure, EM, can be expressed as

$$\text{EM} = 12.143 \ \tau \left(\frac{v_0}{[\text{GHz}]} \right)^{2.1} \left(\frac{T_e}{[\text{K}]} \right)^{1.35} , \tag{2.6}$$

where $\tau = T_B/T_e$ and T_e is the electron temperature. Finally, the electron density, n_e, can be expressed as

$$n_e = \sqrt{\text{EM}/D} , \tag{2.7}$$

where D is the depth of the nebular material in pc along the line of sight. We assumed that a electron temperature of 6000 K[11] and the line-of-sight depth of each clump is the same as its diameter, D.

Given the small uncertainties in flux measured from the ATCA observation, around 3% of the flux, Equation 2.7 calculates an uncertainty of 1.5% for the values of n_e[12]. The resultant n_e values obtained for each clump represent the average electron densities and are illustrated in the lower panel of Fig. 2.8 as a function of position angle and distance from the central star. We also estimated the peak n_e for each circular region by adopting the major axis of the beam as the diameter (and depth) of each clump. The peak n_e values are shown in the upper panel of Fig. 2.8.

From Fig. 2.8 we see that the range of values for both the average and peak electron densities is between 10 and 60 cm^{-3}. The highest values are found for position angles $\theta = 45°\pm15°$ (regions R10, R11, and R12) and $\theta = 245°\pm15°$ (regions R01 and R02), which are almost exactly diametrically opposite. Clump R01 is contained within the RC region

---

11 From estimation of T_e[N II]5755/6584 from Esteban et al. (2016)
12 Estimate from the uncertainty propagation: $\sigma n_e = \frac{n_e}{2} \frac{\sigma S}{S}$
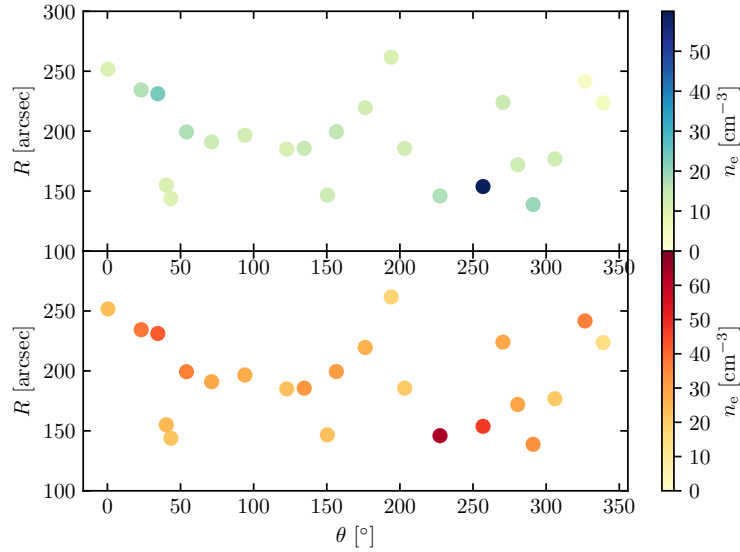
Figure 2.8: Electron density distribution of RCW 58 as a function position angle and distance with respect to the central star (θ, R). Upper panel shows the peak densities, and bottom panel shows average densities. Each point corresponds to a single region of Figure 2.6. Figure taken from Jiménez-Hernández et al. (2021).

described in Section 2.3. For comparison, taking into account the 5% uncertainty in our density estimates, we find that these values are consistent with the estimated value of 100 ± 100 cm^{-3}, which was found by measurements of the [OII] 3726, 3729 Å doublet (see Esteban et al., 2016).

3   Photoionization models

Our aim is to produce a model of each nebula in our sample that can simultaneously reproduce the nebular optical properties and its IR photometry and spectroscopy. The nebular material consists of gas and dust, both of which interact with the UV flux from the central star and they cannot be treated separately. The spectral synthesis and plasma simulation code CLOUDY (Ferland et al., 2017) is one of the best tools to investigate this interaction, coupled with the PYCLOUDY library (Morisset, 2006) to obtain the fluxes and line intensities through apertures corresponding to the different instruments and observations we wish to model. In this chapter we describe the input parameters that must to be considered in order to simulate the nebular emission using CLOUDY, and how we utilize the PYCLOUDY's capabilities.

3.1 1D photoionization model: CLOUDY

CLOUDY is a spectral synthesis code, which simulates the conditions of an interstellar cloud from a static 1D simulation. This code has a wide range in the variation of the physical conditions under which the cloud can be studied. For example, the temperature range extends from 2.7 K to 1.001×10^{10} K, which allows us to simulate the physical conditions of a completely molecular and even a completely ionized cloud(for more detail see Ferland et al., 2017, and documentation). CLOUDY predicts the spectrum of the cloud, as well as the thermal, ionization, and chemical structure.

CLOUDY uses as input parameters: (i) the stellar properties (luminosity and spectral shape), (ii) the nebular properties (abundances and density profile), and (iii) dust properties (species, size distributions, and dust-to-gas ratio). The calculations presented in this thesis were performed with version 17.01 of CLOUDY, last described by Ferland et al. (2017).

M 1-67 and RCW 58 are nebulae around very luminous stars, so we can assume that in both nebulae the gas is fully ionized. On the other hand, CLOUDY has the flexibility to implement input data that are not found in the default data, so we consider the code to be the ideal one to carry out a detailed study of our study objects. Although, since the simulation performed by the code is static, effects produced by the movement of the material would not be taken into account in the calculations, which could cause the flux of some emission lines produced by shocks of the stellar wind on the nebular material to be underestimated.

3.2 Stellar atmosphere

The stellar spectrum is key to obtaining a self-consistent modelling of a nebula. The spectra of WN-type WR stars are the result of non-LTE radiative transfer through expanding atmospheres including line-blanketing by iron and iron-group elements (Gräfener, Koesterke, & Hamann, 2002) and, as such, the spectral shape departs strongly from that of a blackbody spectrum. In particular, the absorption of UV photons drives powerful stellar winds, which have a ratio of mechanical to radiation momentum much larger than unity due to multiple scattering. Detailed synthetic spectra should be used when modelling the observable properties of nebulae around WR-type stars (see, e.g., Reyes-Pérez et al., 2015; Gómez-González et al., 2022) and in this thesis, we use the Potsdam Wolf-Rayet (PoWR) model atmospheres (Hamann et al., 2006), which have been developed and refined over many years, and include effects such as line-blanketing and clumping in the wind.[13]

WR 40 and WR 124 were given the spectral classification WN8h on the basis of its optical spectrum (Smith & Aller, 1969; Smith, Shara, & Moffat, 1996). Hamann et al. (2006, 2019) modelled the atmosphere of these stars with the PoWR code and the best fit in $R_t - T_\star$ space to the *IUE* flux and narrow-band visual photometry is model 06-14 from the WNL-H20 grid of models for both. Here, R_t is the transformed radius, related to the mass-loss rate $\dot{M}$ as

$$R_t = R_\star \left\{ \frac{v_\infty}{2500 \text{ km s}^{-1}} \middle/ \frac{\dot{M}\sqrt{D_\infty}}{10^{-4} M_\odot \text{yr}^{-1}} \right\}^{2/3},$$

(3.1)

where $R_\star$ and $T_\star$ are the stellar radius and temperature defined at a Rosseland optical depth of 20, v_∞ and $M_\odot$ are the stellar wind velocity and (clumped) mass-loss rate, and D_∞ is a clumping factor. Models with the same stellar temperature and transformed radius produce resultant spectra having the same equivalent widths (Schmutz, Hamann, & Wessolowski, 1989). This scaling relation means that the different sets of values of $(R_\star, v_\infty, M_\odot, D_\infty)$ can give the same stellar spectrum.

Herald, Hillier, & Schulte-Ladbeck (2001) performed a detailed modelling for WR 40 using line-blanketed and non-LTE model atmospheres. Herald, Hillier, & Schulte-Ladbeck (2001) found that their best model was achieved with values (10.6 $R_\odot$, 840 km s^{-1}, 3.2×10^{-5} $M_\odot$yr^{-1}, 10) together with $T_\star$ = 45.4 kK, where v_∞ was adopted from Crowther et al. (1995). The corresponding value of the transformed radius is R_t = 5.16 $R_\odot$. On the other hand, Hamann et al. (2006, 2019) using the stellar atmosphere code PoWR, find a good model fit to WR 40 corresponding to the set of values (14.5 $R_\odot$, 650 km s^{-1}, 6.3 × 10^{-5} $M_\odot$yr^{-1}, 4) together with $T_\star$ = 44.7 kK, which take into account the corrections for the new *Gaia* distances (Rate & Crowther, 2020). For this set of values, the transformed radius is R_t = 5.27 $R_\odot$. Hence the two quite different sets of numbers lead to very similar

---

13 http://www.astro.physik.uni-potsdam.de/~wrh/PoWR/powrgrid1.php

model parameters. In the case of WR 124, Hamann et al. (2006, 2019) reported a good fit corresponding to $(11.93\,R_\odot, 710\,\mathrm{km\,s^{-1}}, 5\times10^{-5}\,\mathrm{M_\odot\,yr^{-1}}, 4)$ and $T_\star = 44.7$ kK.

Hamann et al. (2006, 2019) recommend using their model labelled 06-14 from the WNL-H20 grid with Galactic metallicity for WR 40 and WR 124, which corresponds to $\log R_t = 0.7$, $T_\star = 44.7$ kK and a surface hydrogen abundance of 20 per cent by mass. Details of this model and the grid-adjacent model 06-13, which has $\log R_t = 0.8$, are listed in Table 3.1. We note that the main difference in increasing R_t is the higher rate of helium-ionizing photons. In Fig. 3.1, we show the comparison between the synthetic spectrum WNL 06-14 obtained with the PoWR model atmosphere code and blackbody radiation with the same effective temperature, as well as model WNL 06-13 for comparison. Both models were downloaded from the PoWR database. The model atmosphere is extremely deficient in EUV photons compared to the blackbody spectrum due to photon reprocessing in the stellar wind-driving region.

The stellar luminosity, temperature, and radius are related through the Stefan-Boltzmann law. The radius, luminosity, and mass-loss rate can be scaled with distance using the transformation law described by Equation 3.1. The luminosity of WR 40 can be estimated using the v magnitude, the reddening law R_v, E_{b-v} and an assumption as to either the distance d or the absolute magnitude M_v. Using the most recent distance of 3.83 kpc (Rate & Crowther, 2020), we have rescaled both the Herald, Hillier, & Schulte-Ladbeck (2001) luminosity and the Hamann et al. (2019) luminosity and in each case we obtain $\log(L/L_\odot)= 5.9$, so this is the value we adopt in our models. The POWR grid of models is normalized to $\log(L/L_\odot)= 5.3$, so the hydrogen and helium ionizing photon rates listed in Table 3.1 should be scaled. On the other hand, we rescaled the luminosity of WR 124 calculated by Hamann et al. (2019) to our adopted distance of 6.4 kpc and obtained a luminosity of $\log(L/L_\odot)= 5.76$ for WR 124. The WN8h class stars are among the most luminous stars known.

3.3 Dust properties

The photospheres of evolved massive stars are oxygen-rich, rather than carbon-rich, due to nucleosynthesis by the CNO cycle in the core, which favours the production of ^{14}N at the expense of ^{12}C. The most abundant monomers in the material ejected by O-rich stars are Fe, Mg, SiO and H2O, and to a lesser degree Ca and Al. Condensation of the grains begins at $T > 1500$ K, however, at temperatures $1200 > T > 800$ K gives the greatest grain coagulation, which occurs between amorphous SiO with more monomers (see Whittet, 2003, and references therein). The dust formed in RSG and LBV stars should therefore be primarily calcium-magnesium-iron silicates, such as olivine ($MgSiFeO_4$), and metal oxides, such as aluminia (Al_2O_3) (see e.g. Gail et al., 2005; Cherchneff, 2013). However, the dust production process in massive stars is still poorly understood and is highly dependent on the particular physical and chemical conditions
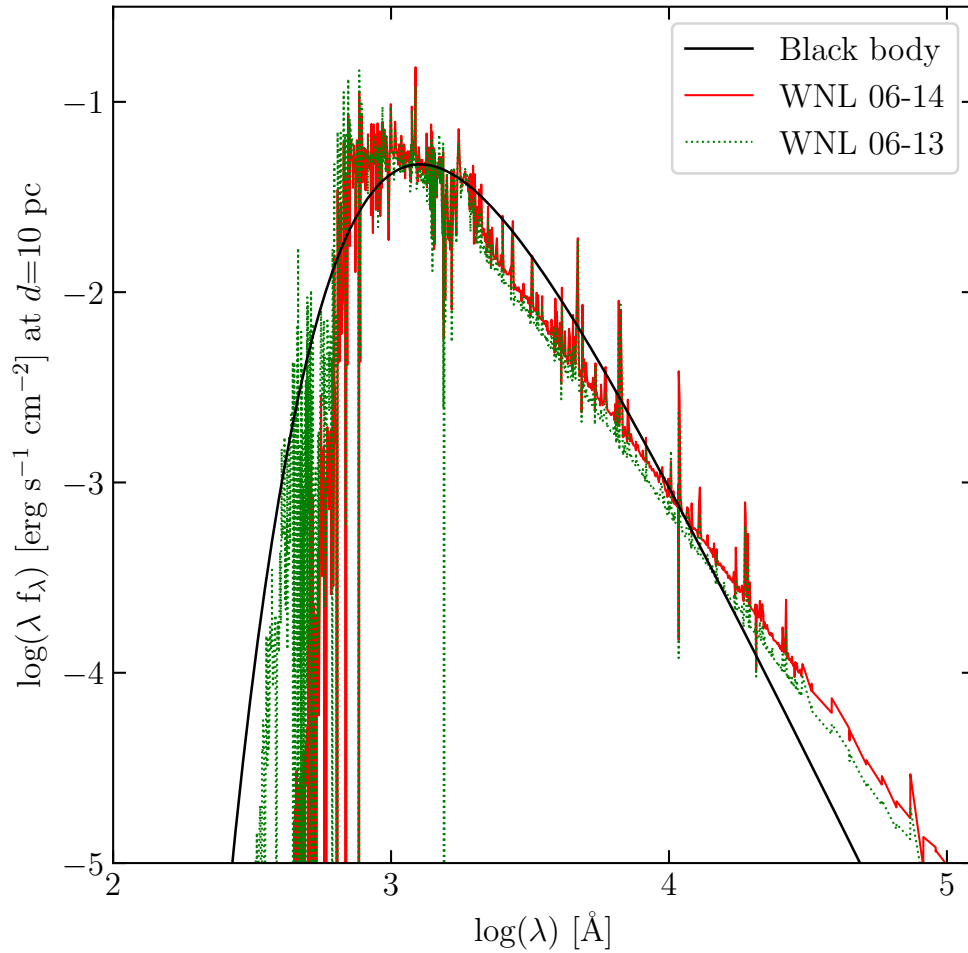
Figure 3.1: Comparison between black body emission and PoWR stellar atmosphere models. The black line represents the black body spectrum with an effective temperature of $T_{\text{eff}} = 28.8\,\text{kK}$. Solid (red) line: best-fit model to WR 124 and WR 40 determined by Hamann et al. (2006) corresponding to model WNL 06-14 ($T_{\text{eff}} = 28.8\,\text{kK}$). Dashed (green) line: model WNL 06-13 ($T_{\text{eff}} = 32.1\,\text{kK}$).

Table 3.1: Parameters of POWR Models WNL 06-13 and WNL 06-14 used to model the nebular and dust properties of M 1-67 with CLOUDY. WNL 06-13 is adopted in this work to be the stellar atmosphere in our models, while WNL 06-14 was found by Hamann et al. (2006) to be the best fit to the stellar spectrum of WR 40 and WR 124. $T_\star$ and $T_{2/3}$ are the effective temperatures at $\tau = 20$ and $\tau = 2/3$, respectively.

Model	WNL 06-13	WNL 06-14
X_H [%]	20	20
$T_\star$ [kK]	44.7	44.7
$R_\star$ [$R_\odot$]	7.5	7.5
$\log_{10} R_t$ [$R_\odot$]	0.8	0.7
$T_{2/3}$ [kK]	32.1	28.8
$R_{2/3}$ [$R_\odot$]	14.4	17.9
$\log_{10} Q_H$ [s^{-1}]	48.95	48.85
$\log_{10} Q_{He}$ [s^{-1}]	46.99	44.91
D_∞	4	4

in the region where it forms. For example, during the nucleation process grains tend to form disorderly (amorphous) unless the grains are heated during or after the growth process, giving rise to ordered structures (crystalline or polycrystalline).

The size distribution depends on the growth process of the solid particles and the destruction processes that occur in the dust formation region. Regions that present grain-grain collisions, such as the expanding envelopes of red giants, obey a power law grain-size distribution $a^{-3.5}$ (Biermann & Harwit, 1980). In this context, the dust in WR nebulae may have a size distribution of this form.

CLOUDY provides optical constants for carbonaceous grains (graphite, amorphous carbon, and long and short PAH molecules), silicon carbide, and astronomical amorphous silicate, namely olivine ($MgFeSiO_4$) (e.g. Draine, 2003). Only the last of these is of interest for M 1-67 and RCW 58 since the dust will have formed in an oxygen-rich environment.

With CLOUDY we can include single-size spherical grains and also populations with resolved size bins between a minimum, a_{min}, and maximum, a_{max}, grain size with a power-law distribution. We assume that the grains have an MRN (Mathis, Rumpl & Nordsieck, 1977) power-law size distribution $N(a) \propto a^{-3.5}$ and use 10 bins for each resolved population. For each bin i, the ratio of maximum to minimum size a_i/a_{i-1} is taken to be constant and equal to $(a_{max}/a_{min})^{1/10}$. The dust-to-gas mass ratio (D/G) in CLOUDY can be adjusted by the user but the default value defines the Si abundance in

the silicate dust to be $3.28{\times}10^{-5}$, equivalent to the Solar value, and the mass number[14] per dust molecule is 172 (e.g. Weingartner & Draine, 2001).

3.4 3D photoionization model: PYCLOUDY

PYCLOUDY is a interface to CLOUDY (Morisset, 2006). It includes a 3D module based on python tools. PYCLOUDY runs 1D CLOUDY simulations many times, changing at each run the input parameters according to an angular law describing the morphology of the object. In order to compute a 3D model of a nebula:

1. We need to parametrize the morphology of the nebula as function of the angle. That is, the inner and the outer radii, and hydrogen density (radius dependent) vary with the angle.

2. Then, PYCLOUDY generates N input files for CLOUDY, according to the morphology. These N models have fixed parameters that define ionizing flux description, and nebular composition (gas and dust abundances).

3. Next, PYCLOUDY runs CLOUDY N times and generates N CLOUDY output models.

4. And finally, PYCLOUDY reads the N outputs of CLOUDY and interpolates them into a 3D cube in which resolution can be specified by user. The resolution of the 3D cube is better when the number of cells in the cube increases. The 3D cube contains the n_e, T_e, the emissivities of selected lines, and the ionic fractional abundances in each cell.

The main advantage of building the model inside a 3D cube is that it can be rotated, and computed surface brightness maps and emission line profiles viewed from different angles. It also allows the user to integrate emission line profiles over a given aperture shape and position. The computation time of a typical 3D model run for the cases studied in this thesis is around a few tens of minutes.

3.5 Synthetic spectra and photometry

In order to assess if a model is a good fit to the observations, we need to define some constraints. We decided that a good model should simultaneously reproduce the:

1. Ionized gas emission. From Hα, Hβ, and radio continuum observations whenever available.

---

14 Nucleon number.

2. Dust emission. From the shape and flux of the SED obtained from all IR images available for each nebula.

When we work with a specific nebula we first constrain the ionized gas emission, in order to fix the amount of gas. For a given set of input parameters, CLOUDY calculates the ionization and thermal equilibrium solution and computes the continuum and line volume emissivities as a function of radius and depth for the full spectral range from X-rays to radio wavelengths. Then, we used the PYCLOUDY library to produce surface brightness maps from the spherically (or spheroidal) symmetric emissivity results of our models. We extracted simulated optical spectra from synthetic apertures with the same angular size and position as the observation slits of the different telescopes that have observed our targets.

We constrain the dust emission from our targets by simulating broad-band infrared photometry corresponding to the *WISE*, *Spitzer*, and *Herschel* observations shown in Fig. 2.1 and Fig. 2.2. The continuum emission is integrated over each band weighted by the corresponding instrumental transmission curve[15].

In addition, we were also able to simulate photometric measurements from radio continuum observations to constrain the ionized gas emission together with the Hα and Hβ nebular fluxes (see Chapter 5).

3.5.1 The IR continuum of a dusty nebula

It is necessary to bear in mind the different spatial scales from which the observational data that we seek to adjust are taken. We required to fit our model to emission line intensities measured in specific regions of the nebula (see Figure 4.1), and the IR SED obtained from the entire nebula.

The methodology to find the best models for M 1-67 and RCW 58 consists of varying gas and dust parameters in an iterative form. Once we adjust the ionized gas emission (from Hα, Hβ or radio continuum) the dust is included in the model searching for a good approximation to IR data. However, when the dust is included into the model it is necessary to readjust the gas parameters anew because of the effect the dust absorption has on emission line intensities. In most cases it is necessary to refine the values of the gas parameters to maintain a good fit.

CLOUDY considers that the dust grains are mixed with the gas and their mass is weighted by the D/G ratio. Depending on the dust species and size distributions the resulting SED will have a specific shape and width. To put this into context, in figure 3.2 we show a cartoon of an IR SED produced by a single dust species with two different size distributions. In the leftmost panel we labeled with number 1 the small wavelength range where the star and the ionized nebula dominate. The contribution of the shape of the SED from the dust are labeled with 2, 3 and 4 in the middle and rightmost panels.

---

15 http://svo2.cab.inta-csic.es/theory/fps/index.php?mode=browse
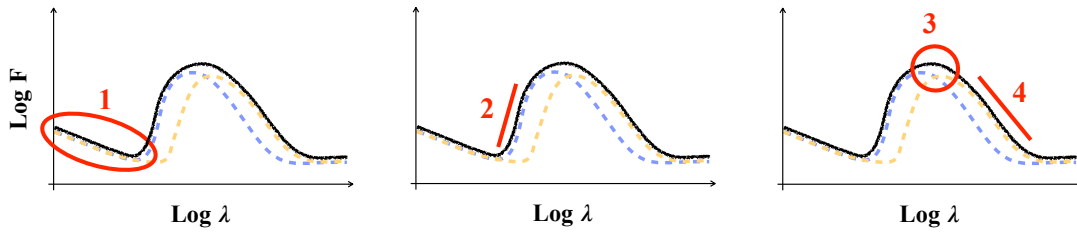
Figure 3.2: A schematic figure shows the IR wavelength continuum of a dusty nebula (solid black line): blue and yellow dashed lines show the contribution of small and large grains, respectively. The figure has three panels in which the areas of the spectrum that are directly affected by the parameters considered to model our sample of dust nebulae are shown with red marks. *Left panel:* Mark 1 indicates the region is dominated by emission from the central star and gas. *Middle panel:* Mark 2 shows the slope of the continuum at short wavelengths, it is dominated by the emission from the smallest grains. *Right panel:* Marks 3 and 4 indicate the peak and tail of the continuum, the former being dependent on the contribution of small and large grains, while the latter is largely governed only by the emission of larger grains.

A fit to the slope of the short wavelength range (number 2) of the IR bump is obtained by including the population of small grains. This requires to find the minimum and maximum value of the size distribution as well as the D/G ratio. Similarly, the slope of the long wavelength range (number 4) reflects the presence of the large population of grains. However, after including the second population of grains another parameter should be considered, this is the big-to-small grains (B/S) ratio by mass. Finally, the peak of the SED (number 3) is the result of the combination of the two dust size populations. The best fit to the observed SED is then an iterative process.

4   M 1-67

This chapter is based on the results published in the paper:

Dust in the Wolf-Rayet nebula M 1-67
Jiménez-Hernández P., Arthur S. J. Toalá J. A.; 2020, MNRAS, 497, 4128

4.1 Nebular and dust parameters

There are a number of optical spectroscopic studies of M 1-67 which have addressed the physical properties and abundances of this WR nebula. However, we selected the work of Esteban et al. (1991), rather than those of the most recent of Fernández-Martín et al. (2013), because their slit positions have a larger coverage which are representative of average conditions of M 1-67. Furthermore, we assume that M 1-67 can be modelled as a purely photoionization nebula since there are no apparent signs of interaction between a fast wind and the clumpy nebula material (Fernández-Martín et al., 2013). The kinematics of the clumps suggests an ejecta origin rather than the breakup of a swept-up shell due to instabilities (Solf & Carsenty, 1982; Grosdidier et al., 1998; Toalá & Arthur, 2011).

The distribution of nebular material in M 1-67 can be mapped from observational data. Optical images reveal that M 1-67 has a clumpy appearance, while its kinematics suggest that it is comprised of expanding hollow shell structures (Zavala et al., 2022). Grosdidier et al. (1998) show a manner to observe the spatial distribution of the nebular gas from the study of the radial distribution of the Hα emission of the nebula. They found that the radial surface brightness distribution Hα can be reproduced by a radial power-law density distribution of the form

$$n_\mathrm{e}(r) = n_0\left(\frac{r_\mathrm{in}}{r}\right)^{\alpha},\tag{4.1}$$

with power-law index $\alpha = 0.8$. Furthermore, the nebula must be density bounded with an external cutoff radius because Hα images show that the nebula is completely ionized (Grosdidier et al., 1998). Fernández-Martín et al. (2013) report electron densities of $n_\mathrm{e} \sim 1500$ cm^{-3} in the central regions of the nebula and $n_\mathrm{e} \sim 650$ cm^{-3} in the outer regions with a symmetric gradient. Sirianni et al. (1998) calculate the electron densities at 270 positions in M 1-67 and find densities as high as 2400 cm^{-3}. Vamvatira-Nakou et

Table 4.1: Chemical abundances in M 1-67 shown in $12+\log_{10}X$ notation.

	Esteban et al. (1991)[1]	Fernández-Martín et al. (2013)[2]
O	8.12 ± 0.28	7.70 ± 0.03
S	6.96 ± 0.14	6.40 ± 0.02
N	8.54 ± 0.16	8.21 ± 0.03

[1] Refers to Region A in Esteban et al. (1991).
[2] Refers to the average of regions 5 and 6 in Fernández-Martín et al. (2013)

al. (2016) make the approximation that the nebula is a spherical shell with inner radius r_{in} = 45 arcsec (Solf & Carsenty, 1982) and outer radius r_{out} = 55 arcsec (Grosdidier et al., 1998). In our models, we adopt a density distribution similar to equation 4.1 and vary n_0, r_{in}, and α in order to obtain the best fit. We also consider multiple layers and take into account the bipolar appearance of the dust emission disclosed in Fig. 2.1.

Esteban et al. (1991) derive chemical abundances for four positions in M 1-67, while Fernández-Martín et al. (2013) determined abundances for eight different regions; both studies agree that nitrogen is enriched while oxygen is deficient in the nebula as a result of processing in the CNO cycle. Their results are summarized in Table 4.1. We note, however, that the derived chemical abundances from these studies vary with position in M 1-67.

We examined the publicly available *Spitzer* IRS spectra to search for grain emission features but found no evidence for crystalline silicates at their known wavelengths 6, 11.3,19, 23, 27, and 33 μm (Henning, 2010). Accordingly, we assume that the grains are composed of amorphous astronomical silicate material (Greenberg & Li, 1996), specifically olivine ($MgFeSiO_4$), which is the default silicate grain option in cloudy.

4.2 Constraints on the models

For this nebula, we selected these specific constraints:

(i) the total observed Hα nebular flux. This was taken from Grosdidier et al. (1998);

(ii) the Hβ surface brightness F(Hβ) obtained from the Isaac Newton Telescope (INT) slit A aperture taken from Esteban et al. (1991);

(iii) the gas electron temperature T_e derived from the [N II] $\lambda\lambda$ 5755/6584 ratio from the INT slit A aperture taken from Esteban et al. (1991);

(iv) the shape and flux of the IR photometry obtained from all images shown in Fig. 2.1, illustrated in Fig. 2.4 and listed in Table 2.3.
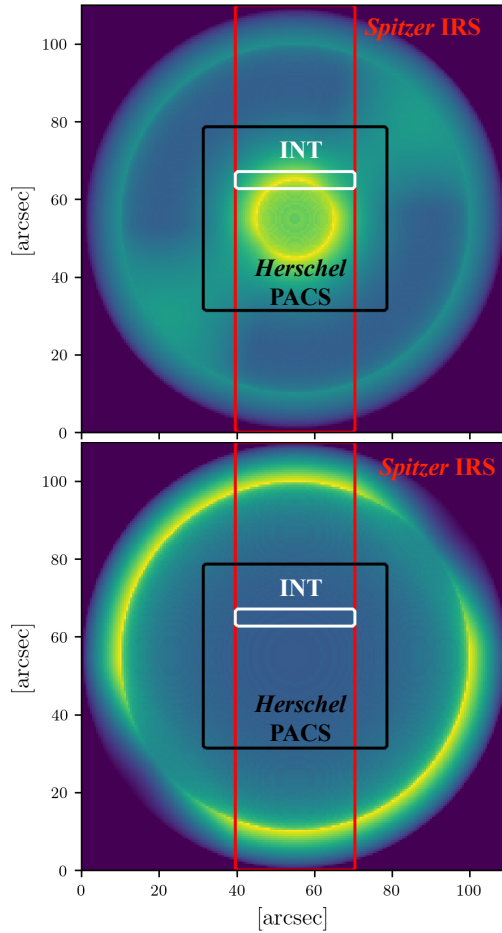
Figure 4.1: Synthetic emission maps obtained from our best model MC 6-14 calculated with PYCLOUDY. Top panel: Hβ emissivity on a logarithmic scale. Bottom panel: *Herschel* PACS 70 μm. The rectangular regions show the relative positions and sizes of apertures representing region A of the INT slit from Esteban et al. (1991) (white), footprint of the *Herschel*-PACS spectrometer (black), and the slit of *Spitzer* IRS observations (red).

We used the PYCLOUDY library (Morisset, 2006) version 0.9.8b3 (using CLOUDY version 17.01) to extract simulated optical spectra from a synthetic aperture with the same angular size and position as slit A of the INT observations presented by Esteban et al. (1991) (see Figure 4.1).

To constrain the shape and flux of the IR photometry obtained from all images shown in Fig. 2.1, we simulated to broad-band infrared photometry corresponding to the *WISE*, *Spitzer*, and *Herschel* observations.

We do not attempt to fine-tune the chemical abundances of our models and we keep them fixed at the values reported by Esteban et al. (1991). This may lead to differences between observed and model emission-line intensities for some elements, but line ratios should not be affected. We note that derived conditions across M 1-67 are not uniform due to the clumpiness of the nebula (Esteban et al., 1991; Fernández-Martín et al., 2013), but we do not model discrete clumps in the present analysis.

4.3 Results

In this section, we describe the results of a series of models varying the density distribution and the dust properties, leading to a self-consistent description of the nebular optical and IR properties of M 1-67.

4.3.1 Gas density distribution

We begin by investigating the gas density distribution. We ran a set of CLOUDY models using the PoWR 06-14 stellar atmosphere model (see Section 3.2) as input and including pure amorphous silicate grains with an MRN power-law size distribution represented by 10 size bins in the range of 0.005-0.25 μm, which is the standard ISM size distribution. We fixed the outer radius of the nebula, $r_{out} = 55$ arcsec (Grosdidier et al., 1998) and allowed the inner radius r_{in} to vary. The density in the shell obeys a power-law index and the density at the inner radius is to be determined and we assume spherical symmetry. Using the constraints of the observed total $F(H\alpha)$ flux, the $F(H\beta)$ surface brightness and the electron temperature T_e, we varied the inner radius r_{in}, the density at the inner radius n_0, and the power-law index α until the model estimates of the observed constraint parameters agreed within 25 per cent for each value. The best model, labelled as MA 6-14, resulted from the parameter values $n_0 = 2100$ cm^{-3} and $\alpha = 1.4$, bounded by inner and outer radii of 10 and 55 arcsec, respectively.

Input details of model MA 6-14 are listed in column 2 of Table 4.2. The output values of the constraint parameters for this model are given in Table 4.3. Additionally, in Table 4.4, model predicted emission-line intensities are compared to observed values at optical and IR wavelengths from different apertures. We note that although the low-ionization lines of ions such as [N II] are well reproduced by the model, higher

ionization lines, for example, [S III] are not well modelled. We attribute this to the stellar atmosphere model, which lacks photons capable of photoionizing S to S^{++} (this is discussed in Secction 4.4.1). We also note that this model produces an over-prediction of emission in the [C II] λ 158-μm line. Vamvatira-Nakou et al. (2016) interpreted this emission as being produced in a photon-dominated region (PDR), but our models are fully ionized and density bounded.

The simple model described above reproduces the gas low-ionization emission reasonably well. However, the thermal dust emission resulting from the ISM size distribution of silicate grains that are homogeneously mixed with the gas at all radii leads to the SED shown in Fig. 4.2. There is a clear excess of emission at shorter wavelengths, i.e. there is too much hot dust.
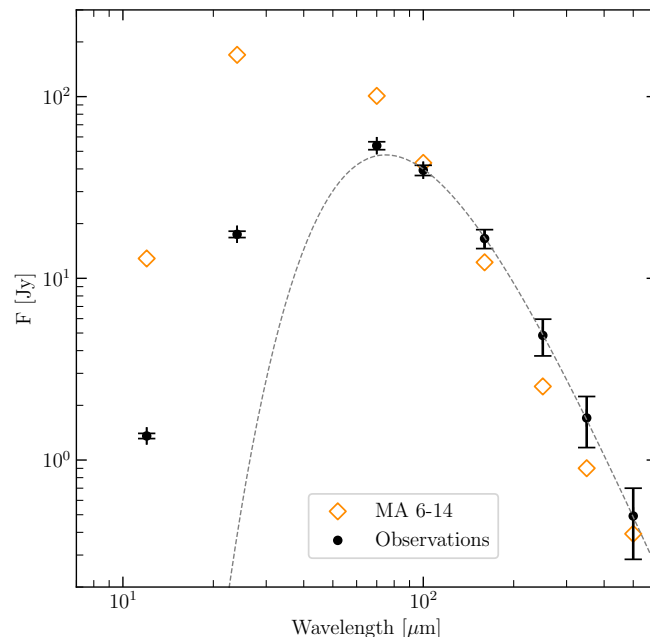
Figure 4.2: SED obtained from the IR observations of M 1-67 (black) dots (see Table 2.3). The error bars take into account uncertainties associated with the instrument calibration and the background subtraction process. The synthetic SED obtained from our model MA 06-14, is also shown with empty yellow diamonds.

The dust temperature can be lowered by either increasing the size of the dust grains or moving the dust further away from the star (see Appendix A in Gómez-Llanos et al., 2018). To better understand the distribution of dust in the nebula, we calculated the radial distribution of the surface brightness of the 70 μm emission integrated over the bipolar shape seen in Fig. 2.1. This has been done by using the CART2POL python
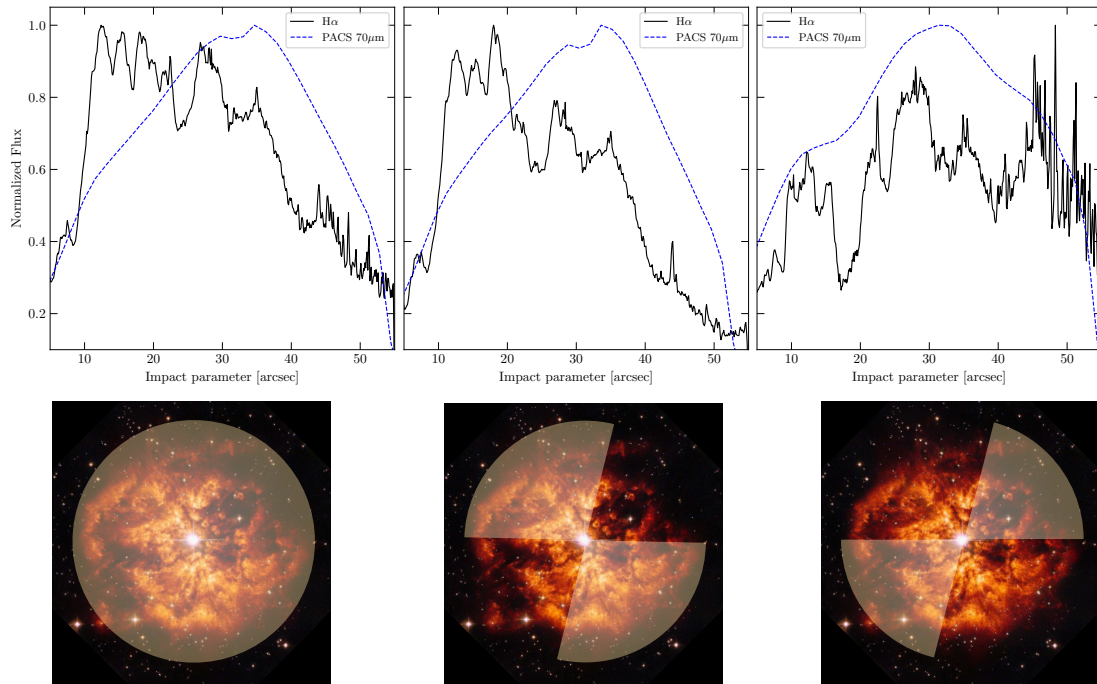
Figure 4.3: Projected radial distribution of the surface brightness integrated over a specific region of M 1-67 delimited by the angle ϕ. The angle is measured from a vertical y-axis and counterclockwise. *Top left panel:* whole nebula ($0° \leq \phi \leq 360°$). *Top middle panel:* the bipolar emission region of M 1-67 at 70 μm ($-30° \leq \phi \leq 90°$ and $130° \leq \phi \leq 230°$). *Top right panel:* regions outside of bipolar emission ($90° \leq \phi \leq 130°$ and $230° \leq \phi \leq 330°$). The solid black line is the observed Hα surface brightness. The dashed blue line is the observed surface brightness from the *Herschel* PACS band at 70 μm. *Bottom panels*: Hα image of M 1-67 indicating the sectors over which the surface brightness was integrated shown in the top panels.

routine[16]. The radial distribution of the 70 μm emission shown in Figure 4.3 strongly suggests that it originated in a shell. Furthermore, the radial distribution of the Hα surface brightness for the same bipolar region shows evidence for emission from a structure at intermediate radii (see Fig. 4.3).

The MBB fit to the long-wavelength ($\lambda \geq 100$ μm) *Herschel* emission suggested that the grains responsible for this part of the SED have a characteristic temperature of $T_D =$ 38 K. This grain population will represent the bulk of the mass of grain material in the nebula and will comprise large grains. On the other hand, small grains are necessary to produce the short wavelength thermal emission, and these grains absorb a greater proportion of the UV photons and affect the optical properties of the nebula.

---

16 https://github.com/e-champenois/cart2pol

4.3.2 Dust models

Two-shells model

Our second scenario proposes that M 1-67 is composed of an inner shell with no contribution from dust and an outer shell with gas and two populations of grains (see e.g. Gómez-Llanos et al., 2018). The inner dust-free shell is delimited by r_{in} and r_{mid}, while the outer shell material is distributed between r_{mid} and r_{out}. The region interior to r_{in} is empty.

We begin by setting r_{mid} to 45 arcsec, which corresponds to the radius of the ring of expanding clumps reported by Solf & Carsenty (1982) and Sirianni et al. (1998), and fix the outer radius at r_{out} = 55 arcsec, as before. The other parameters, that is, r_{in}, the power-law index in both shells (α_{in}, α_{out}), the density normalizations ($n_{0,\mathrm{rin}}$, $n_{0,\mathrm{mid}}$), and the filling factors (f_{in}, f_{out}) were arrived at during an exhaustive process of testing different dust grain-size distributions and dust-to-gas ratios in the outer shell while adjusting the inner shell parameters to maintains compliance with the observational constraints listed in Section 4.2. We found that the total Hα flux is most sensitive to the outer shell parameters, since that is where the bulk of the nebular mass resides, while the Hβ surface brightness is most affected by the density distribution near r_{in} where the INT aperture is located. We follow the process described in Section 3.5.1 to find the appropriate outer layer parameters that work with the dust-free inner layer to reproduce the observations consistently.

Our best spherically symmetric two-shell model, labelled MB 6-14, comprises two concentric shells: the inner, dust-free shell is delimited by r_{in} = 10 arcsec and r_{mid} = 45 arcsec has power-law index α = 2, density normalization $n_{0,r_{\mathrm{in}}}$ = 2500 cm^3, and filling factor f_{in} = 0.05, and the outer, dusty shell is bounded by r_{mid} = 45 arcsec, r_{out} = 55 arcsec has power-law index α = 2, density normalization $n_{0,r_{\mathrm{mid}}}$ = 600 cm^{-3}, and a smaller filling factor, f_{out} = 0.037. The dust properties that give a good fit to the observed IR SED combine a population of large grains of representative size 0.9 μm ('big grains') and a population with an MRN power-law size distribution between 0.005 μm and 0.05 μm ('small grains'), with a much higher proportion of big grains than small grains (high value of B/S). It was also necessary to increase the dust-to-gas ratio above the default value in the outer shell. Details of this model are listed in the third and fourth columns of Table 4.2.

Model MB 6-14 does a good job of fitting the nebular optical and IR emission lines, except those with high ionization potential ions, as well as reproducing T_{e} and n_{e} (see Tables 4.3 and 4.4). The total ionized gas mass resulting from this model is 11.26 M$_{\odot}$ and the dust mass is M_{D} = 0.22 M$_{\odot}$.

We found that dust with sizes between 0.8 and 1.0 μm (represented, for simplicity, by a population of single-size grains of size 0.9 μm), and located in the outer shell, has a very similar temperature to the characteristic dust temperature suggested by the MBB
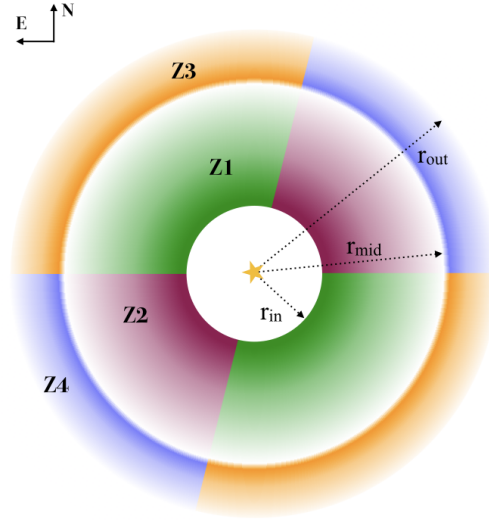
Figure 4.4: Schematic view of the distribution of gas and dust in M 1-67 used for model MC 6-14. Regions Z1 (green) and Z2 (purple) are composed purely of gas but with differing density distributions; region Z4 (blue) is also dust free and has a steeper power law to Z2; Z3 (orange) is the only region that contains dust, see Table 4.2 for details of the density distributions. The white region interior to r_{in} is completely empty of both gas and dust. The diagram depicts a vertical slice ($y = 0$ plane) of the 3D model, which must be rotated through $\phi = \pi$ and oriented with respect to the observer in order to produce the emission maps.

fit, that is $T_D \sim 38$ K (see Section 2.3.3). The shorter wavelength part of the IR SED requires a population of smaller grains with sizes in the broad range of 0.005−0.05 μm. The dust in the smallest size bin is twice as hot as the largest grains (size 0.9 μm).

Bipolar shells model

Motivated by the evident bipolar morphology revealed by the IR images (see Fig. 2.1), we introduced a further refinement to our models. PYCLOUDY enables us to use fully three-dimensional density structures and so we relaxed our assumption of spherical symmetry and defined the bipolar density distribution depicted in Fig. 4.4. The form of the density law in the different regions of the bipolar structure was guided by the surface brightness profiles depicted in middle and right panels of Fig. 4.3.

The final model, labelled MC 6-14, consistent with both the optical constraints detailed in Section 4.2 and the observed IR SED, is similar to the previous model MB 6-14 in that it requires an inner, dust-free shell and an outer shell are divided into sectors having different density distributions and, moreover, part of the outer shell is dust-free to simulate the bipolar nature of the dust emission seen in the IR images.
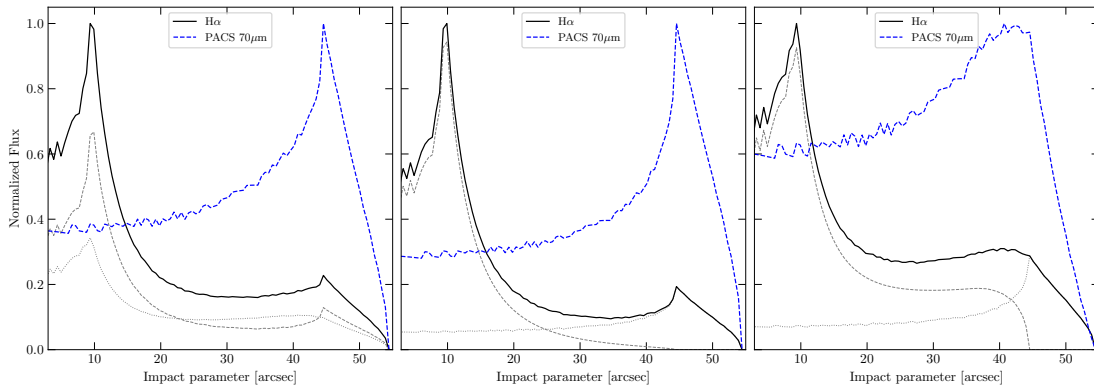
Figure 4.5: Projected radial distribution of the surface brightness from our 3D best model (MC 6-14) integrated over a specific region delimited by the angle ϕ, of a vertical slice (y = 0 plane). The angle is measured from a vertical y-axis and counterclockwise. *Left panel*: whole nebula ($0° \leq \phi \leq 360°$). *Middle panel*: the bipolar emission region of M 1-67 at 70μm ($-30° \leq \phi \leq 90°$ and $130° \leq \phi \leq 230°$). *Right panel*: regions outside of bipolar emission ($90° \leq \phi \leq 130°$ and $230° \leq \phi \leq 330°$). The solid black line is the observed H$\alpha$ surface brightness. Right panel: The dashed gray line and the dotted gray line show Zone 2+Zone 4 and Zone 1+Zone 3 contributions, respectively. Central and left panels: The dashed gray line and the dotted gray line show inner and outer zones contributions, respectively. The dashed blue line is the observed surface brightness from the *Herschel* PACS band at 70 μm.

In Fig. 4.4, regions Z1 (green) and Z2 (purple) are dust-free inner regions, region Z4 (blue) is a dust-free outer region, and region Z3 (orange) is the only region that contains dust. The density distribution in region Z1 is a steep power law, while that in region Z2 is much flatter, as suggested by the surface brightness profiles in Fig. 4.3. The outer regions, Z3 and Z4, both require a steep falloff in density but the filling factor in the dust-free sector is much lower than that in the dusty region. Full details of the parameters for this model are given in Table 4.2. In addition, we must specify the viewing angle and the placement of the apertures for the INT and PACS-simulated emission lines. In particular, the INT aperture crosses regions Z1 and Z2, illustrated in Fig. 4.1.

The simulated radial Hα surface brightness distribution of this model is shown in Fig. 4.5. The dust properties that give a good fit to observed IR SED combine a population of large grains of representative size 0.9 μm ('big grains') and a population with an MRN power-law size distribution between 0.005 μm and 0.05 μm ('small grains'). As expected, these are the same populations as we found for the two shell model discussed above and we find the same proportion of big-to-small grains. However, now that all the dust is confined to a smaller volume of the model, we require an even higher dust-to-gas ratio to explain the observation (see Table 4.2). The resultant temperature profiles for the
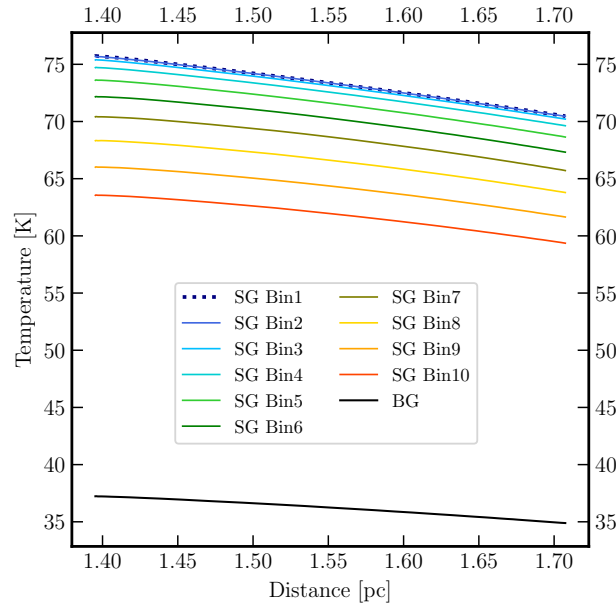
Figure 4.6: Dust temperature profiles from our best model MC 6-14. The model has 10 size bins from the population of small grains (SG) and only one of the big grains population (BG).

different grains in our model are shown in Fig. 4.6. Variations in temperature across the shell are small for a given dust-size bin but there are noticeable temperature differences between small grains and large grains.

The synthetic 70-μm radial surface brightness distribution corresponding to these grain distributions is shown in Fig. 4.5. Details of the optical and infrared emission lines of this model are presented in Table 4.4 labelled as MC 6-14. The synthetic SED obtained from MC 6-14 is shown in Fig. 4.7, where it can be seen to compare very well with the observed SED. In this figure, we also show separately the contribution from the ionized gas and that from the dust. It can be appreciated that the major contribution of the gas is around 12 μm and at 160 μm. The latter is due to the presence of the [N II] 121-μm emission line (see Table 4.4). The free-free emission from the gas also influences the total emission at the longest wavelength point at 500 μm.

We note that in order to fit the IR SED, we had to increase the dust-to-gas ratio in the outer shell (D/G) compared with that in the ISM (D/G_{ISM}). Our best model, MC 6-14, requires a dust-to-gas ratio 16 times that of the ISM and a mass ratio of big-to-small grains of B/S =20. With these values, our best, self-consistent photoionization model finds a dust mass of 0.22 M$_\odot$, with 95 per cent corresponding to the big grains, and an ionized gas mass for M 1-67 of 9.2 $^{+1.6}_{-1.5}$ M$_\odot$. Here, the errors in the estimated ionized mass
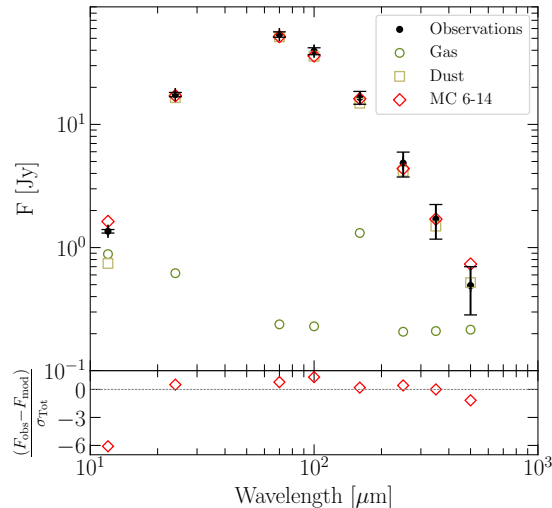
Figure 4.7: The synthetic SED obtained from our best model, MC 06-14, is also shown with empty red diamonds. The contribution to the synthetic photometry from the ionized gas and dust are also shown. SED obtained from the IR observations M 1-67 is shown with black dots (see Section 2.3.1 for details). The residuals are defined as $(F_{\mathrm{obs}} - F_{\mathrm{mod}})/\sigma_{\mathrm{Tot}}$.

were computed taking into account the errors in the Hα flux reported by Grosdidier et al. (1998).

4.4 Discussion

Our best PYCLOUDY model successfully reproduces the IR photometry corresponding to the thermal emission from the dust in the nebula and approximates the main characteristics of the photoionized gas in M 1-67. In this section, we discuss the limits of our models in accounting for all of the observed spectral features and also place our models in the context of the evolution of the central star (WR 124).

4.4.1 Gas emission lines

The gas in the nebula absorbs the majority of the ionizing photons emitted by the star, which correspond to wavelengths around the peak of the SED. The shape of the incident stellar spectrum is important: even though WNL stars have high effective temperatures, $T_{\mathrm{eff}} \sim 30$ kK, the EUV photons are reprocessed to longer wavelengths in the process of driving the strong stellar wind. The stellar spectrum that emerges is lacking in the highest energy photons, $h\nu > 25$ eV (see Fig. 3.1 and Table 3.1). Thus, the electron temperature in the nebular gas is low, $T_{\mathrm{e}} \sim 5909$ K and high ionization lines, such as [O III] $\lambda 5007$, are absent.

47

Table 4.2: Input parameters for the model sets discussed in the text.

| Parameter | MA 6-14 | MB 6-14 | | MC 6-14 | | | |
| | | Inner shell | Outer shell | Inner Shell | | Outer Shell | |
				Zone 1	Zone 2	Zone 3	Zone 4
Distance [kpc]	6.4	6.4	6.4	6.4	6.4	6.4	6.4
$\log_{10}(L_\star/L_\odot)$	5.76	5.76	5.76	5.76	5.76	5.76	5.76
$c(H\beta)$	1.9	1.9	1.9	1.9	1.9	1.9	1.9
Inner radius["]	10	10	45	10	10	45	45
Outer radius["]	55	45	55	45	45	55	55
n_0 [cm^{-3}]	2100	2500	600	2500	900	600	666
α	1.4	2.0	2.0	2.0	0.2	2.0	2.0
Filling Factor	0.05	0.05	0.037	0.05	0.02	0.0365	0.005
a_{small} [μm]	0.005−0.25[a]	-	0.005−0.05[a]	-	-	0.005−0.05[a]	-
a_{big} [μm]	-	-	0.9[b]	-	-	0.9[b]	-
B/S	-	-	20	-	-	20	-
D/G	4.03×10^{-3}	-	3.87×10^{-2}	-	-	6.33×10^{-2}	-
Gas mass [M$_\odot$]	11.87	5.48	5.78	3.29	2.19	3.41	0.35
Dust mass [M$_\odot$]	0.05	-	0.22	-	-	0.22	-

[a] Population of grains with a standard MRN grain size distribution.
[b] Population of grains represented by a single size.

Table 4.3: Emission lines used to constrain our models: [a] Total Hα flux and [b] Hβ surface brightness, both in erg cm^{-2} s^{-1} through INT slit A. The errors from the observational measurements are statistical, of order $\sim 5\%$.

Instrument	Parameter	Observations	MA 6-14	MB 6-14	MC 6-14
HST[a]	$\log_{10}F(H\alpha)$	−10.55[1]	−10.56	−10.55	−10.55
INT[b]	$\log_{10}F(H\beta)$	−13.01[2]	−13.03	−13.07	−13.105

[1]From Grosdidier et al. (1998).
[2]From Esteban et al. (1991).

Table 4.4: Line intensities considered in our models. Optical lines are relative to Hβ = 100 and infrared line measurements obtained from IRS spectra using the PAHFIT IDL routine (Smith et al., 2007) are relative to H I 12.3μm. Hβ surface brightness, F(Hβ), in erg cm^{-2} s^{-1}.The errors from the observational measurements are based on sky subtraction process, of order $\sim$ 5%.

Instrument	Line	Observed	MA 6-14	MB 6-14	MC 6-14
INT[1]	Hβ	100.0	100.0	100.0	100.0
	Hα	296.0	298.4	298.3	298.2
	[N II] 5755	0.9	0.7	0.8	0.8
	[N II] 6584	314.0	287.8	291.6	294.9
	[N II] 6548	108.0	97.6	98.9	100.0
	[O II] 3727	15.0	15.3	15.4	15.8
	[S II] 6716	13.2	17.6	17.1	17.5
	[S II] 6731	16.2	21.1	20.9	21.2
	[S III] 9068	12.0	3.5	3.7	3.7
	[S III] 9530	30.6	8.9	9.3	9.3
	F(Hβ) $\times 10^{-14}$	9.81	9.43	8.44	7.86
	T_e[N II]5755/6584	6019	5866	5894	5909
	n_e[S II]6716/6731	947	885	925	898
Spitzer	H I 12.3μm	5.2	5.2	5.2	5.2
IRS	[Ne II] 12.81μm	165.9	139.2	137.9	139.1
	[Ne III] 15.5μm	3.1	0.0	0.0	0.0
	[S III] 18.7μm	251.5	47.8	46.0	45.9
	[S III] 33.5μm	263.8	37.3	35.6	35.9
	n_e[S III]18.7/33.5	554	922	936	922
Herschel	[N II] 121μm	13.1	18.5	15.0	14.7
PACS[2]	[N II] 205μm	1.9	2.6	2.2	2.1
	[N III] 57.2μm	0.3	0.0	0.0	0.0
	[O I] 63.2μm	1.3	0.0	0.0	0.0
	[O I] 145μm	0.1	0.0	0.0	0.0
	[C II] 158μm	2.1	5.3	4.3	4.3

[1]From Esteban et al. (1991).
[2]From Vamvatira-Nakou et al. (2016), in 10^{-15} W/m^2.

In M 1-67, the observed low-ionization emission features of hydrogen, nitrogen, and sulphur in the optical spectra are consistent with the photoionization of an essentially power-law density distribution (see e.g. equation 4.1) by the WNL stellar spectrum proposed by Hamann et al. (2006), with the chemical abundances derived by Esteban et al. (1991). Our best model returns derived electron temperatures and densities from simulated emission-line ratios (see Table 4.4) within the ranges reported in the literature (e.g. Esteban et al., 1991; Sirianni et al., 1998; Fernández-Martín et al., 2013). However, our models are not able to reproduce the intensities of high-ionization species, such as [S III], which are seen in optical and *Spitzer* IRS spectra. Furthermore, the emission of the neutral [O I] 63-μm detected in selected *Herschel* PACS spatial pixels (Vamvatira-Nakou et al., 2016) is not replicated by our models.

Although our best model does produce some [S III] emission, the simulated intensities of the optical $\lambda\lambda$9068 Å and 9530 Å lines and IR 18.7-μm and 33.5-μm lines are much lower than what is observed in M 1-67. In addition, our CLOUDY models do not produce any [Ne III] or [N III] emission, which is seen in the *Spitzer* IRS and *Herschel* PACS spectra, respectively. In our photoionization model, the [S III] emission is produced primarily at the inner radius $r_{\rm in}$ by the most energetic photons of the incident stellar spectrum. It is not possible to model these high-ionization species with the adopted stellar SED (WNL 6-14), which Hamann et al. (2006) found to be a good fit to the optical and UV spectra of WR 124. A SED with a greater proportion of photons able to photoionize S to S^{++} may be required. Alternatively, we speculate that the high-ionization emission lines could be produced in shocks but such physics is not included in CLOUDY. For example, shocks could form in the 88 km s^{-1} bipolar flow detected by Sirianni et al. (1998) and Fernández-Martín et al. (2013), which is oriented in a north-west-southeast direction. Alternatively, the [S III] emission could arise close to the star where the fast stellar wind shocks against the innermost nebular material.

The other emission lines that our photoionization model does not reproduce are those of neutral oxygen. Although Esteban et al. (1991) find only upper limits for the optical [O I] λ 6300 Å line, in the infrared, the [O I] 63 μm is detected in several of the *Herschel* PACS spaxels and is strongest for those that cover bright regions of emission at 70 μm. The 63 μm line is usually emitted by neutral gas in the PDR just outside an ionization front. We speculate that this emission comes from small, dense, unresolved neutral clumps in the nebula, which are photoionized on their surface closest to the central star. The [O I] λ 6300 Å optical line emission that we would expect to see from the ionization front is simply too weak to detect from such small regions. In addition, we have inspected both the Hα image of Grosdidier et al. (1998) and the emission-line maps presented by Fernández-Martín et al. (2013) and we do not see the characteristic photoevaporated flows coming off the starward side of the condensations in the nebula that we might expect if the neutral material is the main component of the condensations we see coincident with the PACS spaxels superimposed on the 70 μm image. Fernández-

Martín et al. (2013) do find that the reddening coefficient c(Hβ) is not homogeneous across the nebula and varies between 1.3 and 2.5. There is no particularly extreme value associated with any of the blobs in the 70 μm image.

4.4.2 Dust properties

The dust-size distribution predicted by our models consists of two populations: the first has an MRN power-law size distribution with $a_{\min}$ = 0.005 μm and $a_{\max}$ = 0.05 μm and a power-law index $q = -3.5$. The second population consists of large grains with representative size a_{big} = 0.9 μm, which are necessary to reproduce the $\lambda \geq 100$ μm *Herschel* photometry. We find that a mass proportion between big grains and small grains of B/S = 20 is required. The maximum size of the grains is considerably smaller than that predicted by Vamvatira-Nakou et al. (2016), whose pure dust model required a population of large dust grains up to 10 μm in size to model the *Herschel* photometric observations. In our models, the gas absorbs and processes most of the ionizing photons, so it is not necessary to have such large dust grains to reproduce the dust temperature indicated by the photometry (see Section 4.3.2). A maximum grain size a_{big} = 0.9 μm is much easier to explain than 10 μm. Kochanek (2011) showed that dust formation in the winds of evolved massive stars $M_{\mathrm{ZAMS}} \geq 40$ M$_\odot$ most likely occurs through eruptive events in an LBV phase, such as the 'great eruption' of η Carina. This is because the mass-loss rate $\dot{M}$ needs to be high enough to shield the dust formation region from soft UV photons. Mass-loss rates $\dot{M} \geq 10^{-2}$ M$_\odot$ yr^{-1} are required to obtain $a_{\mathrm{big}} > 1$ μm. The maximum grain size of our best-fitting model is a_1 = 0.9 μm, which requires mass-loss rates above $\dot{M} > 10^{-3}$ M$_\odot$ yr^{-1} (see Fig.2 of Kochanek, 2011). An eruptive scenario would be consistent with the kinematic evidence of M 1-67 presented by Sirianni et al. (1998), which consists of a hollow shell of clumps expanding at 46 km s^{-1} centred on WR 124. The second N-rich bipolar kinematic component with expansion velocity $\sim$ 88 km s^{-1} (Sirianni et al., 1998; St-Louis et al., 2017) is not spatially coincident with the dust emission shown in our Fig. 2.1.

Our estimate for the total mass of dust in M 1-67 is M$_{\mathrm{D}}$ = 0.22 M$_\odot$, of which 0.206 M$_\odot$ corresponds to the largest size grains, a_{big} = 0.9 μm. This is $\sim$2/3 smaller than the dust mass obtained from the MBB model (see Section 4.3.2) and suggests that the standard Milky Way normalization $\kappa_{\nu 0}$ value is not appropriate for M 1-67. Indeed, the normalization value $\kappa_{\nu 0}$ includes the standard Milky Way hydrogen-to-dust ratio, set to H/D = 90 (Draine, 2003; Bianchi et al., 2019), but we have found that a much higher proportion of dust is required in this nebula.

Increasing the mass of silicate grains by a factor of 16 as required by our model is puzzling and needs some further discussion, since the underlying assumption was that virtually all of the available silicon atoms were locked up in dust grains (see Section 3.3 and Weingartner & Draine, 2001). Thus, to increase the mass fraction, we would require more silicon atoms than are available. A possible explanation is a

nucleosynthesis event such as that proposed by Podsiadlowski et al. (2010) through an explosive common envelope (CE) ejection scenario, but we calculate that the energy liberated in fusion reactions to produce the atoms needed for the extra silicate dust grains is 9.7×10^{-7} erg nucleon^{-1}. That is, the energy to convert 0.22 M$_\odot$ into dust is 2.50×10^{50} erg. This amount of energy would result in the surrounding envelope being expelled at velocities far higher than the 46 km s^{-1} expansion velocity observed in the shell. This scenario is therefore unlikely, also, it would occur very close to the end of life of the star, for which there is no evidence.

A more viable explanation is that the silicate grains have different optical properties to the spherical grains assumed in our models. For example, Siebenmorgen, Voshchinnikov & Bagnulo (2014) find that spheroidal[17] grains have far-IR absorption cross-sections a factor of 1.5–3 larger than spherical grains with the same volume. Dust masses estimated without taking this into account would be overestimated by the same factor. Additionally, Gómez-Llanos et al. (2018) found that the emission of spheroidal grains is shifted to longer wavelengths in comparison with spherical grains. If the grains are fluffy, that is, porous aggregates of smaller grains, the absorption cross-sections will be even higher and a much smaller mass of grain material would be required to reproduce the observed IR SED. We intend to explore different grain properties in future work.

4.4.3 Mass loss and stellar evolution

Our PYCLOUDY model MC 6-14 finds the ionized gas mass in the nebula to be $9.2^{+1.6}_{-1.5}$ M$_\odot$. The estimated mass for the central star WR 124 is 22 M$_\odot$ (Hamann et al., 2019), which means that the initial mass for this star was at least 31 M$_\odot$. If we take into account mass loss during main-sequence evolution where single stars with ZAMS masses above 30 M$_\odot$ can lose $\sim$ 10 M$_\odot$ (Ekström et al., 2012; Georgy et al., 2012), the initial mass for WR 124 could easily be $>$ 40 M$_\odot$.

We can estimate the average mass-loss rate of the star during the dust formation stage. Assuming a constant expansion velocity of 46 km s^{-1}, the elapsed time between the ejection of the outer (r_{out} = 55 arcsec) and inner (r_{in} = 45 arcsec) edges of the shell is 6.6×10^3 yr, where we have taken the distance to the nebula to be 6.4 kpc. According to our model, the mass of gas corresponding to the shell is 3.98 M$_\odot$ and thus the mass-loss rate when the shell was expelled is of order $\dot{M}_{\text{shell}} = 6 \times 10^{-4}$ M$_\odot$ s^{-1}. This is within the range of values listed for mass-loss rates of known Galactic LBVs with dusty shells (see Table 1 in Kochanek, 2011).

We have discussed WR 124 and its surrounding nebula in the context of single massive star evolution. *Hipparcos* light curves over the 3-yr period 1990–1993 show no evidence of periodic variability, so any binary companion would have to be very low mass. However, Toalá et al. (2018) recently speculated that the marginal detection of hard

---

17 Ellipsoids of revolution.

X-rays from WR 124 does not rule out the presence of a compact object such as a neutron star embedded within the dense stellar wind of the WN8 star. That means that the evolutionary scenario for WR 124 would include substantial mass transfer at some point (De Donder, Vanbeveren & van Bever, 1997). De Marco (2009) argue that binary interactions in the evolution of the common envelope give rise to a high mass loss in the equatorial plane, which generates a bipolar nebula. So bipolar distribution of the thermal dust emission in M 1-67 at all wavelengths further supports a binary system origin.

In a close binary system, CE evolution can lead to the ejection of the CE and produce a tighter binary (Ivanova et al., 2013, and references therein). In the current literature, different mechanisms have been proposed as energy sources that can eject the CE. Once the CE forms, frictional drag causes the secondary component of the binary to spiral-in and orbital energy is transferred to the envelope. If enough energy is transferred, a substantial fraction of the envelope can be ejected. If the gas in the envelope can recombine and form molecules during the ejection event, the recombination energy can be an additional driving mechanism for the envelope ejection (Ivanova et al., 2013). On the other hand, if we identify the shell between 45 arcsec and 55 arcsec in our model with the observed clumpy ring expanding at 46 km s^{-1} (Solf & Carsenty, 1982; Sirianni et al., 1998), then the kinetic energy of the shell is of order 8×10^{46} erg, which is similar to that estimated for outbursts in recent optical transient events that have been associated with mass-transfer processes in binary systems (Kashi & Soker, 2010). Such accretion processes can also power the ejection of a CE. However, we estimate the time-scale for the ejection event in M 1-67 through this mechanism to be much longer than, for example, the Great Eruption of the massive binary system η Carine, which occurred over 20-yr period in the mid-19th century. This suggests that the spiral-in scenario is more likely, since this can occur over many dynamical time-scales (Ivanova et al., 2013).

The ejecta of CE systems have been shown to be an ideal environment for dust formation, which can form more efficiently in certain CE conditions than in the envelopes of cool stars (Lü, Zhu, & Podsiadlowski, 2013). Which is very convenient for us, since our model suggests a high rate of mass loss so that grains as large as 0.9 μm could have been condensed. As well as the bipolar morphology seen in infrared images it can be explained by the interaction of a binary system. Also, Iaconi et al. (2019) have modelled the asymptotic behaviour of the CE expansion after the end of the dynamic in-spiral and found that it evolves into an ordered, shell-like structure at late times. This may explain the observed clumpy ring expanding observed in the optical counterpart of M 1-67. Finally, a CE phase is now thought to be one of the main routes to producing Type Ib supernovae, where the progenitors lose their hydrogen envelopes and become WR stars before exploding some 10^4–10^6 yr later, depending on the stage of evolution where the mass transfer occurs (Podsiadlowski, Joss & Hsu, 1992).

The analysis of the IR data in combination with a self-consistent photoionization model, able to reproduce both the dust and nebular properties of M 1-67, lead us to conclude that this WR nebula has not formed by the classic wind-wind interaction scenario, nor an eruptive LBV channel characteristic of single massive star evolution. We suggest that M 1-67 has formed as the result of the ejection of a CE of a binary system. If this is true, this would make M 1-67 and its progenitor star, WR 124, the first direct evidence of the post-CE scenario in massive stars.

5 RCW 58

This chapter is based on the results published in the paper:

Dust in RCW 58: Clues to common envelope channel formation?
Jiménez-Hernández P., Arthur S. J., Toalá J. A. Marston, A. P.; 2021, MNRAS, 507, 3030

5.1 Nebular and dust parameters

A global model of the dust and nebular properties of RCW 58 is hampered by extended background emission in the northern part of the nebula. For this reason, regions RC and LC (see Section 2.3.2) have been selected as representative of the properties of the ring nebula. Whilst LC does not appear to be special at any wavelength, RC harbours the region with highest average electron density as derived from the ATCA observations. Following our previous work on M 1-67 (see previous chapter and Jiménez-Hernández, Arthur, & Toalá, 2020), we modelled the gas and dust properties of these two regions.

RCW 58 consists of slow-moving clumps of photoionized stellar ejecta enveloped by a shell of low-density material swept-up by the wind-blown bubble of the central star (Chu, 1982; Smith et al., 1988; Gruendl et al., 2000). The shell is detected as a faint [O III] emission extending beyond the Hα clumps and corresponds to the outer shock of the wind bubble. The photoionized clumps form a roughly elliptical ring (see the top-left-hand panel of Fig. 2.2) and often have sharp inner edges and diffuse outer edges (Chu, 1982).

Electron densities have been estimated using the [S II] $\lambda\lambda$ 6617,6731 doublet and values between 200 and 500 cm^{-3} were reported for positions corresponding to our region LC (Smith et al., 1988), although the uncertainties are of the same order since the emission lines are very faint. More recently, Esteban et al. (2016) derived $n_\mathrm{e} = 100 \pm 100$ cm^{-3} from the [S II] $\lambda\lambda$ 6717,6731 doublet observed using the 6.5 Magellan Clay Telescope. For these observations, the 10×1 arsec^2 slit was positioned in the brightest region of the RC clump. Stock, Barlow & Wesson (2011) also derived electron densities close to the low-density limit using the [S II] $\lambda\lambda$ 6717,6731 doublet from spectroscopic observations across the south-west of RCW 58. Given the large uncertainties, these reported electron densities are entirely consistent with our values determined from the ATCA radio observations (see Section 2.4).

The chemical abundances in the nebula were studied by Kwitter (1984), Rosa & Mathis (1990), and Esteban et al. (2016). Rosa & Mathis (1990) remarked that RCW 58 is

Table 5.1: Chemical abundances in RCW 58 used in our CLOUDY models.

Element	$12+\log_{10}(X/H)$	Reference
He	11.23±0.02	Méndez-Delgado et al. (2020)
O	8.60±0.16	Méndez-Delgado et al. (2020)
N	8.67±0.18	Méndez-Delgado et al. (2020)
S	7.02±0.12	Esteban et al. (2016)
Ar	6.44±0.24	Esteban et al. (2016)
Fe	6.87±0.38	Esteban et al. (2016)

such a low ionization nebula that it is difficult to reliably determine He/H because He abundance can mimic a lower stellar effective temperature since all the available helium-ionizing photons are absorbed in the inner part of the nebula. Note that for the stellar atmosphere models described above (see Section 3.2), the stellar effective temperature, defined at an optical depth of $\tau = 2/3$, is much lower than $T_\star$; in particular, $T_{\text{eff}} \sim 28$ kK for these models. All of the cited works find evidence for strong nitrogen and helium enrichment in RCW 58, although the exact helium abundance is very uncertain. Such enrichment is an indication that CNO-cycle nucleosynthesis products are present in the stellar ejecta material. In Table 5.1 we list the chemical abundances reported by Esteban et al. (2016) and Méndez-Delgado et al. (2020), which are the ones we adopt for our CLOUDY models.

Finally, the first direct determination of the electron temperature in RCW 58 was made by Esteban et al. (2016), who obtained the value $T_e = 6450 \pm 220$ K using the [N II] 5755/(6548 + 6584) emission-line diagnostic ratio.

The dust mixture in RCW 58 can be expected to consist of amorphous silicates such as olivines (oxygen-rich magnesium iron silicates: $(Mg,Fe)_2SiO_4$) and pyroxenes (oxygen-deficient magnesium iron silicates: $(Mg,Fe)SiO_3$), together with metal oxides, in particular corundum (aluminium oxide Al_2O_3) (Tamanai et al., 2017). In the absence of mid-infrared spectra for RCW 58, we cannot confirm or rule out any of these dust species. However, oxygen-deficient amorphous silicates have a lower peak opacity and a lower near-IR absorptivity compared to oxygen-rich silicates (Ossenkopf, Henning & Mathis, 1992), so if the dust were composed primarily of pyroxene a larger mass of dust would be required to model the IR SED. Corundum has an emissivity peak in the 12 μm spectral region (Onaka, de Jong & Willems, 1989) but, since Al is 10 times less abundant than Si, we anticipate the contribution of corundum to the far-IR SED to be much lower than either olivine or pyroxene. Further analysis is beyond the scope of this thesis. Following the analysis of M 1-67 (see Chapter 4), we select spherical, amorphous silicate grains (olivine) whose optical properties are included in CLOUDY.

As part of our modelling procedure, we adjust the grain size range and dust-to-gas

ratio until we fit the IR SED. Mathis et al. (1992) suggested two populations of grains were required to explain the IR observations of RCW58: one with sizes between 0.002 and 0.008 μm, and another with sizes between 0.005 and 0.05 μm located at a larger distance from the star. These findings were based on *IRAS* fluxes at 25, 60, and 100 μm, where the 100 μm flux was highly uncertain due to background variation.

5.2 Constraints on the models

The specific constraints to model the two selected clumps located in RCW 58, RC an LC regions, are listed below:

  (i) the shape and flux of the IR photometry obtained from all images shown in Fig. 2.2, illustrated in Fig. 2.7 and listed in Table 2.4;

 (ii) the nebular free-free emission at v_0 = 2.735 GHz obtained by ATCA. (Note that this is instead of the Hα flux that we used in Chapter 4);

(iii) the gas electron temperature, T_e, determined from the [N II] $\lambda\lambda$ 5755/6584 emission-line-ratio for an aperture corresponding to the Magellan Clay telescope observations of Esteban et al. (2016);

 (iv) the optical (Hα) and IR radial surface brightness distributions. For this purpose we extracted surface brightness profiles from the images shown in Fig. 2.2 for regions corresponding to the LC and RC clumps using the CART2POL routine[18]. The resulting profiles are shown in the top panels of Fig. 5.1.

5.3 Results

In this section, we describe our CLOUDY photoionization models that best reproduce the optical, IR, and radio properties of regions LC and RC clumps in RCW 58. We used the PYCLOUDY library (Morisset, 2006) version 0.9.8b3 and CLOUDY version 17.01.We performed preliminary calculations using a shell of pure gas with appropriate density and chemical abundances together with the stellar atmosphere model WNL 06-14 described in Section 3.2. We found that this stellar atmosphere model has insufficient UV photons to produce the He I and [N II] line strengths while at the same time exceeds that of the [S II] lines when compared to the spectroscopic observations of Esteban et al. (2016). For this reason, we also ran CLOUDY models using atmosphere WNL 06-13, which corresponds to a slightly larger transformed radius, R_t and has a higher helium-ionizing photon rate (see Table 3.1).

---

18 https://github.com/e-champenois/cart2pol
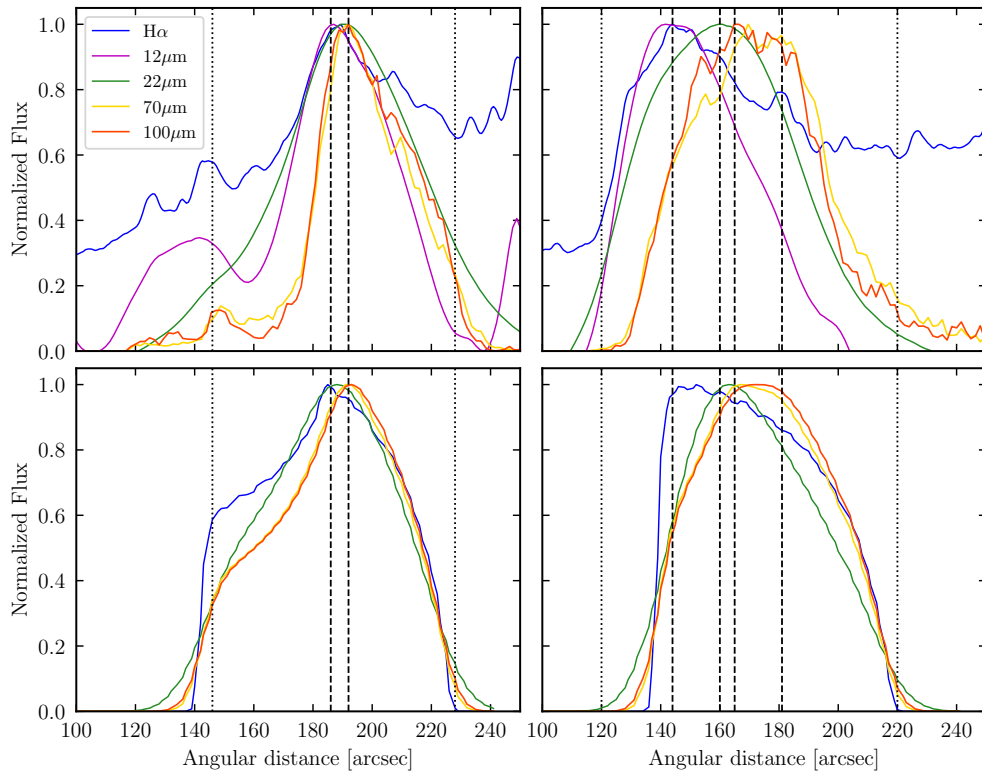
Figure 5.1: *Top panels.* Surface brightness profile as a function of angular distance from the star integrated over LC (PA: $196° \leq \theta \leq 218°$ - left) and RC (PA: $122° \leq \theta \leq 150°$ - right) clumps. Different colours represent profiles obtained from different instruments. The dashed vertical lines show the position of the emission peaks whilst dotted lines denote the inner and outer radii of the RC and LC regions. *Bottom panels.* Simulated surface brightness profiles obtained from our best models of the LC (left) and RC (right). The colour code is the same as for the top panels.

From Fig. 5.1 we see that there are unambiguous differences in the dust distribution between LC and RC. In both regions, the peak of the *WISE* 12 μm profile coincides with that of the Hα emission lines from the ionized gas (see, e.g. Mathis et al., 1992; Toalá et al., 2015). For LC, the peaks of the optical and the IR profiles are almost coincident. The 70 and 100 μm IR profiles extracted from the *Herschel* PACS observations are only offset 6 arcsec behind that of the optical emission. The 22 μm *WISE* emission peaks at the same position as the PACS profiles but is much broader due to the lower spatial resolution of these observations. On the other hand, the RC profiles suggest a more stratified distribution of dust. For example, the offset between the peak of the optical profile and those of the *Herschel* profiles is 21 arcsec, with the *WISE* 22 μm emission peaking at an intermediate position.
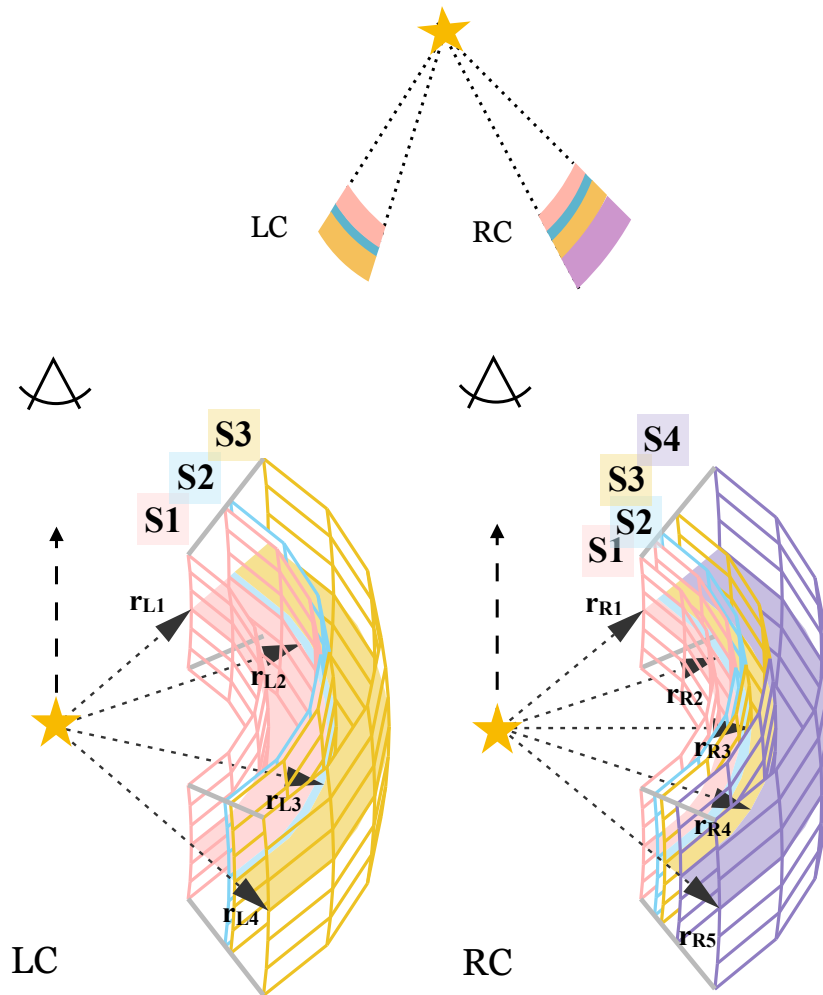
A schematic view of the gas and dust distributions for the LC and RC models is shown in Fig. 5.2. The 3D geometry assumed for each of LC and RC is that of a wedge-shaped sector of a 3D ring whose plane-of-the-sky cross-section is an annulus sector with diagonal $w^2 = r_{out}^2 - r_{in}^2$, and whose line-of-sight depth is the chord length between the 2 points where the tangent to the inner radius r_{in} intersects the outer boundary at r_{out}. Generally, the assumed line-of-sight depth is a few times (~ 5.5) the distance $r_{out} - r_{in}$.

Multiple regions were required to model LC and RC and their characteristics are described in detail below. The fitting procedure is iterative and can be described as follows. From the surface brightness profiles, we fix the inner and outer radii of the density distributions, which we take to be constant in each layer. For each layer of the LC and RC there are then eight free parameters: the hydrogen density n, filling factor ϵ, and grains defined by size ranges (a_{min}, a_{max}) for the two populations, the big-to-small grain population ratio B/S, and the dust-to-gas mass ratio D/G. The combination of n and ϵ parameters are used to model the ionized gas emission, and together they determine the synthetic 12 μm and 2.7 GHz photometries, as well as the resultant emission lines. We choose values of n from the range derived from the ATCA observations (see Section 2.4) and the corresponding value of ϵ is that which is required to give a good fit to the 2.7 GHz and 12 μm photometric points.

Once the model hydrogen density and filling factor have been determined, we turn to the dust grains. The big grain population is selected so that the model dust emission fits the peak of the IR part of the SED as well as the slope at longer wavelengths. This slope is determined solely by the large grain population a_{big}. A population of small grains a_{small} is then needed to complete the shorter wavelength part of the SED and this is determined by adjusting its size range, and the D/G and B/S ratios. In Section 3.5.1 we describe the procedure to fit IR SED considering a shell, however, for RCW 58 we model multilayer regions with more than one of them with dust. In this case, we vary the dust parameters in each layer at the same time.

In Appendix B, we show the results of some experiments in the parameter space

Figure 5.2: Schematic view of the gas and dust distributions in the LC (left panel) and RC (right panel) clumps. The innermost (white) regions are gas and dust free. Regions S1 contain only gas, S2 contain small grains, while regions S3 and S4 contain a combination of distinct populations of small and large grains. The properties of each layer are described in Sections 4.1 and 4.2. The clumps are taken to be pieces of a thick ring viewed pole-on, as illustrated in the upper figure, and the line-of-sight depth is ~5.5 times the plane-of-the-sky width. In the 3D views, the clumps have been tilted at 40° to the line-of-sight, to aid visualization of the different regions.

$(n_0, a_{big}:a_{min}, a_{max})$ and how these key parameters are the ones which determine the model SED.

5.3.1 The LC model

We found that three layers were required to account for the observational properties of LC. These regions were defined with reference to the surface brightness profiles of the top left-hand panel of Fig. 5.1. The gas densities are inspired by ATCA results described in Section 2.4 and depicted in Fig. 2.8. We report the results obtained using the stellar atmosphere model WNL 06-13. In the following, all radii are measured from the central star and converted to arcsec assuming a distance to the nebula of $d = 3.83$ kpc (Rate & Crowther, 2020).

   (i) **S1 layer:** 146 arcsec $< r <$ 186 arcsec. This layer consists solely of gas with constant density $n = 16$ cm^{-3} and filling factor $\epsilon = 0.03$.

  (ii) **S2 layer:** 186 arcsec $< r <$ 192 arcsec. This intermediate layer comprises gas with constant density $n = 31$ cm^{-3} and a filling factor $\epsilon = 0.08$ together with a population of small dust grains with and MRN power-law distribution with grain sizes between $a_{min} = 0.002$ μm and $a_{max} = 0.01$ μm. The dust-to-gas mass ratio (D/G) in this layer is 6.5×10^{-4}.

 (iii) **S3 layer:** 192 arcsec $< r <$ 228 arcsec. This outer layer is composed of gas with constant density $n = 31$ cm^{-3} and filling factor $\epsilon = 0.08$, and two grain populations: the same small grain population as layer S2 and, in addition, an MRN power-law distribution of large grains with sizes between 0.6 and 0.9 μm. The relative proportion by mass of the large grain population to the small grain population (B/S) is 60. The total dust-to-gas mass ratio (D/G) in this layer is 4.0×10^{-2}.

Full details of this model, labelled L 6-13, are listed in Table 5.2. Taking into account all three layers, the total ionized gas mass of the 3D clump is 0.026 M$_\odot$, with a dust mass of M$_D$ = 0.001 M$_\odot$. Region S3 contains the largest proportion of dust, which reaches 5 per cent of the mass of ionized gas in this layer. Assuming the 3D geometry described above, we calculated the predicted surface brightness profiles, as a function of angular distance from the star, of the different infrared bands obtained from this CLOUDY model, and convolved them with the appropriate instrumental broadening. The results are shown in Fig. 5.1, bottom left-hand panel. The model predicts an angular separation between the Hα peak and the *Herschel* wavelength bands of 6 arcsec, similar to the observations. In Fig. 5.1, the observational surface brightness profiles (top left-hand panel) for the longer wavelength emission are narrower than that of the Hα emission. This suggests that the line-of-sight depth for the dusty material should be smaller than

Table 5.2: Input parameters and final masses for the different layers of the LC and RC models.

Parameter	L 6-13			R 6-13			
	S1	S2	S3	S1	S2	S3	S4
Distance (kpc)		3.8				3.8	
$\log_{10}(L_\star/L_\odot)$		5.91				5.91	
Inner radius["]	146	186	192	144	158	165	181
Outer radius["]	186	192	228	158	165	181	220
n_0 [cm^{-3}]	16	31	31	63	63	63	63
Filling Factor (ϵ)	0.030	0.080	0.080	0.015	0.015	0.015	0.015
a_{small} [μm]	-	0.002-0.010	0.002-0.010	-	0.002-0.010	0.002-0.010	0.002-0.010
a_{big} [μm]	-	-	0.6-0.9	-	-	0.6-0.9	0.6-0.9
B/S	-	-	60	-	-	80	127
D/G	-	8.269×10^{-4}	5.044×10^{-2}	-	4.961×10^{-4}	4.019×10^{-2}	6.334×10^{-2}
Gas mass [M$_\odot$]	0.0027	0.0025	0.0207	0.02458	0.00831	0.03024	0.10266
Dust mass [10^{-5}M$_\odot$]	-	0.2059	104.6	-	0.4123	121.5	650.3

that of the pure gas component: we can imagine a dusty nucleus within a more extended clump of gas, for example.

In Fig. 5.3 (left-hand panel) we plot the dust temperature as a function of the radial distance from the star that results from the 1D spherically symmetric CLOUDY model. The small grains have temperatures around 60 K while the large grains have temperatures around 30 K. The mass-weighted average dust temperature is represented by the heavy line in the figure and we can see that, in the layers with mixed grain populations, it is dominated by the temperature of the large grains, which comprise the bulk of the mass. The average dust temperature is around 30 K, which is considerably lower than the value of $\sim$ 44 K obtained from the MBB fit to the LC photometry (see Section 2.3). This suggests that MBB parameters should be treated with caution when mixed grain populations are expected.

Finally, the synthetic SED obtained from L 6-13 is in Figure 5.4, as well as the synthetic SED obtained from L 6-14 for comparison. L 6-14 have the same physical parameters that L 6-13, however, used the stellar atmosphere model WNL 6-14. In Figure 5.4 we can observe a comparing very well with the observed SED for both models. The χ^2 value for L 6-13 and L 6-14 are 0.119 and 0.157, respectively.

5.3.2 The RC model

The RC model requires 4 layers to adequately explain the observations. As for LC, the regions are defined with regard to the surface brightness profiles shown in Fig. 5.1 (top right-hand panel) and the gas densities are taken from the ATCA results reported
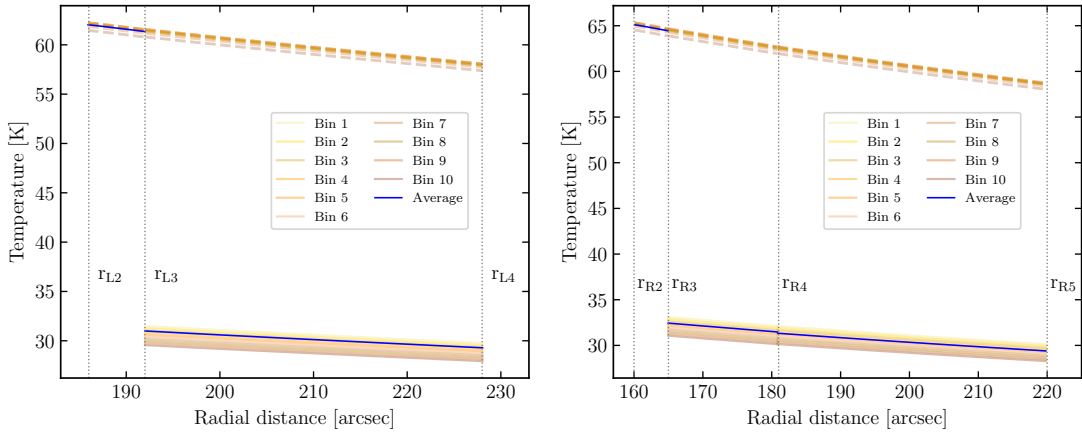
Figure 5.3: Dust temperature as a function of radial distance from the central star for models L 6-13 (left) and R 6-13 (right). Different colours represent different bins in the dust grain size distribution. Solid (dashed) lines represent large (small) grains. Solid blue lines show the mass-weighted average temperature of the grains in each layer.

Figure 5.4: The synthetic SED data points, obtained from our best models of RC (R 6-13 and R 6-14) and LC (L 6-13 and L 6-14), are represented by (filled and hollow) triangles. SED obtained from the IR and ATCA observations of RCW 58: black and red diamonds correspond to the RC and LC regions, respectively (see Section 2.3.2). The residuals are defined as $(F_{obs} - F_{mod})/F_{obs}$.

in Section 2.4. Again, we used the POWR stellar atmosphere model WNL 06-13 in our CLOUDY simulations.

(i) **S1 layer:** 144 arcsec $< r <$ 158 arcsec. This layer contains only gas with density $n = 63$ cm^{-3} and filling factor $\epsilon = 0.015$.

(ii) **S2 layer:** 158 arcsec $< r <$ 165 arcsec. This layer contains gas with constant density $n = 63$ cm^{-3} and filling factor $\epsilon = 0.015$ together with a population of small dust grains with an MRN power-law distribution with grain sizes between $a_{\min} = 0.002$ μm and $a_{\max} = 0.01$ μm. This is the same dust population as layer S2 of the LC model. The dust-to-gas ratio (D/G) in this layer is 3.9×10^{-2}.

(iii) **S3 layer:** 165 arcsec $< r <$ 181 arcsec. This region requires two grain populations: the same small grain population as layer S2 and an MRN power-law distribution of large grains with sizes between 0.6 and 0.9 μm. The gas properties are the same as for layers S1 and S2 and the total dust-to-gas ratio is 3.15×10^{-2}. The relative proportion of the big to the small grains (B/S) is 80.

(iv) **S4 layer:** 181 arcsec $< r <$ 220 arcsec. A final, external layer is required with the same gas properties as the interior layers and the same two grain populations as layer S3. However, in layer S4 the ratio of big to small grains is much higher, equal to 127, and the total dust-to-gas mass ratio is 5.0×10^{-2} in this case.

Table 5.2 lists the details of the R 6-13 model including the D/G and B/S values. Taking into account all four layers, the total ionized gas mass of this model is 0.17 M$_\odot$ and the dust mass is $M_D = 0.016$ M$_\odot$. In region S3 the dust mass is 4 per cent of the gas mass, while in region S4 this rises to 6 per cent. The synthetic surface brightness profiles for model R 6-13 are shown in Fig. 5.1 bottom right-hand panel. There are 3 main peaks in these profiles: one for the optical (gas) emission, one for the 22 μm emission, and one for the longer wavelength emission. The model reproduces the peak separations seen in the observations (see Fig. 5.1) but not the width of the profiles. As for the L 6-13 model, the Hα and narrower dust-emission surface brightness profiles can be explained if the line-of-sight depth of the emitting components is different, with the dusty regions being contained within a larger gas clump.

In Fig. 5.3 (right-hand panel), we plot the dust temperature distribution as a function of radial distance from the star that results from the 1D spherically symmetric CLOUDY model. Similarly to the L 6-13 model, the R 6-13 model discussed here resulted in small grain temperatures around 60 K and large-grain temperatures around 30 K. The mass-weighted average grain temperature is dominated by the large grains and is around 30 K. The grain temperatures are a little higher than in the L 6-13 model because all the components are slightly closer to the star.
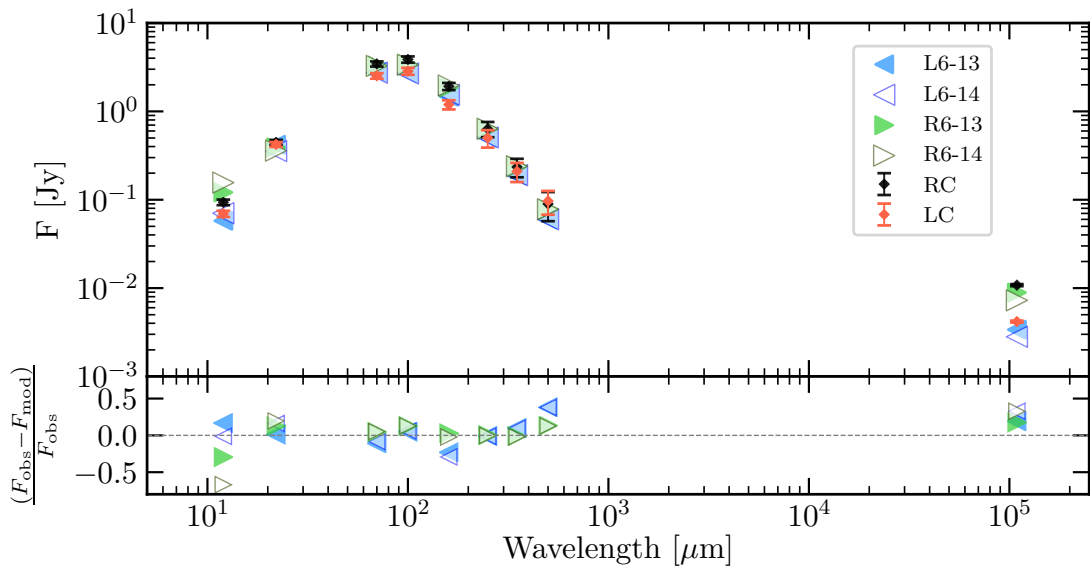
Finally, the synthetic SED obtained from R 6-13 is in Figure 5.4, as well as the synthetic SED obtained from R 6-14 for comparison. R 6-14 have the same physical parameters that R 6-13, however, used the stellar atmosphere model WNL 6-14. In Figure 5.4 we can observe a comparison very well with the observed SED for both models. The χ^2 value for R 6-13 and R 6-14 are 0.089 and 0.136, respectively.

5.3.3 Optical emission lines

We used PYCLOUDY library of tools to make synthetic observations of optical emission lines from an aperture corresponding to Esteban et al. (2016) observations. The observed spectrum is extracted from a small (1×8 arcsec^2) region of the RC clump. In Table 5.3, we list the emission-line fluxes from the spectroscopic observations of Esteban et al. (2016) together with the synthetic observations obtained from our CLOUDY models using the two different POWR stellar atmosphere models, WNL 06-14 and WNL 06-13 (Hamann et al., 2006). RCW 58 is a low-ionization nebula and the optical spectrum shows several He I recombination lines.

Model R 6-14 does a reasonable job at reproducing the general emission-line trends in the observed spectrum. The electron density, derived from the [O II] $\lambda\lambda\, 3726/3729$ Å and [S II] $\lambda\lambda\, 6716, 6731$ Å doublets using PYNEB (Luridiana, Morisset & Shaw, 2015) returns similar results to the value derived from the observations. However, the electron temperature, derived from the [N II] emission lines, is considerably lower. Moreover, the intensities of all the He I recombination lines are lower than those observed, suggesting that He$^+$/He is lower in the model. This parameter depends on the ionizing source properties and is lower for softer ionizing sources (Delgado-Inglada, Morisset & Stasińska, 2014). Thus, we also ran CLOUDY simulations using the stellar atmosphere model WNL 06-13, which has a higher rate of Helium-ionizing photons and is a harder ionizing radiation source (see Table 3.1).

The results of changing the stellar atmosphere model to WNL 6-13 are also presented in Table 5.3, labelled as R 6-13. This model does an even better job of reproducing the general trends of the spectral lines and He recombination line intensities are very similar to the observations. The low-ionization lines of [O II] and [S II] are also a close match. The electron temperature and density derived from the model emission lines are within the errors of those derived by the same methods using the observed line intensities.

It is interesting to note that none of our CLOUDY photoionization models reproduces the [N II], [O III] 5007 Å or [S III] emission-line intensities seen in the observations. We varied the abundance of N within the range of values suggested in Table 5.1 but this did not make a significant difference to the line intensities relative to Hβ. A slightly hotter star, as suggested by the temperature diagnostic, could explain the discrepancies between the observed [O III] and [S III] emission line intensities and the model results. With regard to the [N II] results, we note that analysis of the full CLOUDY model shows

Table 5.3: Emission lines considered in our models. Observational data were taken from Esteban et al. (2016) and are relative to Hβ = 100.

Line	Observations	R 6-13	R 6-14
Hβ	100.0	100.0	100.0
Hα	310 ± 11	299.75	302.25
[O II] 3726	24.2 ± 1.2	23.83	12.71
[O II] 3728	33.5 ± 1.4	32.80	17.61
H I 3734	2.19 ± 0.46	2.36	2.35
H I 3750	4.14 ± 0.98	3.00	2.99
H I 3770	3.88 ± 0.62	3.89	3.88
H I 3797	3.59 ± 0.35	5.19	5.17
He I 3819	1.75 ± 0.44	2.23	0.65
H I 3835	6.70 ± 0.55	7.14	7.12
He I 3888	31.3 ± 1.3	24.57	7.36
He I 3964	3.2 ± 0.51	1.07	0.97
H I 3970	15.77 ± 0.67	15.52	15.46
He I 4026	4.80 ± 0.74	4.03	1.02
H I 4101	30.75 ± 0.99	25.32	25.22
H I 4340	48.9 ± 1.2	46.07	45.94
He I 4387	1.0 ± 0.25	1.07	0.27
He I 4471	8.84 ± 0.36	8.42	2.15
He I 4921	2.21 ± 0.34	2.31	0.60
[Fe III] 4658	0.87 ± 0.22	1.02	0.65
[O III] 5007	14.14 ± 0.54	2.79	0.00
He I 5015	4.46 ± 0.16	3.30	1.20
[N II] 5755	1.11 ± 0.12	0.68	0.49
He I 5875	25.45 ± 0.90	22.99	5.87
[N II] 6548	101.3 ± 3.6	72.71	90.42
[N II] 6584	312 ± 11	214.33	266.55
He I 6678	8.15 ± 0.37	6.47	1.68
[S II] 6716	10.58 ± 0.47	11.02	25.40
[S II] 6731	8.01 ± 0.36	8.25	18.88
He I 7065	3.99 ± 0.34	5.03	1.25
[Ar III] 7135	4.66 ± 0.47	5.75	0.72
[S III] 9068	19.2 ± 1.4	12.16	1.97
[S III] 9530	59.9 ± 4.1	30.54	4.95
F(Hβ) ×10^{-14}	1.45±0.03	0.068	0.071
T_e[N II]5755/6584	6370±220	6190	5450
n_e[O II]3726/3729	80	87	80
n_e[S II]6716/6731	90	80	72

that [N II]/Hα increases with radius from a minimum of 0.7 to a maximum at the outer radius of 1.7. For the small aperture on RC of the Esteban et al. (2016) observations, the [N II]/Hα ratio is 1, while our R 6-13 model finds 0.7 at this position. We remark that Smith et al. (1988) found that the [N II]/Hα ratio varied between 0.9 and 2 along a slit with position angle 167° crossing the shell roughly in the location of the region LC. We tentatively attribute the [N II] discrepancy to the line-of-sight depth taken through the model, or the positioning and spatial resolution of the model aperture. Returning to the higher ionization lines, another possibility is that there is a contribution from tenuous material behind the outer shock, which is propagating into a low-density surrounding medium (see the analysis presented by Gruendl et al., 2000). In optical images, the ejecta clumps are enveloped in a faint [O III] shell and some of this shocked gas emission will inevitably be included along the line-of-sight in the aperture.

We note that the Hβ flux obtained by Esteban et al. (2016) is a factor $\sim$ 20 higher than that calculated by our models. We attribute this to small-scale density variations within RC, which are not accounted for in our model but which are emphasized in the small bright region covered by the aperture in the observations. Including density profiles in our model would add complexity by increasing the number of free parameters. Because of this, we decided to give priority to the radio photometry obtained from ATCA observations, which is more representative of the average density properties of the clumps.

5.3.4 Ionized gas mass estimation

Assuming that RCW 58 is optically thin and that its free-free emission is thermal, we can obtain a global estimation of the ionized mass of the nebula using the procedure outlined by Smith & Batchelor (1970). The mass of the nebula is given by

$$M = (1 + 3a)M_{\mathrm{H}}n_{\mathrm{e}}V, \tag{5.1}$$

where M_{H} is the mass of the hydrogen atom and V is the effective radiating volume. Smith & Batchelor (1970) considered that the nebula has uniform density and that the helium is all singly ionized, and found an expression for V from the integrated emissivity at frequency v_0,

$$V = 50\, T_{\mathrm{e}}^{0.35}\, v_0^{0.1}\, \frac{d^2 S}{n_{\mathrm{e}}}. \tag{5.2}$$

where S is the flux of RCW 58 at v_0. The mass can then be expressed as

$$\frac{M}{\mathrm{M}_\odot} = 1.24 \frac{(1 + 3a)}{n_{\mathrm{e}}} \left(\frac{S}{[\mathrm{Jy}]} \right) \left(\frac{d}{[\mathrm{Kpc}]} \right)^2 \left(\frac{v_0}{[\mathrm{Hz}]} \right)^{0.1} \left(\frac{T_{\mathrm{e}}}{\mathrm{K}} \right)^{0.35}, \tag{5.3}$$

where a is the fraction of helium in the nebula. From optical data and our photoionization

models we have T_e = 6190 K, n_e[O II] = 87 cm^{-3} and an average value of the helium fraction is a = 0.155. Finally, we measured a flux of 4.383×10^{-2} Jy of RCW 58 from the ATCA observations and thus we estimate an ionized gas mass of 2.5 M$_\odot$.

5.4 Discussion

Our best PYCLOUDY model successfully reproduces the IR photometry corresponding to the thermal emission from the dust in the nebula and approximates the main characteristics of the photoionized gas in RCW 58. In this section, we discuss the limits of our models in accounting for all of the observed spectral features and also place our models in the context of the evolution of the central star (WR 40).

5.4.1 Dust characteristics and spatial distribution

Our best CLOUDY models require the presence of two populations of grain sizes for both RC and LC. A population of small grains with sizes between 0.002 and 0.01 μm is needed to fit the short wavelength part of the SED. The small grains and gas absorb most of the UV radiation from the star but the large grains dominate the dust mass.

The two grain populations are not uniformly mixed in the gas. For both RC and LC the photoionization models require an inner layer devoid of dust (S1 in Fig. 5.2). Layer S2 contains only the population of small grains: for LC the dust mass in this layer is 0.08 per cent (see Table 5.2). Layers S3 and S4 (if present) contain both small and large grains, with total dust mass rising to between 4 and 6 per cent of the gas mass. The mass of the large grains is roughly two orders of magnitude greater than that of the small grains in these layers and is considerably higher in RC than in LC. We remark that the gas density in RC is twice as large as that of LC.

Grain sizes, shapes, and chemical composition

In our models, we have assumed that the grains are composed purely of silicates. This is because the envelopes of massive stars will be nitrogen rich and carbon poor as a result of the CNO cycle in the hydrogen burning core and the mixing that occurs in convective zones after the main sequence. Oxygen is therefore expected to dominate the dust chemistry. The total mass of silicate dust that can be produced is limited by the availability of the least abundant element that makes up the dust formula: in this case Si. Our models require that 5 per cent of the total mass of the S3 and S4 layer material is in the form of silicate dust. Since each olivine molecule in the dust grains has a mean molecular weight of $\mu_{mol} \sim$ 172, then the dust molecule abundance relative to hydrogen can be found from the relation

$$\frac{n(\text{dust})}{n(\text{H})} = \frac{D}{G}\frac{1}{X\mu_{\text{mol}}}, \tag{5.4}$$

where D/G is the dust-to-gas mass ratio reported in Table 5.2 and X is the hydrogen mass fraction of the gas. For the gas abundances used in this work (see Table 5.1), the hydrogen mass fraction is $X \sim 0.6$. The grain molecule abundance is therefore $n(\text{dust})/n(\text{H}) \sim 5 \times 10^{-4}$ and, since every grain molecule contains a silicon atom, we compare this with the Solar silicon abundance $n(\text{Si})_\odot/n(\text{H})_\odot \sim 4 \times 10^{-5}$ (Grevesse et al., 2010). Thus, the implication is that there are at least 10 times more silicon atoms bound up in grains in RCW 58 than should be available, since the assumption is that no additional silicon has been formed by nucleosynthesis in WR 40.

A possible explanation for this is because we use spherical grains in our models. Grains with larger far-IR absorption cross-sections than spherical grains can require less mass to reproduce the observed IR SED. Spheroidal grains have far-IR absorption cross-sections larger by a factor of 1.5 to 3 than spherical grains with the same volume (Siebenmorgen, Voshchinnikov & Bagnulo, 2014). Also, the emission of spheroidal grains would be shifted to longer wavelengths (Gómez-Llanos et al., 2018).

Another possibility could be so-called *fluffy* grains (porous aggregates of grains), which have a greater absorption cross-section than compact grains with the same mass. For grains larger than $a > 0.01\mu$m, porosity develops by grain growth due to coagulation. To explore this possibility, we computed a CLOUDY model using the same nebular parameters as model L 6-13 but changing to fluffy grains. We used grains comprised of 50 per cent vacuum and the rest being silicate material, i.e. porosity of 0.5. This model, denoted LC (fluffy), had the same two populations of grains sizes as our standard model L 6-13, that is, a population of small grains with sizes between 0.002 and 0.010 μm, and a population of big grains with sizes between 0.5 and 0.9 μm. Model LC (fluffy) successfully reproduced the observed IR SED with the same spatial distribution of dust as that of L 6-13. The model results in a total mass of dust of $M_{\text{LC(fluffy)}} = 3.8 \times 10^{-4}$ M$_\odot$, of which 90 per cent corresponds to the largest size grains. This is in contrast to the 10.5×10^{-4} M$_\odot$ of dust required by the compact grain model. That is, fluffy grains can reduce the total amount of dust material required by a factor of 2 or more, depending on the porosity.

Although the results with fluffy grains seem promising, coagulation of small grains into porous large structures will only occur in cold, dense regions ($T_{\text{gas}} < 100$ K and $n > 10^3$ cm^{-3}), where the grain relative velocities are small enough to allow the grains to stick to each other through low-velocity grain-grain collisions (Dominik & Tielens, 1997; Hirashita & Yan, 2009). High velocity collisions will cause the grains to shatter.

Recent studies have demonstrated that the competing effects of coagulation and shattering create and maintain the porosity of the grains, and a maximum porosity of 0.7 to 0.9 is achieved for grain size around 0.1 μm, with larger grains being less porous

(see Hirashita et al., 2021). Our models imply that the dust mass is dominated by grain sizes much larger than 0.1 μm and although the porosity of such grains is not optimum, it can still result in a factor 2 or 3 reduction in the total mass of grains required to explain the observations.

We have not explored the effect of including other grain species, such as iron or amorphous carbon grains, on our results. This is because our underlying assumption is that the RCW 58 nebula material was ejected from the envelope of the progenitor star, which we expect to be oxygen rich and carbon poor. However, radiative transfer modelling of the 2.4 to 670 μm spectral energy distribution of the dusty Homunculus Nebula around the Luminous Blue Variable star η Carina suggests the presence of iron, pyroxene, and other metal-rich silicates, corundum, and magnesium-iron sulphide (Morris et al., 2017). The total dust mass our models infer for RCW 58 would be easier to explain if it were not so dependent on the abundance of Si.

Multilayer distribution of dust grains

Our preferred CLOUDY models require the grains to be stratified in different layers within the clumps. The part of the clump closest to the star is devoid of dust. There is a population of small grains, with sizes between 0.002 and 0.01 μm, which is found throughout the remainder of the clump, and a population of much larger grains, with sizes between 0.6 and 0.9 μm, which is found only in the part of the clump furthest from the star. Where the large grains exist, they dominate the dust mass, and in RC their proportion increases with distance from the star. We will discuss the following interpretations for the stratified dust distributions:

(i) The large grains and small grains did not all form in the same location and this different spatial origin is preserved in the current clumps.

(ii) The small grains result from the destruction of the large grains as a result of clump disruption by the stellar wind shock.

(iii) The small grains and the large grains were well mixed until dynamical segregation occurred, due to the interaction of the clump with stellar wind shock or due to radiation pressure on the large grains.

The large grain sizes inferred by our models require extreme environments and special physical processes such as coagulation through grain-grain collisions. Large grain sizes are also derived for other objects such as nova ejecta and Type II SN. Recent high-sensitivity ALMA observations with an angular resolution of 0.1 arcsec of the red supergiant VY CMa reveal the presence of massive dusty clumps on spatial scales 70-700 AU from the star (Kamiński, 2019). Radiative transfer modelling, including grains up to 1 μm, suggests an atypically low gas content for the clumps in order to reconcile

the total envelope mass of the star. It was not possible to determine whether there was a change in dust properties with distance from the star from these observations.

On the other hand, numerical studies of dust formation in the ejecta of low-mass systems that underwent a common envelope event show that dust is initially formed in the outer regions of the gas distribution, but it is not the largest grain size achieved in the calculations (Iaconi et al., 2020). The largest grain sizes (0.1–1 μm) are formed at intermediate times in the simulations and are not located at the outer edge of the gas distribution. If a similar dust formation history occurred in RCW 58, extra processes have created the observed spatial distribution of grain sizes.

The clumpy shell seen in Hα and 2.75 GHz images of RCW 58 (see Figs. 2.2 and 2.6) is most likely the result of the interaction of the stellar wind shock with a layer of clouds. There is rich literature on the interaction between a single cloud with a shock or a wind (see e.g. Pittard & Parkin, 2016; Goldsmith & Pittard, 2018) but studies of multicloud systems are less common (Alūzas et al., 2012; Banda-Barragán et al., 2020, 2021). Important features of the multicloud scenario are the thickness of the cloud layer and the spatial separation between the mass sources (i.e. the porosity). Not only do the clouds interact with the main shock but there are subsequent interactions within the shocked layer. Although the parameters (intercloud density and shock velocity) are not tuned for nebulae around massive stars, the general scenario portrayed in simulations such as those of Banda-Barragán et al. (2021) can be appreciated.

Initially, the impact of the main shock on the cloud layer triggers reflected and refracted shocks. After a short-lived transient period where the forward (refracted) shock splits into multiple shocks with different speeds as it encounters clouds of different densities, it then transitions to a steady transmitted shock that traverses the cloud layer, heating and compressing it. Individual cloud cores interact with the transmitted shock, expand laterally and are accelerated downstream. Kelvin-Helmholtz instabilities at the cloud-intercloud interfaces strip material from the clouds and entrain it into the flow. When the forward shock exits the cloud layer, it re-accelerates, and low-density entrained material moving with the post-shock flow also expands in the same-wise direction. Individual clouds are stretched and produce filamentary tails. Banda-Barragán et al. (2021) show that, in radiative models, strong cooling can promote the clumping and fragmentation of dense gas. In RCW 58 there is the added process of photoionization, which will prevent the flow from cooling below 6500 K. Turbulence and mixing occur in the low-density, heated flow behind the accelerating forward shock.

In the context of RCW 58, we see that different parts of the nebula are at different stages of this process. Towards the east, the forward shock has clearly exited the cloud layer and has left behind elongated filaments. In the region of RC, and also towards the north-east, the [O III] emission is not well-separated from the Hα shell, suggesting that the forward shock is only just exiting the cloud layer (see Gruendl et al., 2000). Large linewidths were found in the optical spectra by Smith et al. (1988)

in the vicinity of LC, suggestive of turbulent gas motions. The radial velocity with respect to the local standard of rest found in these long-slit spectra is about 90 km s^{-1}. In addition, blueshifted absorption components with v_{LSR} between -150 and -100 km s^{-1} have been detected in UV and optical spectra of the central star, WR 40 (Smith et al., 1984). In the radiative simulations of Banda-Barragán et al. (2021), the forward shock re-accelerates to at most 0.4 times the initial shock velocity when it exits the cloudy layer i.e. $v_{as} \sim 0.4v_b$, and the post-shock flow velocity is $v_{psh} = 0.75v_{as}$ for a fast-shock. If we take the range of observed velocities as the post-shock flow velocities, then the initial shock velocity would be $300 < v_b < 500$ km s^{-1}.

What consequences does this scenario have for the dust in RCW 58? While traversing the cloud layer, the forward shock has a lower velocity than the original shock wave, $v_{fs} = Kv_b/\chi^{1/2}$, where χ is the density contrast between the cloud and the intercloud gas, and $K \sim 2$ (Banda-Barragán et al., 2020). The transmitted shock velocity within the cloud layer, assuming a density contrast of $\chi = 10^2(10^3)$, will then be $v_{fs} \sim 60(20)$ km s^{-1} for the lower value of v_b or $v_{fs} \sim 100(30)$ km s^{-1} for the higher value.

Grains can be destroyed by shock waves through thermal and non-thermal sputtering, and through grain shattering (see e.g. Jones, Tielens & Hollenbach, 1996). Sputtering arises from gas-grain impacts and returns grain material to the gas phase. Thermal sputtering is only important for fast shocks ($v_s > 150$ km s^{-1}), and non-thermal sputtering is the main dust-destruction process for intermediate shock velocities (50 km s^{-1} < v_s < 150 km s^{-1}). Grain shattering dominates below $v_s < 50$ km s^{-1}. For cloud-intercloud density contrasts $\chi = 10^2$, the range of transmitted shock velocities we derived for the cloudy layer falls within the range for non-thermal sputtering to be important. However, the time-scale for dust destruction by sputtering for gas densities $n \sim 100$ cm^{-3} is of the order of 10^6 yr, far larger than the age of the nebula. Thus, sputtering is not expected to be important in RCW 58. For higher density contrasts, $\chi = 10^3$, the transmitted shock velocities are outside the sputtering range. However, we can expect shattering to be an important grain destruction mechanism. Shattering conserves the total grain mass but alters the grain size distribution. Thus, shattering could produce the population of small grains required by our CLOUDY models. However, the layer S2, which contains only small grains, should have a similar dust-to-gas mass ratio as the other layers, S3 and S4, if shattering is responsible.

We now consider segregation of the grains into the populations of large grains and small grains with a different spatial distribution that our models require. We assume that the two populations of grains are initially well-coupled to the gas in the clumps. When the shock encounters a clump, the gas is compressed but the grains, due to their large inertia, decouple from the gas. The acceleration of the grains is opposed mainly by collisional drag forces. Collisional drag is due to direct collisions of grains with atoms and ions, it is proportional to the grain cross-section and inversely proportional

to the grain mass. Large and high-density grains are therefore least affected by drag and remain decoupled from the gas.

Finally, we remark that gas-grain drift due to radiation pressure on dust grains could have played a role at early times, when the clumpy layer was much closer to the star. In photoionized regions, such as RCW 58, Coulomb forces between gas ions (mainly protons) and charged dust grains lead to increased plasma drag forces, which couple the dust to the gas (Draine, 2011). However, the dust is subject to a much larger radiation force than the gas, which leads to a drift between the dust and gas components and even a total decoupling sufficiently close to the star. Large and small grains decouple and recouple at slightly different distances from the star (Henney & Arthur, 2019), so this differential could have imprinted itself on the spatial distribution of the grain sizes soon after the clumps were ejected from the stellar envelope and the star became a source of ionizing photons. Note that in Jiménez-Hernández, Arthur, & Toalá (2020) our model for M 1-67 requires two layers: one of pure gas and one in which populations of small and large grains were mixed.

5.4.2 Tracing the origins of RCW 58 and WR 40

Given the strong IR emission from the background of RCW 58 we were not able to produce a complete model for the nebula. However, we can estimate the total mass (gas+dust) by extrapolating from our results tailored to LC and RC and, consequently, estimate the initial mass of the progenitor of WR 40.

From Table 5.2, the total masses estimated for the LC and RC are 0.027 and 0.173 $M_\odot$, respectively. Taking the average of these values as typical for the 23 clumps detected in the radio image of RCW 58 we estimated $M_{TOT} \approx 2.3 \pm 1.7$ $M_\odot$, which is of the same order as the mass estimated from the ATCA observations (2.5 $M_\odot$) and consistent with previous determinations of 3 $M_\odot$ (Smith & Batchelor, 1970; Chu, 1982). These results confirm RCW 58 as the least massive WR nebula (see Chapter 4 and Rubio et al., 2020, and references therein).

The current mass of WR 40 has been estimated to be in the 26–28 $M_\odot$ range by Hamann et al. (2019). Adding to this the mass of RCW 58 and considering that massive stars lose up to $\sim$ 10 $M_\odot$ during the main sequence phase (for stars with ZAMS masses above 30 $M_\odot$; see Ekström et al., 2012; Georgy et al., 2012), we can estimate the mass of the progenitor of RCW 58. These results seem to suggest that WR 40 evolved from a massive star with an initial mass around $M_i \approx 40^{+2}_{-3}$ $M_\odot$.

Such small estimates of the total mass of RCW 58 and the initial mass of WR 40 argue against an LBV scenario, but the need for dust with grain sizes as large as 0.9 μm advocates for an eruptive formation scenario where $\dot{M} > 10^{-3}$ $M_\odot$ yr^{-1} (see Section 1.3.1). An alternative formation mechanism for RCW 58 is that of the common envelope (CE) scenario. The idea, initially proposed by Paczyński (1976), is that a companion in a close binary system accretes the H-rich envelope from a massive component. This causes

the reduction of the period of the binary in a spiral-in process releasing orbital energy that then ejects the massive envelope of the primary, simultaneously creating a WR star and its associated nebula. A more extreme version of this scenario is explosive CE ejection (ECEE), proposed by Podsiadlowski et al. (2010). In this mechanism, hydrogen-rich material from the secondary component is injected into the helium-burning shell of the primary component of a binary system. The energy released from explosive nucleosynthesis expels the H-rich envelope. This scenario could naturally explain the extra Si needed to fit the IR SED of RCW 58 but would result in ejecta velocities far higher than those observed as well as requiring the primary to already be in a helium shell-burning stage of evolution (see Chapter 4). We favour the orbital energy route for the expulsion of the H-rich envelope but are left with the conundrum of the large quantity of silicate grains implied by our results.

5.4.3 Comparison with M 1-67

RCW 58 and M 1-67 share similar characteristics, besides harbouring WN8h stars. Their optical images are dominated by Hα clumps and their thermal IR emission is produced by dust associated with these clumps. Neither nebula has undergone a strong interaction with the surrounding ISM and their optical spectra are characterized by low-ionization emission lines. However, RCW 58 shows clear signs that the fast stellar wind from the central star has interacted with the circumstellar clumps, giving rise to the [O III] skin and leaving a turbulent flow in its wake. M 1-67 appears not to have been overrun by a fast stellar wind, indeed, a morphokinematic model of M 1-67 recently proposed by Zavala et al. (2022) requires three concentric structures each of them composed by a torus and a bipolar structure.

In subsection 4.4.3 we estimated the kinetic energy associated with the expanding clumps in M 1-67 using the nebular mass calculated from our CLOUDY models (9.2 M$_\odot$) and the measured expansion velocity of 46 km s^{-1}, obtaining $E_K \approx 1.9 \times 10^{47}$ erg. For RCW 58, the expansion velocity is less well-defined, but adopting a value in the range 30–87 km s^{-1} (see Chu, 1982; Smith et al., 1988) together with a total mass of 2.5 M$_\odot$ (see section 5.3.4), we estimate the kinetic energy for RCW 58 to be $E_K \approx [0.3-1.9] \times 10^{47}$ erg. The similarity of these values suggests a similar origin for the ejected mass in each nebula. Moreover, the toroidal nature deduced for M 1-67 appears to be replicated in RCW 58, since our models require a ring of material seen approximately pole-on, rather than a complete shell (see also Chu, 1982). This supports the suggestion that both M 1-67 and RCW 58 formed through a CE channel. If confirmed, these stars should be placed under scrutiny because they could evolve to become stripped-envelope stars, which could eventually be candidates for progenitors of gravitational wave sources (see Laplace et al., 2020).

6   Stellar evolution models

In this chapter, we study the dynamical mass loss in a common-envelope object by examining the dynamical properties of the object during the slow spiral-in phase using a parameterised 1D model of orbital dissipative heating. We find that the envelope becomes unstable to high-amplitude dynamical pulsations that can lead to repeated mass-ejection events capable of removing part of the hydrogen envelope and terminating the common-envelope phase. We estimate the conditions under which this occurs and discuss how this mechanism may resolve the origin of M 1-67 and RCW 58, two Wolf-Rayet nebulae around WN8h stars.

6.1   Common envelope in massive stars

A general outline about the formation and evolution of a CE in a binary scenario was described by Paczyński (1976). In a close binary, as the primary star evolves it expands; if the material from its extended surface fills the Roche lobe and passes beyond the outer Lagrangian point, and CE is originated (see Figure 6.1). Inside the common envelope the secondary star and the dense nucleus of the primary star spiral towards each other, triggering different physical processes that release energy (e.g. frictional dissipation of the binary's orbital energy). The released energy generates an expansion of the envelope. In some cases, this energy can generate the loss of the envelope through one or several ejections. The loss of the envelope leads to the loss of angular momentum, causing the orbital period to decrease by a few orders of magnitude and it can lead to a tighter binary.

There is a wide variety of binary systems that can form a CE and not all cases follow the general scheme proposed by Paczyński (1976); for example, a merger can occur during the evolution of the CE. Thus, the CE process has been suggested as the main formation channel for many classes of late-stage star systems; for example, X-ray binaries, SN progenitors, stellar-mass gravitational-waves sources, Thorne-Zytkow objects and potential progenitors of both short- and long- duration gamma-ray bursts (see Ivanova et al., 2013, and references there in). It is important to carry out studies to understand the conditions and the evolution process of a CE, since at least 30% of binaries are believed to have passed through this stage at some time (Han, Podsiadlowski, & Eggleton, 1995). Also, there are cases where the conditions of the binary system allow this process to occur more than once, for example, type Ia supernovae, which

[19] https://commons.wikimedia.org/wiki/File:Common_envelope_evolution.svg
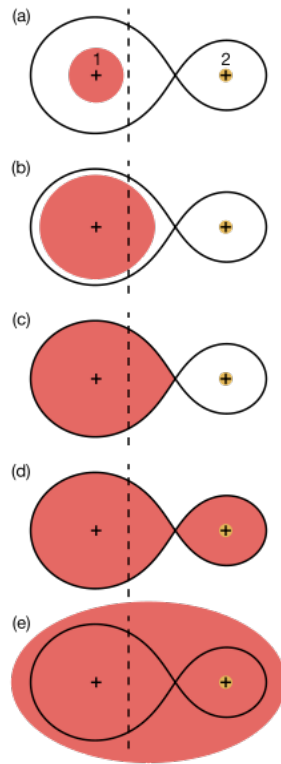
Figure 6.1: CE formation. The solid and dashed black lines represent the Roche lobe and rotation axis of the binary. The stellar material of the primary and secondary star is indicated by red and orange areas, respectively. (a) Primary and secondary stars centred at points 1 and 2, respectively. (b) Primary star expands, (c) until it fills its Roche lobe and transfers mass to secondary. (d) The primary transfers too much material and cannot be accreted by the secondary. (e) Secondary Roche lobe is full and the stars enter into a common envelope. Image author Philip D.Hall[19] adapted from Izzard et al. (2012)

may experience several mass transfer episodes between the companion and the white dwarf until the latter reaches its critical mass and explodes.

The CE process has proven remarkably difficult to constrain observationally and theoretically. Observationally it is difficult to identify CE-type objects due to their short lifetime. There are currently no clearly identified examples of ongoing CE events that have been observed, but the results of different works have made it possible to suggest some transients as candidates.

To model CE evolution it is necessary to be able to resolve timescales and spatial scales in order to take into account the different factors that contribute to the physics of the system. However, the CE process has a broad range of timescales. For example, the orbital period changes dramatically from start to end of the process (hours to days). When the primary and secondary are inside the CE the dynamical timescales of the interaction between both objects and the surrounding material can be seconds if there is a compact object. Also, the thermal timescales of the envelope are of the order of ~1000 years. On another hand, the spatial scales range from the size of the secondary to the radius of the shared envelope, that is, from 10 km (neutron star size) to order 10^3 R$_\odot$.

Three phases have been identified in numerical simulations of the evolution of CE (see Podsiadlowski et al., 2001; Ivanova, 2002, and references therein):

- **Loss of corotation**. In this phase, the spiral-in inside the common envelope starts. The binary loses its stability because the secondary, which initially has a circular orbit in corotation with the primary, starts to break down this corotation, and the orbit will cease to be circular.

- **Fast plunge-in**. The secondary enters into a dynamical plunge-in into the CE. The high rate of energy dissipation drives the expansion of the envelope and the binary orbit contracts on a dynamical timescale. The binary components approach each other in a spiral path

- **Self-regulating spiral-in**. In this phase (also referred as slow spiral-in) the spiral-in will slow down, and the frictional energy released increases the expansion of the envelope and reduces the rate of orbit contraction.

6.2 Simulation model

The best way to investigate the physics involved in processes where there are dynamical interactions is to model the systems in 3D simulations and the evolution of CE is no exception. However, due to the large number of physical parameters involved (including time scales) in each phase of the evolution of CE-type objects, these simulations have a long computation time (e.g. Iaconi et al., 2017). Ivanova & Nandez (2016) compared a 3D

and a 1D simulation of the same system evolving as CE in the "spiral-in" phase. They conclude that the 1D simulation overestimates entropy resulting in different outcomes in the 1D and 3D simulations. Nevertheless, we can use 1D models to examine some of the physics relevant to the CE process and take advantage of their computationally cheaper nature to explore parameter space (Ivanova & Nandez, 2016).

We employ the stellar evolution code Modules for Experiments in Stellar Astrophysics (MESA) created by the MESA collaboration (Paxton et al., 2011). In this section we summarize the physics required to model CE dynamical evolution used in this thesis. We use as information source Paxton et al. (2011, 2013, 2015, 2018); Clayton et al. (2017) and the online module documentation of the MESA version r15140[20].

6.2.1 MESA execution

MESA is a suite of open source modules that develop 1D stellar evolution models. One of them is MESA star; this module solves the fully coupled structure and composition equations simultaneously based on an implementation of a Henyey style code (Henyey, Forbes & Gould, 1964). Basically, Henyey's method discretizes and associates the stellar physical parameters in concentric layers that allow the construction of a 1D evolutionary model. MESA star uses adaptive mesh refinement, sophisticated timestep controls, analytic Jacobians, coupled solution of the structure and composition equations, and supports shared memory parallelism based on OpenMP. In order to solve highly nonlinear systems of differential-algebraic equations, this module is integrated with a multidimensional Newton-Raphson solver. In addition, MESA star calls the modules that provide equation of state, opacity, nuclear reaction rates, element diffusion data, and atmosphere boundary conditions. Each module is constructed as a separate Fortran 95 routine with its own interface to simplify independent development Paxton et al. (2011).

Starting models

Under the Henyey method scheme MESA star builds 1D, spherically symmetric models by dividing the structure into cells, and simultaneously solves the full set of coupled equations for all cells from the surface to the center of the star. The solution of a MESA simulation is a sequence of individual, static stellar models separated by timesteps. Each individual model is discretized in a radial spatial dimension. The values of timesteps and the radial distribution are parameterised by mass coordinate.

There are two ways to start a new evolutionary sequence with MESA star. The first one is to use a saved model from previous run, that could be take of default files of MESA or previously saved by the user. The second way to start a new evolution is to create a

---

20 https://docs.mesastar.org/en/r15140/modules.html

Pre-main sequence (PMS) model by specifying the mass, M, a uniform composition, a luminosity, and a central temperature.

MESA star first reads the input files and initializes the physics modules to create a nuclear reaction network and access the EOS and opacity data. The specified starting model or PMS model is then loaded into memory, and the evolution loop is entered. The procedure for one timestep in each simulation can be summarized as follows (see Figure 6.2):

1. It prepares to take a new timestep. Here, the model is re-meshed if necessary; for example, when the star's surface expands (Flowchart label: Prepare for a step).

2. It adjust the model to reflect changes in its initial parameters: mass loss by winds or mass gain from accretion, adjusts abundances for element diffusion, determines the convective diffusion coefficients. It also solves for the new structure and composition using the Newton-Raphson solver (Flowchart label: Take step - Check model).

3. The timestep ends (Flowchart label: Finish step).

4. Output files are generated (Flowchart label: Write data). Not all output data is saved to files, only those that have been specified in the input files.

Figure 6.2 shows a flowchart presenting an overview of a MESA run. At each timestep, MESA star converges on a final solution. But if the corrections and residuals of the solution cannot achieve convergence with the current timestep, then MESA will first try again with a reduced timestep in order to reduce the nonlinearity (see first decision in Figure 6.2). If the retry fails, MESA returns to the previous model and decreases the timestep to try again. This cyclical process will continue until either the model converges or the timestep reaches some pre-defined minimum (it can be specified by the user), and then the evolutionary sequence is terminated.

6.2.2 Stellar structure

MESA code has a wide variety of modules that provide the physical properties of stellar matter for a detailed model of stellar evolution. In this subsection we briefly describe the physics considered for this work, for more detailed information see Paxton et al. (2011, 2013, 2015, 2018) and references therein.

Microphysics

The MESA microphysics modules provide information about the equation of state (EOS), opacities, and the nuclear reaction networks. The EOS module works with density, ρ, and temperature, T, as independent variables. By default MESA build up $\rho - T$ tables
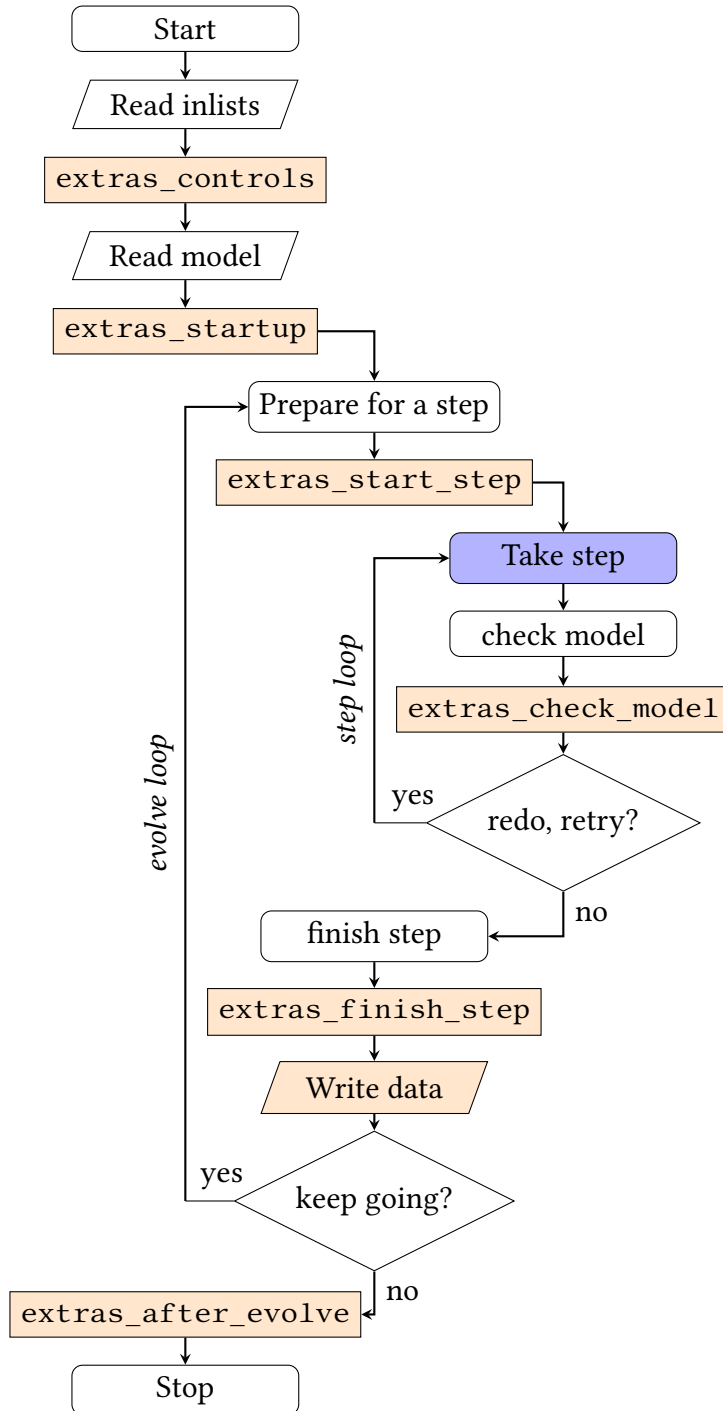
Figure 6.2: Flowchart summarizing MESA execution structure. The orange blocks on flowchart indicated the possibility to insert your own code to be executed by MESA at these times. Source: https://jschwab.github.io/mesa-2021/.

based on OPAL EOS tables (Rogers & Nayfonov, 2002) and they can be extended by other default tables in order to increase $\rho - T$ coverage. MESA opacity tables are built up by combining radiative opacities (divide into high- and low-temperature domain) with electron conduction opacities from the extended tables of Cassisi et al. (2007). The user can extend the EOS and opacity tables based on the default tables, or implement tables from any source as long as the tables conform to MESA's standard format. The reaction networks module contains set of isotopes and a set of reactions. Although the module with networks of nuclear reactions in MESA has been constantly updated, the user can implement a new network. By default MESA includes a basic network of eight isotopes: ^{1}H, ^{3}He, ^{4}He, ^{12}C, ^{14}N, ^{16}O, ^{20}Ne, and ^{24}Mg, and contains more than 300 rates for elements up to nickel.

Macrophysics

With regard to the physics of mixing, MESA star by default implements the mixing length theory (MLT) of convection from Cox & Giuli (1968). In the MLT is necessary to provide the ratio of the characteristic mixing length (l_{mix}) of convective motions to the pressure scale height (H_p) of the star:

$$\alpha_{\mathrm{MLT}} = \frac{l_{\mathrm{mix}}}{H_p}, \tag{6.1}$$

MESA star allows the evolution of convective mixing during simulation, however, due to the 1D nature of the modeling, it is necessary to parameterize the convection to account for hydrodynamic mixing instabilities at convective boundaries. For this reason, after the MLT calculations have been performed, MESA star sets the overshoot mixing diffusion coefficient (D). In this work we use a step overshoot with constant diffusion coefficient (D)

$$D = \mathrm{overshoot}_{\mathrm{D0}} + \mathrm{overshoot}_{\Delta 0} \times \mathrm{D_{ob}}, \tag{6.2}$$

where $\mathrm{D_{ob}}$ is the convective diffusivity at the top (bottom) of the step overshooting region for inward (outward) overshooting. By default $\mathrm{overshoot}_{\Delta 0} = 1$.

Modeling massive stars is difficult due to the low gravitational binding and the tendency of their envelope to be unstable due to their high luminosities. As a result, it is necessary to pay special attention to the boundary conditions of the stellar atmosphere. MESA star assumes the plane parallel approximation, thus using M, R, and L in each cell can calculate the pressure (P_S) and temperature (T_S) at the top of the outermost cell. The calculation of P_S and T_S in MESA star can be done by different methods using two variables: $g = GM/R^2$ and $T_{\mathrm{eff}}^4 = L/4\pi\sigma_{\mathrm{SB}}R^2$. Also, it is important specify the optical depth τ_S to the base of the atmosphere, which by default is $\tau_S = 2/3$.

Artificial viscosity

We implemented artificial viscosity in our models to avoid numerical problems caused by shocks due to the hydrodynamic treatment. We use the folllowing form of the artificial viscosity pressure in MESA:

$$Q_i = C_Q P_i \left[\min \left(\frac{\Delta u}{(P_i V_i)^{1/2}} + \alpha, 0 \right) \right]^2, \tag{6.3}$$

where Q_i is the viscous pressure in zone i, $\Delta u = u_{i+1} - u_i$ is the relative velocity of two adjacent zones, P_i is the pressure, V_i is the specific volume. The quantity C_Q is the viscosity parameter, and α is the compression in units of sound speed. MESA defaults values are $C_Q = 4$, and $\alpha = 0.1$. For more details see Stellingwerf (1975).

6.3 Methodology

A common method used for 1D studies of CE events is to co-opted a stellar evolution code to model a lone primary star (commonly a giant star), and then to simulate the presence of an embedded companion by adding quantities such as heat, gravitational mass, and angular momentum at appropriate locations within the envelope (e.g. Ivanova, Justham & Podsiadlowski, 2015; Clayton et al., 2017, and references therein). In this work, we apply this method, using the hydrodynamical treatment available in version 15140 of MESA. In our simulations, we emulate the presence of an embedded binary companion within the envelope by injecting additional heat, which represents the frictional dissipation of the binary's orbital energy during a self regulated spiral-in. In figure 6.3, left-hand panel we show a schematic view of how the secondary star is moving into the CE during the slow spiral-in phase. The spiral-in phase begins when secondary is located at the base of the primary convective envelope (r_i), and the final orbital radius is taken to be r_f, which is the inner radius of the portion of the envelope into which the energy is injected. An illustration of this description is shown in Figure 6.3, right-hand panel.

We considered a range of time for deposition of this heat into the envelope as 10–1000 years, delimited by different physical factors like the slow spiral-in phase duration (see Ivanova et al., 2013). Because of the above, in our ejecting models we set the following variables:

1. Initial model of the star (M_i, v_{rot}, $R_{photosphere}$)

2. Injected Energy

3. $R_{photosphere}$ (Star's age) when injection of energy occurs.

4. Time in which energy is injected.
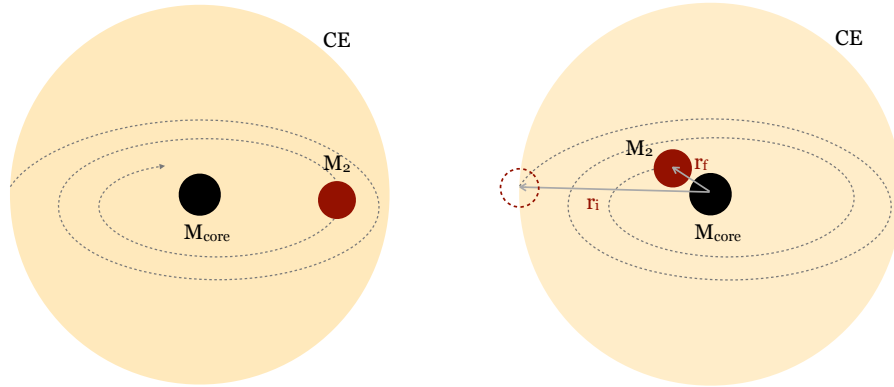
Figure 6.3: Schematic view during slow spiral-in phase. *Left panel*: Secondary star moving into CE. *Right panel*: Initial and final orbital radii (r_i and r_f, respectively) of secondary star.

5. Depth at which energy is injected.

6.3.1 Primary star

We can minimize the number of free parameters by setting the same initial model for each primary star. The initial model we use has been chosen to match as closely as possible to the progenitor star WR 124, that is 40 $M_\odot$ and 32 $M_\odot$ stars, being the estimated value and its lower limit for the initial mass of the WR star. The upper limit of the initial mass (48 $M_\odot$) was not counted due to numerical issues we had in version 15140 of MESA.

First, we evolved a metallicity of $Z = 0.02$[21] star of 32 $M_\odot$ from the zero-age main sequence (ZAMS). At the beginning of the simulation the initial rotation velocity rotation was 100 km s^{-1}. We selected a mixing length parameter, α_{MLT} = 1.95. The star's evolution when reached a radius of 300 $R_\odot$. We shall refer to this model as the "initial model", which serves as the starting point for all simulations reported. Figure 6.4 shows the track of initial model on a Hertzsprung-Russell diagram with a blue line.

Mass-loss treatment

Massive stars are so bright that radiation pressure on atmospheric spectral lines in the ultraviolet leads to mass-loss in a wind. For that reason, we used the wind mass-loss rate recipe from Vink (2017). Vink (2017) proposed that the wind mass-loss rate from stripped stars depends on the luminosity and metallicity of the star in the following way:

21 Z is the fraction of stellar mass which is made up of elements that are not hydrogen or helium.
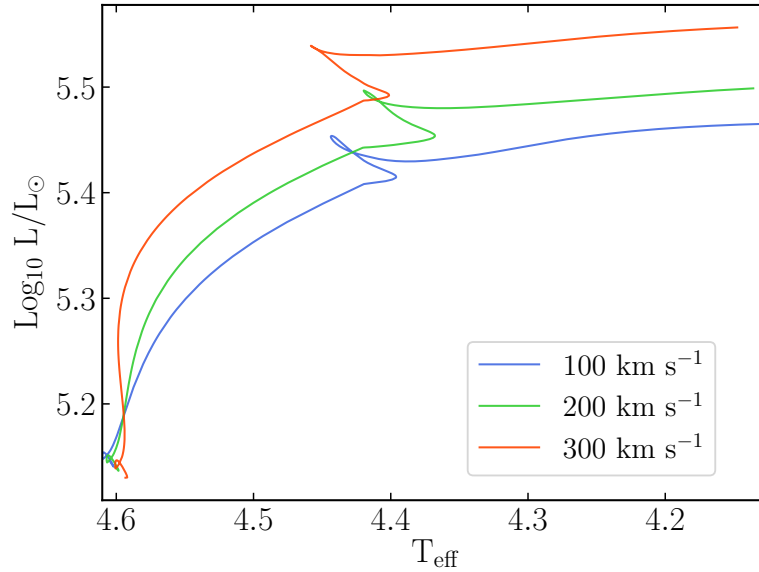
Figure 6.4: Evolutionary tracks of stars with initial mass of 32 $M_\odot$, with solar metallicity, for three different initial rotational velocities. Each model was calculated with version 15140 of MESA.

$$\log \dot{M} = -13.3 + 1.36\log(L/L_\odot) + 0.61\log(Z/Z_\odot) \tag{6.4}$$

6.3.2 Common envelope simulation

In our simulations there are only two energy sources, the star's existing nuclear heating and the added heat. We turn on the hydrodynamic scheme of MESA and we applied artificial viscosity in order to allow MESA to resolve hydrodynamic shocks; we use the default values of MESA (see Section 6.2.2). Additionally, during CE evolution in our models we implement an additional mass-loss recipe described below.

Convection is modeled with a mixing-length parameter $\alpha_{MLT} = 1.5$ and we also apply convective step overshooting with overshoot$_{D0}$ = 1.0 (see Equation 6.2) inside central convection zones. We adopt the Ledoux criterion (Ledoux, 1947) for convective stability.

In order to avoid numerical issues at the outer boundary (stellar surface) when the envelope has become extremely tenuous and optically thin, we relax the position of the outer boundary by changing the value of the optical depth from 2/3 (default value) to 20 (Clayton et al., 2017).

Heat

Heat is then added within a specified region of the envelope of our synthetic CE. In our models we add the extra energy in a portion of the convective envelope bounded by an inner radius (taken as a free parameter), and an outer edge at the top of convective zone. The energy is injected as follows:

1. The heat is injected at the same inner boundary throughout the duration of the simulation,

2. at a constant total rate per unit time,

3. and at a uniform rate per unit mass.

The rates at which we have added heat to the envelope are intended to simulate the slow spiral-in of a 1 $M_\odot$ companion. We can estimate the energy released from orbital decay when the secondary moves from an initial orbital radius r_i to a final orbit radius r_f by:

$$E_{\text{tot}} = GM_2\left(\frac{M_{\text{core}}}{r_f} - \frac{M_1}{r_i}\right),$$
(6.5)

where G is Newton's gravitational constant, and M_1 and M_2 are the masses of the primary and the secondary component, respectively. M_{core} is the mass of the primary core alone. Considering the spiral movement towards M_{core}, r_i and r_f are the initial and final distance of M_2 from M_{core}.

The question of how much energy we have available to inject in our models can be answered if we consider that the slow spiral-in phase begins when the secondary is located at the surface of the convective envelope and the final distance is taken to be the Roche limit of the secondary with respect to the primary core

$$R_{\text{Roche}} \approx R_2\left(\frac{M_1}{M_2}\right)^{1/3},$$
(6.6)

where R_2 is the radius of the secondary. For our particular case, typical values are: M_1 = 32 $M_\odot$, M_2 = 1 $M_\odot$, M_{core} = 3 $M_\odot$, R_2=1 $R_\odot$, r_i= 300 $R_\odot$, and r_f= 3.17 $R_\odot$. With these values we have available around 10^{48} erg before slow spiral-in ends. Considering a range of timescales between 10 and 1000 years for deposition of this extra energy into the envelope, we obtain energy deposition rates of between 10^{45}–10^{47} erg yr^{-1}.

Mass-loss treatment

In order to simulate dynamical mass-loss events in the evolution of our synthetic CE objects, in which matter is ejected from the stellar surface, we adopt the mass-loss

routine used by Clayton et al. (2017) to remove unbound material that is expanding at above the local escape velocity.

Basically this mass-loss routine identifies contiguous surfaces layers which exceed the local escape velocity at every cell, and then removes the material of those layers. For this work we considered the unbound mass (m) to decrease exponentially with a time constant of 0.01 years, that is:

$$\dot{M} = 100/\mathrm{yr}^{-1} \times m \tag{6.7}$$

This rate ensures that the timescale for mass removal is at least an order of magnitude below the dynamical and thermal timescales of the star and ensures numerical stability.

Pulsations

The growth rate of pulsations has been known to be the result of the increase of heating in CE simulations (e.g. Clayton et al., 2017; Ivanova, Justham & Podsiadlowski, 2015). Depending on the initial parameters of each simulation, the pulsations fall into the following regimes: Ejecting and Non-Ejecting cases. In the ejecting cases the pulsation amplitudes grow sufficiently large and the velocities are sufficiently supersonic so that the compression phases and accompanying shocks which occur are strong enough to dynamically eject shells of matter from the surface. The mass in these ejected shells is ignored in the simulation after it exceeds the escape velocity, and can be seen by changes in the remaining model mass and $\dot{M}$ evolution. On the other hand, non-ejecting cases correspond to pulsations that grow over multiple pulsation cycles until their amplitude is damped by nonlinear effects. Also, there are some cases where pulsations reach amplitudes large enough to launch ejections, but no ejections occur. In these cases, the shocks dissipate the energy of the pulsation and excite higher-order pulsations that then fade. The primary pulsation proceeds to grow once gain, resulting in stable repeating cycles.

In this way, we are looking for models in the ejecting case that are capable of reaching a mass-loss rate high enough to shield the dust formation region, that is $\dot{M} \geq 10^{-3} \, \mathrm{M}_\odot \, \mathrm{yr}^{-1}$ (Kochanek, 2011).

6.4 Results

We carried out simulations adding heat and implementing a hydrodynamic treatment as was described in Section 6.3.2 (Clayton et al., 2017). We stopped the initial primary star evolution when it reached a $\mathrm{R}_{\mathrm{photosphere}} = 300 \, \mathrm{R}_\odot$, which we take as our to have our starting point to inject the extra energy.

Table 6.1: Labels of the simulations described by the injected energy rate (E_{add}) and depth from which the energy is injected, R_{inj}.

|		E_{add} (erg yr^{-1})			
		10^{45}	10^{46}	10^{47}	10^{48}
	27	E_{r27}^{1e45}	-	-	-
R_{inj} ($R_\odot$)	30	-	E_{r30}^{1e46}	E_{r30}^{1e47}	E_{r30}^{1e48}
	120	-	E_{r120}^{1e46}	E_{r120}^{1e47}	E_{r120}^{1e48}
	200	-	E_{r200}^{1e46}	E_{r200}^{1e47}	-

6.4.1 Ceaseless energy injection

We removed time as a free parameter by injecting heat throughout the whole simulation, where each simulation lasted 600 years. For this set, we performed a grid of models to explore the effects of injecting different quantities of energy per year (E_{add}) and varying the depth from which the energy is injected (R_{inj}). Variation in values of R_{inj} and E_{add} were chosen to show a significant pulsation evolution. In Table 6.1 we show the simulations of this grid, and in Figure 6.5 we show the surface radii evolution of these models.

In Figure 6.5 we show representative models that allow us to explore the effects of varying R_{inj} and E_{add} when energy is injected during the whole simulation and primary star model is fixed. In Figure 6.5 we can see that large scale pulsations for some cases. The behaviour of these pulsations varies strongly with heating rate and R_{inj}. The growth rate of the pulsations increases with heating rate and can reach extremely high values.

Models in which the extra energy is equal to 10^{46} erg yr^{-1} (E_{r30}^{1e46}, E_{r120}^{1e46} and E_{r200}^{1e46}) were capable of generating pulsations when the energy is injected deeper (E_{r30}^{1e46}). For models with extra energy equal to 10^{47} erg yr^{-1}, the only one with high amplitude pulsations had an injection radius of 30 $R_\odot$ (E_{r30}^{1e47}), however, it had trouble converging when the simulation got to ∼300 years from the start of the power injection. The models with larger injection radius, 120 $R_\odot$ and 200 $R_\odot$, (E_{r120}^{1e47} and E_{r200}^{1e47} models, respectively) show an irregular pattern of pulsations with a small amplitude. The most energetic models, with $E_{add} = 10^{48}$ erg yr^{-1}, are not capable of converging and the simulation stops a few years after starting the injection of energy. The E_{r27}^{1e45} model was designed to explore pulsation formation at a greater depth and for a longer time, in this case we inject the energy for 700 years.

Top panel in figure 6.5 shows trends already noted by Clayton et al. (2017); we see
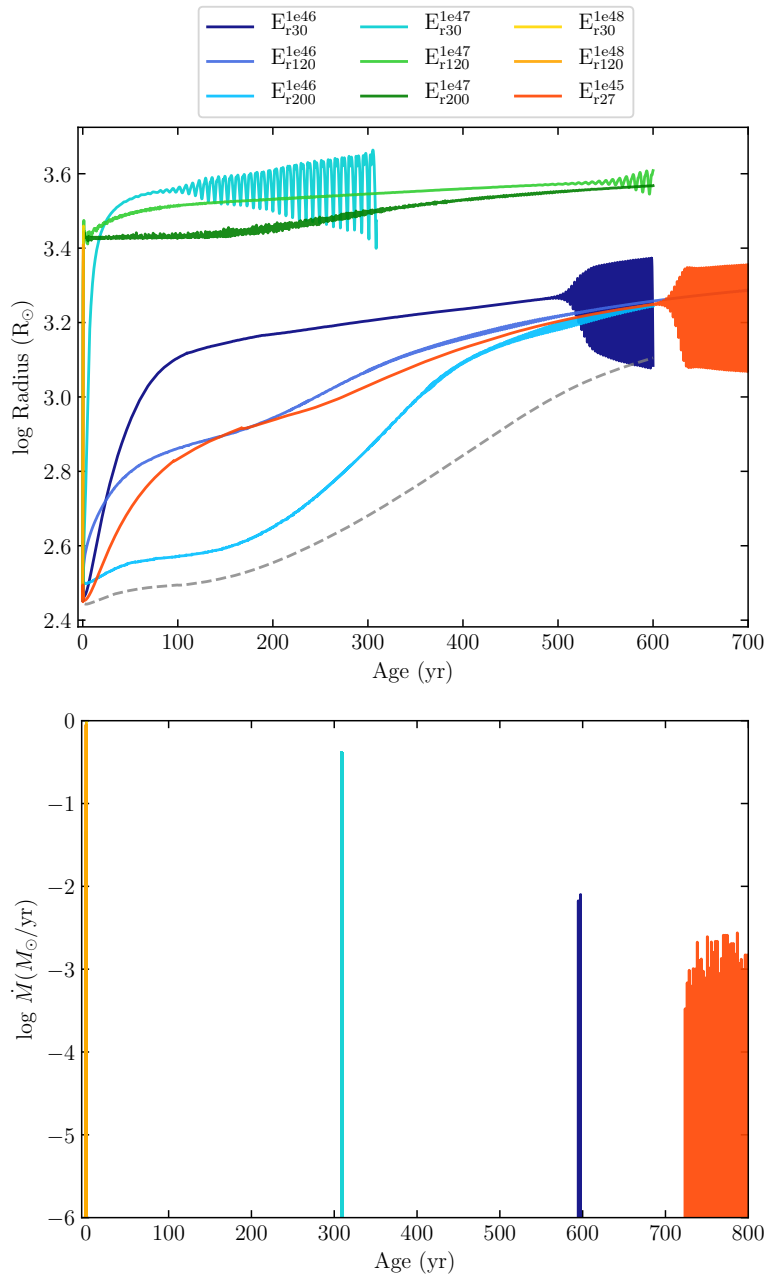
Figure 6.5: *Top panel:* Surface radii of a selection of hydrodynamical models in the uniform heating case, chosen as representative of the behaviours observed in these simulations. The figure shows models with different rate and depth at which the energy is injected into the envelope (see Table 6.1). Dashed gray line is the evolution of the primary without energy injection. *Bottom panel:* Mass loss rate evolution of the models in Table 6.1. The color code is the same in both panels.

that a lower energy deposition rate leads to a stable hydrodynamic model, with highest heating rates causing an accelerating expansion of the star that quickly reaches and exceeds escape velocity. A look at the evolution of mass-loss rate of these models (see the bottom panel in figure 6.5) allows us to distinguish those models in which ejections of material are present. In the bottom panel of the Figure 6.5 we can see that the E_{r30}^{1e47} and E_{r30}^{1e46} models exhibit an ejection of material before stopping, while the model E_{r27}^{1e45} shows successive ejections from ~ 710 years until the simulation ends. If we compare the top and bottom panels of Figure 6.5 it is remarkable that the ejections of material occur some years after the pulsations begin.

The lower energy model (E_{r27}^{1e45}) indicates that it is not essential to inject high energy to obtain pulses that generate mass ejections, if the injection of energy is very prolonged. Thus, it is possible that if we run the model E_{r30}^{1e46} for longer times we would be able to observe repeated ejections as in model E_{r27}^{1e45}.

Following the results of model E_{r27}^{1e45} (orange in Figure 6.5), we carried out a simulation with $E_{add} = 10^{46}$ at the same R_{inj} (27 $R_\odot$), E_{r27}^{1e46}. The left panel of the figure 6.6 allow us to see pulsations with large amplitudes. We can see in the right panel how these pulsations produce spirals in the HR diagram initially, but as the amplitude increases we can see the emergence of the characteristic shape seen in HR diagrams as the pulsation enters the nonlinear regime.

A brief explanation about the formation of this characteristic track in the HR diagram induced by pulsations is due to the values of minimum and maximum radius of each pulsation, as well as cooling process after pulsation reaches its maximum point, and the re-expansion process cause by return to hydrostatic equilibrium.

E_{r27}^{1e46} model present material ejections reaching mass-loss rates around 10^{-3} $M_\odot$ yr^{-1} in each pulsation. The mass ejected in this model is 1×10^{-2} $M_\odot$ throughout 200 years. In conclusion, to eject an amount of mass similar to that which makes up RCW 58 (~ 3 $M_\odot$, it is less massive that M 1-67) we need to inject energy for hundreds of years more.

6.4.2 Halted energy injection

The results of the previous subsection suggest that we need to inject energy continuously into the star's envelope in order to maintain large-amplitude pulsations capable to eject material. However, we are limited by time because slow spiral-in phase during the common envelope has a short duration ($\lesssim 1000$ yrs).

We design a grid of models to study the surface radius evolution in the case where we inject energy during a specific range of time. Representative models of this grid are present in Figure 6.7 and are described in Table 6.2. In these models, we stop the energy injection after 10, 50 and 100 years. We can see in Figure 6.7 that these injection times are not enough to produce oscillations and mass ejections.

Models with injected energy rate equal to 10^{47} erg yr^{-1} at $R_{inj} = 30$ $R_\odot$ expand rapidly
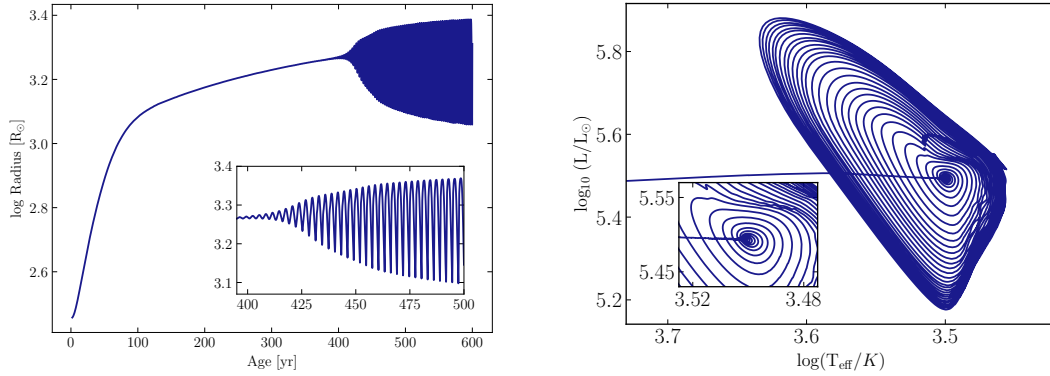
Figure 6.6: Evolution of the simulation with 1×10^{46} erg yr^{-1} at R_{inj} = 27 R$_\odot$. *Left panel:* Surface radius evolution. *Right panel:* Hertzsprung-Russell track plotted from 400 to 500 yrs after energy injection starts.

Table 6.2: Labels of the simulations described by the injected energy rate (E_{add}), depth from which the energy is injected R_{inj}, and time over which energy is injected.

| | | E_{add} (erg yr^{-1}), R_{inj} = 30 R$_\odot$ | |
		10^{46}	10^{47}
	10	$E_{r30,t10}^{1e46}$	$E_{r30,t10}^{1e47}$
t (yrs)	50	$E_{r30,t50}^{1e46}$	-
	100	$E_{r30,t100}^{1e46}$	$E_{r30,t100}^{1e47}$
		E_{add} (erg yr^{-1}), R_{inj} = 27 R$_\odot$	
		2×10^{46}	5×10^{46}
t (yrs)	100	$E_{r27,t100}^{2e46}$	$E_{r27,t100}^{5e46}$
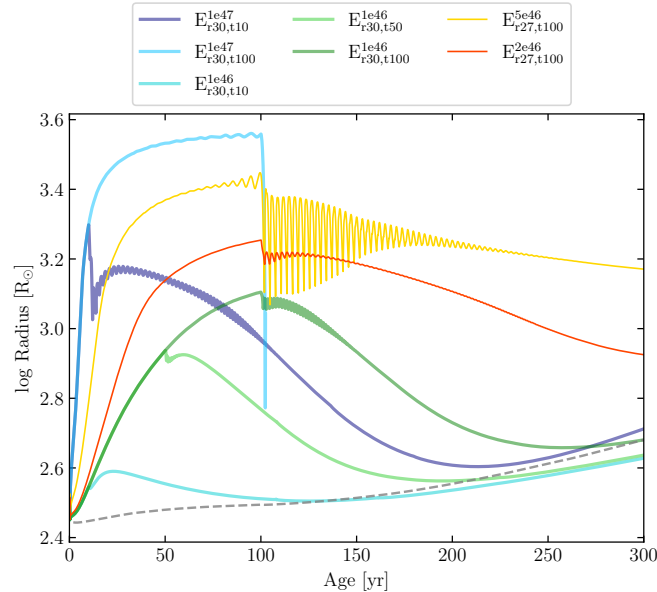
Figure 6.7: Surface radii of a selection of hydrodynamical models in the uniform heating case, chosen representative of the behaviours observed in these simulations. Figure shows models with different rates and depths at which the energy is injected into the envelope. Dashed gray line is the evolution of the primary without energy injection.

the envelope. In particular, model $E^{1e47}_{r30,t100}$ fails to converge at the end of ejection of energy. On the other hand, the radius evolution is almost unperturbed (compared with the evolution without extra energy added) when we feed the simulation with an injected energy rate equal to $E_{add} = 1 \times 10^{46}$ at the same depth for 10 years, model $E^{1e46}_{r30,t10}$. A special case is model $E^{5e46}_{r27,t100}$, because it is the only one that exhibits pulsations with high amplitude, although the physical condition of these pulsations are not enough to induce mass ejections.

In all models after the energy injection stops, the envelope contracts right at the end of the ejection and we can see small pulsations (except for one, model $E^{5e46}_{r27,t100}$) for a while. Finally, the evolution of the radius of the surface tries to follow the evolution of the star without injection of extra energy (dashed gray line in the figure 6.7).

Taking into account these results, we considered another alternative, stop the injection of energy once pulsations appear. So, we perform model $E^{5e46}_{r27,t250}$. This model injects energy at a rate of $E_{add} = 5 \times 10^{45}$ erg yr^{-1} to a depth of $R_{inj} = 27$ R$_\odot$ over 250 years. We can see the evolution of the surface radius and the mass in Figure 6.8. We note that once the injection of energy stops the envelope presents a small contraction and the pulsations succeed in inducing ejections for a while.

Model $E^{2e46}_{r27,t250}$ ejected around 0.175 M$_\odot$ in an elapsed time of $\sim$ 50 years, this gives us a mass loss rate average of around 10^{-3} M$_\odot$ yr^{-1}. Although the mass loss rate is
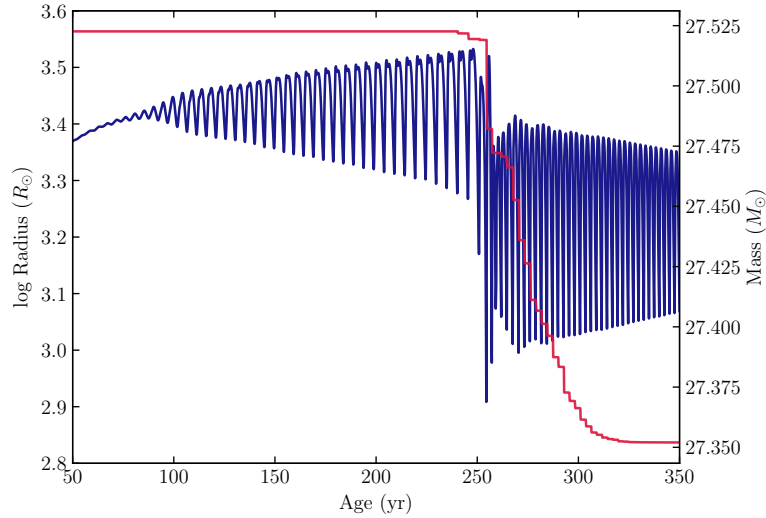
Figure 6.8: The surface radius (blue) and mass (red) evolution of a simulation with added energy equal to 5×10^{45} ergs yr^{-1} at R_{inj} = 27 $R_\odot$ which was being injected of energy during 250 years.

sufficient to shield the formation of dust, the mass ejected by the envelope is not enough to form a nebula like those studied in the previous chapters.

6.5 Recombination energy

The CE evolution process can release different kinds of energy into the envelope. Commonly, the energy released from orbital decay is used in models due to it being the largest reservoir of energy. Nevertheless, we look for other different sources of energy to contribute to induce the ejection of mass.

As the CE expands, its component material can cool below 10^5 K (during the spiral entry phase), making recombination energy a significant energy source during the evolution of the CE. This energy is what is released when a plasma recombines to form neutral atoms, so it is stored in the ionized gas of the stellar envelope (mainly in ionized hydrogen, ionized helium and doubly ionized helium).

During the CE evolution, the envelope mass is lost and the radius at which the recombination energy is significant gets smaller. Also, the internal layers start to expand looking for equilibrium. Then, considering that a giant star is capable of releasing around 10^{46} erg if the outer layers are enough cool to be ejected (Ivanova & Nandez, 2016; Ivanova, Justham & Podsiadlowski, 2015), we are interested in examining whether recombination energy can play an important role as an energy source in our models.

We examined one of our models to study the distribution of the ionized material. MESA code does not include the ionization state of each element. We used the Saha equation to calculate the different ionization states of hydrogen and helium in our models. The dominant contribution to the total recombination energy comes from hydrogen and helium. We can get from output files of MESA the hydrogen mass fraction (X), the helium mass fraction (Y), density (ρ), and the mean molecular weight per gas particle (μ) to calculate electron density (n_e). Then, we used the electron density and the temperature at every radius to calculate the Saha equation throughout the entire simulation (every timestep). In Figure 6.9 we show the distribution of the ionized hydrogen (top left), single and doubly ionized helium ratios (bottom panels) of our model E_{r30}^{1e46} (see Figure 6.5). We can note that the outer layers diminish the ionised material where the recombination can be significant, in particular during the pulsations. The top right panel in Figure 6.9 shows the doubly ionized helium ratio distribution versus the mass throughout the simulation measured from the surface.

The location of the region within the envelope in which recombination begins is important, to assess whether the energy released by this process can contribute significantly to the ejection of the envelope. Recombination energy becomes important to expand and eject the envelope when recombinations occur above the recombination radius (r_{rec}), this radius is (Ivanova & Nandez, 2016)

$$\frac{r_{rec}}{R_\odot} \gtrsim \frac{65 \, m_{grav}}{M_\odot} \tag{6.8}$$

where m_{grav} is the CE bounded gravitating mass, for our model E_{r30}^{1e46} the bounded mass is $\sim 27 \, M_\odot$. It is also important to consider that when recombination energy storage and release scales occur on dynamic time scales during expansions and contractions of the stellar envelope, recombination energy has a greater presence in the CE. In these circumstances, by not being able to transport the recombination energy by means of a radiative or convective flux, it becomes work, which pushes the envelope, contributing to the ejection of this (Ivanova, 2018).

Our interest is focused on observing the amount of mass found in the upper layers above the recombination region, since this would be the mass ejected if the recombination energy is greater than the binding energy (Ivanova & Nandez, 2016). In the top right panel of Figure 6.9 we can see that during pulsations recombination occurs in the region where the upper layers can reach a mass of up to 1 $M_\odot$, which allows us to suggest that if this energy could be included in the calculations of MESA we could obtain a higher rate of mass loss than that obtained with our previous models.
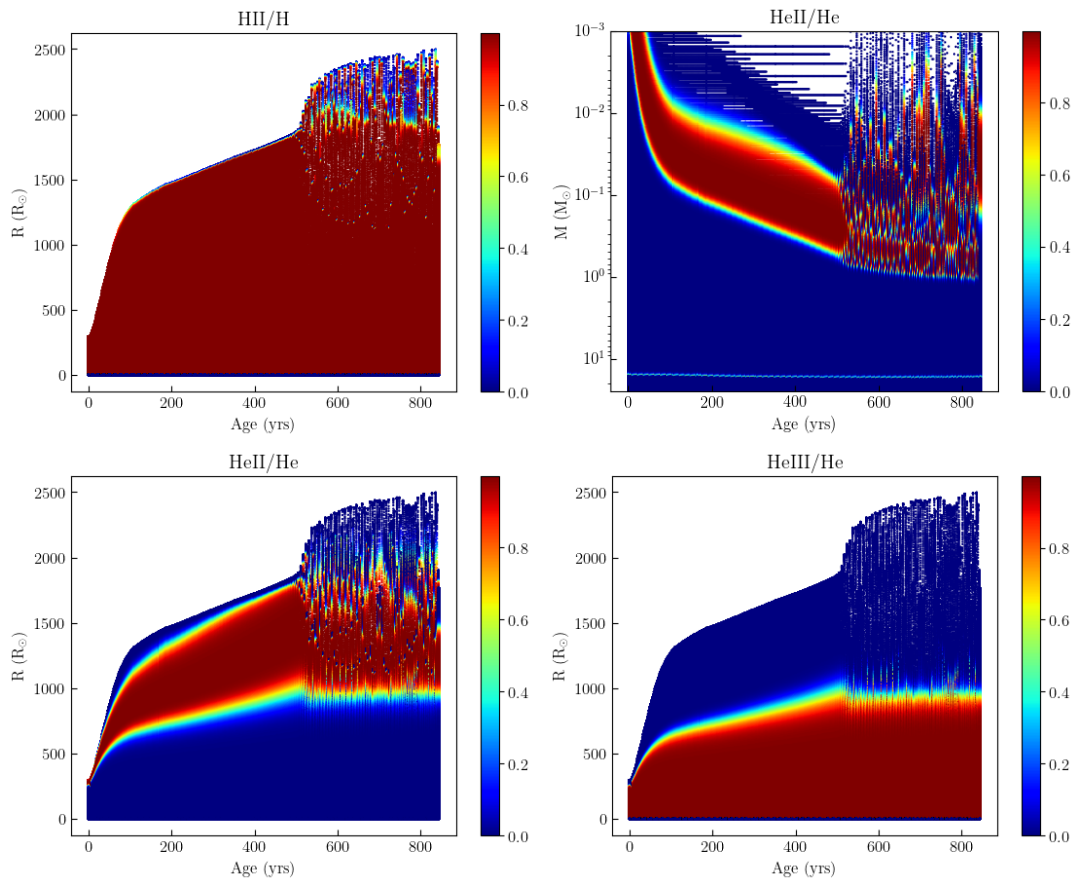
Figure 6.9: Distribution of ionized hydrogen, single and doubly ionized helium ratios of the synthetic CE during the Model E_{r30}^{1e46} simulation. The y-axis of the top right panel is measured from the envelope surface.

6.6 Discussion

Our MESA hydrodynamic simulations of a CE give us a broad view of how the production of pulsations and the subsequent ejection of the material depend on the injected energy rate and adopted depth at which the energy is injected. Although the injected energy rate into the star's envelope modulates the growth rate of the pulsations, it is not a linear effect. For example, increasing the injected energy rate does not ensure the generation of dynamic mass ejections. Furthermore, the radius at which the energy is injected amplifies the pulsations. We point out also that the time for which energy is injected plays an important role, we obtain pulsations with a prolonged injection of energy.

Previous works are based on low mass binary systems. Models in Clayton et al. (2017) present different timescales in which the pulsations appear; their models show pulsations at some decades after energy injection while our models need more time. They modelled a binary system integrated by a red giant of 1.6 $M_\odot$ with a companion of 0.3 $M_\odot$. While our system is composed of a primary star with an initial mass of 32 $M_\odot$ and a companion of 1 $M_\odot$.

We have not attempted to change the initial stellar model for one with a higher initial mass than our models present here (32 $M_\odot$). Another key parameter is the star's initial radius ($R_{photosphere}$) when the injection occurs, a more evolved star will have lower gravitational binding energy in its outer layers that could favour its ejection. In our model the ejection begins when the star has $R_{photosphere}$ = 300 $R_\odot$.

Model $E^{2e46}_{r27,t250}$ gave us an optimistic outlook to study the halted energy injection models in more detail. But, the study of recombination energy could provide new clues about the ejection of the envelope in a CE. Different works have found that recombination energy is not negligible as a source of energy in cases of low and intermediate mass stars. Ivanova & Nandez (2016) showed that in the case of the low-mass stars the recombination energy is significant and in some cases it is capable to eject the whole envelope by itself.

We point out the importance of timestep in our hydrodynamic simulations. It is necessary to use a small enough timestep in order to resolve pulsations and we required timestep on the order of days (Paxton et al., 2013; Clayton et al., 2017). The main consequence of a small time step is the large amount of time our models spend running, ranging from 12 to 36 hours, which means that a detailed study of parameter space is computationally expensive.

7   Conclusions & Future work

7.1 General conclusions

In this thesis we have shown that to obtain a good characterization of WR nebulae, gas and dust must be modelled simultaneously using a good representation of the stellar atmosphere. Our models are an improvement on those that simply model the dust emission in these nebulae without considering the presence of gas, as failure to do so may lead to incorrect flux estimates that cannot be reconciled with observations.

We found that the best photoionization model for the nebulae M 1-67 and RCW 58 requires the presence of dust with sizes as large as about 1 μm, which suggests an eruptive event with mass-loss rates as high as those postulated for LBV stars. However, our estimates of the initial masses of the progenitor stars do not reach the range of the stars that will become LBVs (60 $M_\odot$). Instead, we proposed a formation mechanism through a CE scenario that simultaneously creates the nebula and the WR star (Paczyński, 1976). This is consistent with the bipolar morphologies of these nebulae. However, we note that there is no observational evidence that WR 40 and WR 124 currently have a binary companion, although Toalá et al. (2018) suggested that their companions could be hiding in their dense winds.

We have resolved the star formation conundrum for WN8h, or at least for WR 40 and WR 124. Our results indicate that these stars have gone through a RSG stage and later evolved within a CE, where its binary companion failed to completely remove the hydrogen from its surface. That is, we suggest that the WN8h stars are products of the evolution of a binary system and are not an intermediate stage between an O-type star and the RSG/LBV stage.

In order to study the process under which a CE object can eject enough mass to produce the nebulae M 1-67 and RCW 58, we built models using the stellar evolution code MESA. We simulated a CE event during the spiral-in phase by injecting energy into the stellar envelope, which represents the frictional dissipation of the binary's orbital energy. According to the conditions of the energy injection, material ejections are generated. Our model in which 5×10^{45} erg yr^{-1} is injected to a considerable depth (27 $R_\odot$) inside the envelope for about 250 yrs, manages to generate a high rate of mass loss that could shield the dust regions during condensation ($\sim 10^{-3}$ M$_\odot$ yr^{-1}). However, the mass ejection time occurs for a little less than 100 yr, which does not allow the ejected material to be sufficient to form either of our already studied nebulae. However,

we intend to use this model as a basis to further investigate the evolution of CE objects that can originate a WR nebula.

In the following subsections a summary is given of the results obtained from the photoionization models of M 1-67 and RCW 58, and the stellar evolution models developed with MESA.

7.1.1 Summary of modelling for M 1-67

We have produced a self-consistent photionization model that fits IR photometry and spectra from *WISE*, *Spitzer* (IRS and MIPS), and *Herschel* (PACS and SPIRE) of M 1-67 , the nebula around WR 124. The CLOUDY photoionization code that we used allowed us to test different gas density distributions and dust grain-size distributions. The PYCLOUDY tool enable us to simulate the line emission and dust photometry through synthetic apertures corresponding to the different reference observations. Our principal findings are:

(i) The stellar atmosphere model 06-14 of the PoWR WNL grid that Hamann et al. (2006) found to be a good fit to the stellar spectrum of the central star, WR 124, is broadly consistent with the nebular optical and IR emission lines in our best model but underpredicts the intensities of high-ionization lines (see Section 4.4.1).

(ii) We require a two-shell structure in order to model the gas and dust emission. The inner region contains only gas and is required to reproduce the Hα surface brightness distribution and total emission. The outer shell contains both dust and gas and is needed to reproduce the 70-μm surface brightness profile and the dust temperature. The outer shell could correspond to the clumpy ring at 45 arcsec radius, which expands at 46 km s^{-1}. Both inner and outer shells have a power-law distribution of material (see Section 4.3.2).

(iii) The dust grain-size distribution resulting from our photoionization model consists of two populations of pure silicate grains. The first is an MRN power law with $a_{\mathrm{min}} = 0.005$ μm, $a_{\mathrm{max}} = 0.05$ μm, and power-law index $q = -3.5$. The second is a population of large grains with representative size $a_{\mathrm{big}} = 0.9$ μm, where the mass proportion between the big and small grain populations is $B/S = 20$. This is in stark contrast to the results of (Vamvatira-Nakou et al., 2016), who required much larger grains in their dust-only radiative transfer models, and highlights the role played by the nebular gas in the absorption of UV photons from hot stars (see Section 4.4.2).

(iv) We need a silicate grain mass fraction 16 timer higher than that of standard ISM dust in order to reach the flux of the infrared photometry. We suggest that non-spherical grains, whose absorption cross-sections are factors of 2 or more

higher than spherical grains of identical volume, could explain the discrepancy in the mass of dust and the chemical abundances of the grain material (see Section 4.4.2).

(v) The total dust mass in the nebula resulting from our photoionization model ($M_D = 0.22$ M$_\odot$) and the dust mass resulting from fitting and MBB model to the *Herschel* PACS and SPIRE photometry ($M_D = 0.36$ M$_\odot$) can be reconciled if the normalization parameter $\kappa_{v,0}$ takes into account the specific characteristics of the material in this WR nebula.

(vi) The maximum grain size $a_{big} = 0.9$ μm and the average mass-loss rate in the shell ejection $\dot{M} \sim 6 \times 10^{-4}$ M$_\odot$ yr^{-1} support an eruptive formation of M 1-67.

(vii) The estimated mass of photoionized gas in the nebula is $9.2^{+1.6}_{-1.5}$ M$_\odot$. Since M 1-67 is located high above the Galactic plane ($z \sim 370pc$), we can assume that the nebula consists almost entirely of material ejected from the central star, WR 124. Assuming that the current mass of WR 124 is 22 M$_\odot$ (Hamann et al., 2019), we estimate that its initial mass has to be > 40 M$_\odot$.

(viii) We propose that M 1-67 has been formed as a result of a CE ejection scenario, which easily explains the energetics and dust formation in the outer, dusty shell. This wound make M 1-67 and its progenitor star (WR 124) the first observational evidence of the post-CE evolution in massive stars.

7.1.2 Summary of modelling for RCW 58

We presented the analysis of the nebular and dust properties of RCW 58 around the WN8h star WR 40. The presence of extended IR emission along the line of sight hampers a global study of RCW 58. For this reason, we selected two clumps located towards the South of the nebula as representative for the dust properties of RCW 58 namely, LC and RC.

We used the photoionization code CLOUDY to produce synthetic optical, IR, and radio observations that were compared to publicly available data. We got the following results:

(i) Our models reproduced the derived nebular physical properties and the IR SED when using the WNL 06-13 stellar atmosphere model from POWR.

(ii) Our models required RCW 58 to be distributed into a ring-like structure (instead of a shell) with stratified gas and dust distributions. The total mass (gas + dust) in the RC and LC clumps are 0.027 and 0.173 M$_\odot$, respectively, with total D/G ratios of ~ 0.04 for both models.

(iii) Our cloudy model suggested a stratification of dust grains, with the smallest grains closer to the star and larger grains preferentially at the far-side of the clumps. We thoroughly discuss the different possibilities for the origin of such a distribution. It is very likely that a combination of a physical phenomena, such as gas-grain decoupling and the greater inertia of large grains, as well as grain shattering, produces the required dust distribution. The high dust-to-gas mass ratio predicted by our models could be ameliorated if non-spherical grains are present or if grain compositions other than silicates are also taken into consideration.

(iv) We found that the total mass of RCW 58 is $\approx$ 2.3 $\pm$ 1.7 $M_\odot$, relatively small compared to other WR nebulae. As a result, we estimated that the initial mass of WR 40 was $\approx 40^{+2}_{-3}$ $M_\odot$. Such small values for the mass of RCW 58 and predicted initial mass of WR 40 argue against and LBV evolution. However, our cloudy model requires dust as large as 0.9 μm, which can only form after an eruptive ejection of material with $\dot{M} > 10^{-3}$ $M_\odot$ yr^{-1}.

(v) We propose that RCW 58 formed through a CE channel producing simultaneously the observed WR nebula and giving birth to WR 40. This would make WR 124, to have been formed as a result of binary interaction, in particular a CE evolution. If this scenario is confirmed, WNh8 systems are possible candidates for future progenitors of gravitational waves.

7.1.3 Summary of modelling for stellar evolution

We presented a series of hydrodynamic models using stellar evolution code mesa to simulate CE objects that could represent the origins of RCW 58 and M 1-67. Our stellar evolutionary calculations work with a primary star of 32 $M_\odot$ undergoing a synthetic CE. We inject extra energy to the star's envelope during slow spiral-in phase (10–1000 years).

Orbital dissipatory heating present in our simulations cause the expansion of the envelope, in some cases the envelope become dynamically unstable and generate pulsations. These pulsations can have high amplitude into a supersonic regime. We treated shocks originate by strong compression with artificial viscosity in order to avoid numerical issues.

In certain models, mainly those in which the energy is injected deep into the envelope, the high amplitude compression can be strong enough to accelerate a star's outer layer to above escape velocity and dynamically it can be eject. Our models with uninterrupted injection of energy are capable to produce ejections of matter, however we don have enough time to eject an amount similar to that contained by RCW 58 (and M 1-67).

We propose models with halted energy injection, that is, we inject energy for a specific range of time. This study suggest exploring in more detail models where the

injection of energy stop once pulsations have formed. In addition, we suggest that recombination energy could be the second energy source to encourage the creation of pulsations capable of eject stellar material.

7.2 Future Work

The results obtained in this thesis based on theoretical models and observational data suggest various projects as future work. Below we list these future projects:

- The results presented in chapters 4 and 5 were interpreted assuming spherical silicate grains. Nowadays there are tools available which calculate physical properties such as opacities, that are needed to calculate dust emission with CLOUDY. Thus, we plan to study the effects of the implementation of different kinds of grains with varying optical properties and shapes (e.g. spheroidal grains).

- We have presented detailed modelling of M 1-67 and RCW 58 nebulae around two WNh8 stars, which we propose to have formed as the result of a CE channel. Another candidate is the runaway WN8h star WR 16 and its nebula (Marston et al., 1994), which was recently studied by Cichowolski et al. (2020) through archival IR and new Atacama Submillimeter Telescope Experiment (ASTE) molecular observations. Using simple fits to the IR photometry of the main shell around WR 16, these authors estimated a dust temperature of 65 K. This star appears to have had a complex interaction with the surrounding ISM and Cichowolski et al. (2020) postulate that it has experienced an LBV phase. We intend to perform more detailed modelling of this object in the future.

- In chapter 6, we develop an analysis of a synthetic CE using the stellar evolution code MESA. However, it is necessary explore the parameter space with more detail for these type of models. We are interested in performing a better simulation of a CE object.

Here we presented the exploration of the parameter space around the model described in Section 5.3.1 for LC. The χ^2 value of our best model was estimated to be 0.1191. We explored the effect on χ^2 of varying the hydrogen density n, the filling factor ϵ, and the size range of the big grains (a_{min} to a_{max}). Model examples are listed in Table A.1.

A first test was to reduce n to half of the value used for the best model in accordance with the range of values obtained from the analysis of the ATCA observations (top row in Table A.1). This model requires ϵ to increase by a factor of three to compensate for the mass. Retaining the same big grain size distribution, it was necessary to adjust D/G and B/S to fit the long wavelength part of the SED. The resultant fit was slightly worse than the best model.

Other test models, maintaining n, ϵ fixed but now changing a_{min} and a_{max}, were attempted and result in very similar fits to that of the model presented in the main text. D/G ratios are unchanged but we note a change in the big-to-small (B/S) ratio of $\lesssim 10$ per cent.

We note that small variations in the key parameters around our basic model produce very similar results but that our general conclusions are robust.

Table A.1: Test models to show the validity of our best model for LC. The parameters are normalized to the values obtained from our best model described in Section 6.4 and are labelled with the index 0.

Modified parameter	n [n_0]	ϵ [ϵ_0]	a_{min} [μm]	a_{max} [μm]	S2 [D/G]$_0$	S3 [D/G]$_0$	B/S	χ^2
n	0.5	3	0.6	0.9	0.6	0.7	1.11	0.5250
a_{min}	1	1	0.5	0.9	1	1	0.93	0.6355
a_{max}	1	1	0.6	1	1	1	1.07	0.5816
a_{min}, a_{max}	1	1	0.5	1	1	1	1	0.5624

Bibliography

Alūzas R., Pittard J. M., Hartquist T. W., Falle S. A. E. G., Langton R., 2012, MNRAS, 425, 2212. doi:10.1111/j.1365-2966.2012.21598.x

Andriesse C. D., 1974, A&A, 37, 257

Bailer-Jones C. A. L., Rybizki J., Fouesneau M., Mantelet G., Andrae R., 2018, AJ, 156, 58. doi:10.3847/1538-3881/aacb21

Banda-Barragán W. E., Brüggen M., Federrath C., Wagner A. Y., Scannapieco E., Cottle J., 2020, MNRAS, 499, 2173. doi:10.1093/mnras/staa2904

Banda-Barragán W. E., Brüggen M., Heesen V., Scannapieco E., Cottle J., Federrath C., Wagner A. Y., 2021, MNRAS, 506, 5658. doi:10.1093/mnras/stab1884

Beasor E. R., Davies B., 2018, MNRAS, 475, 55. doi:10.1093/mnras/stx3174

Bianchi S., Casasola V., Baes M., Clark C. J. R., Corbelli E., Davies J. I., De Looze I., et al., 2019, A&A, 631, A102. doi:10.1051/0004-6361/201936314

Biermann P., Harwit M., 1980, ApJL, 241, L105. doi:10.1086/183370

Bohannan B., 1997, ASPC, 120, 3

Cappa C. E., 2006, RMxAC, 26, 9

Cappa C. E., Goss W. M., Niemela V. S., Ostrov P. G., 1999, AJ, 118, 948. doi:10.1086/300995

Cassisi S., Potekhin A. Y., Pietrinferni A., Catelan M., Salaris M., 2007, ApJ, 661, 1094. doi:10.1086/516819

Cherchneff I., 2013, EAS, 60, 175. doi:10.1051/eas/1360020

Chiavassa A., Haubois X., Young J. S., Plez B., Josselin E., Perrin G., Freytag B., 2010, A&A, 515, A12. doi:10.1051/0004-6361/200913907

Chu Y.-H., 1981, ApJ, 249, 195. doi:10.1086/159275

Chu Y.-H., 1982, ApJ, 254, 578. doi:10.1086/159768

Cichowolski S., Duronea N. U., Suad L. A., Reynoso E. M., Noriega-Crespo A., Bronfman L., 2020, MNRAS, 495, 417. doi:10.1093/mnras/staa1153

Clayton M., Podsiadlowski P., Ivanova N., Justham S., 2017, MNRAS, 470, 1788. doi:10.1093/mnras/stx1290

Cohen M., Barlow M. J., 1975, ApL, 16, 165

Conti P. S., 1975, MSRSL, 9, 193

Cox J. P., Giuli R. T., 1968, pss..book

Crowther P. A., 2007, ARA&A, 45, 177. doi:10.1146/annurev.astro.45.051806.110615

Crowther P. A., Smith L. J., Hillier D. J., Schmutz W., 1995, A&A, 293, 427

De Donder E., Vanbeveren D., van Bever J., 1997, A&A, 318, 812

De Marco O., 2009, PASP, 121, 316. doi:10.1086/597765

de Mink S. E., Sana H., Langer N., Izzard R. G., Schneider F. R. N., 2014, ApJ, 782, 7. doi:10.1088/0004-637X/782/1/7

Delgado-Inglada G., Morisset C., Stasińska G., 2014, MNRAS, 440, 536. doi:10.1093/mnras/stu341

Draine B. T., 2003, ARA&A, 41, 241. doi:10.1146/annurev.astro.41.011802.094840

Draine B. T., 2011, ApJ, 732, 100. doi:10.1088/0004-637X/732/2/100

Dominik C., Tielens A. G. G. M., 1997, ApJ, 480, 647. doi:10.1086/303996

Ekström S., Georgy C., Eggenberger P., Meynet G., Mowlavi N., Wyttenbach A., Granada A., et al., 2012, A&A, 537, A146. doi:10.1051/0004-6361/201117751

Endo I., Lau R. M., Sakon I., Onaka T., Williams P. M., Shenavrin V. I., 2022, ApJ, 930, 116. doi:10.3847/1538-4357/ac63bd

Esteban C., Vilchez J. M., Smith L. J., Manchado A., 1991, A&A, 244, 205

Esteban C., Vilchez J. M., Smith L. J., Clegg R. E. S., 1992, A&A, 259, 629

Esteban C., Mesa-Delgado A., Morisset C., García-Rojas J., 2016, MNRAS, 460, 4038. doi:10.1093/mnras/stw1243

Fanciullo L., Kemper F., Scicluna P., Dharmawardena T. E., Srinivasan S., 2020, MNRAS, 499, 4666. doi:10.1093/mnras/staa2911

Ferland G. J., Chatzikos M., Guzmán F., Lykins M. L., van Hoof P. A. M., Williams R. J. R., Abel N. P., et al., 2017, RMxAA, 53, 385

Fernández-Martín A., Vílchez J. M., Pérez-Montero E., Candian A., Sánchez S. F., Martín-Gordón D., Riera A., 2013, A&A, 554, A104. doi:10.1051/0004-6361/201220773

Gail H.-P., Duschl W. J., Ferrarotti A. S., Weis K., 2005, ASPC, 332, 323

Garcia-Segura G., Mac Low M.-M., 1995, ApJ, 455, 160. doi:10.1086/176564

Georgy C., Ekström S., Meynet G., Massey P., Levesque E. M., Hirschi R., Eggenberger P., et al., 2012, A&A, 542, A29. doi:10.1051/0004-6361/201118340

Goldsmith K. J. A., Pittard J. M., 2018, MNRAS, 476, 2209. doi:10.1093/mnras/sty401

Gómez-González V. M. A., Rubio G., Toalá J. A., Guerrero M. A., Sabin L., Todt H., Gómez-Llanos V., et al., 2022, MNRAS, 509, 974. doi:10.1093/mnras/stab3042

Gómez-Llanos V., Morisset C., Szczerba R., García-Hernández D. A., García-Lario P., 2018, A&A, 617, A85. doi:10.1051/0004-6361/201731707

Gräfener G., Koesterke L., Hamann W.-R., 2002, A&A, 387, 244. doi:10.1051/0004-6361:20020269

Greenberg J. M., Li A., 1996, A&A, 309, 258

Grevesse N., Asplund M., Sauval A. J., Scott P., 2010, Ap&SS, 328, 179. doi:10.1007/s10509-010-0288-z

Grosdidier Y., Moffat A. F. J., Joncas G., Acker A., 1998, ApJL, 506, L127. doi:10.1086/311647

Gruendl R. A., Chu Y.-H., Dunne B. C., Points S. D., 2000, AJ, 120, 2670. doi:10.1086/316830

Gvaramadze V. V., Kniazev A. Y., Fabrika S., 2010, MNRAS, 405, 1047. doi:10.1111/j.1365-2966.2010.16496.x

Hamann W.-R., Gräfener G., Liermann A., 2006, A&A, 457, 1015. doi:10.1051/0004-6361:20065052

Hamann W.-R., Gräfener G., Liermann A., Hainich R., Sander A. A. C., Shenar T., Ramachandran V., et al., 2019, A&A, 625, A57. doi:10.1051/0004-6361/201834850

Han Z., Podsiadlowski P., Eggleton P. P., 1995, MNRAS, 272, 800. doi:10.1093/mnras/272.4.800

Henney W. J., Arthur S. J., 2019, MNRAS, 486, 4423. doi:10.1093/mnras/stz1130

Henning T., 2010, ARA&A, 48, 21. doi:10.1146/annurev-astro-081309-130815

Henyey L. G., Forbes J. E., Gould N. L., 1964, ApJ, 139, 306. doi:10.1086/147754

Henyey L., Vardya M. S., Bodenheimer P., 1965, ApJ, 142, 841. doi:10.1086/148357

Herald J. E., Hillier D. J., Schulte-Ladbeck R. E., 2001, ApJ, 548, 932. doi:10.1086/319007

Hirashita H., Il'in V. B., Pagani L., Lefèvre C., 2021, MNRAS, 502, 15. doi:10.1093/mnras/staa4018

Hirashita H., Yan H., 2009, MNRAS, 394, 1061. doi:10.1111/j.1365-2966.2009.14405.x

Iaconi R., Maeda K., De Marco O., Nozawa T., Reichardt T., 2019, MNRAS, 489, 3334. doi:10.1093/mnras/stz2312

Iaconi R., Maeda K., Nozawa T., De Marco O., Reichardt T., 2020, MNRAS, 497, 3166. doi:10.1093/mnras/staa2169

Iaconi R., Reichardt T., Staff J., De Marco O., Passy J.-C., Price D., Wurster J., et al., 2017, MNRAS, 464, 4028. doi:10.1093/mnras/stw2377

Ivanova N., 2002, PhDT

Ivanova N., 2018, ApJL, 858, L24. doi:10.3847/2041-8213/aac101

Ivanova N., Justham S., Chen X., De Marco O., Fryer C. L., Gaburov E., Ge H., et al., 2013, A&ARv, 21, 59. doi:10.1007/s00159-013-0059-2

Ivanova N., Justham S., Podsiadlowski P., 2015, MNRAS, 447, 2181. doi:10.1093/mnras/stu2582

Ivanova N., Nandez J. L. A., 2016, MNRAS, 462, 362. doi:10.1093/mnras/stw1676

Izzard R. G., Hall P. D., Tauris T. M., Tout C. A., 2012, IAUS, 283, 95. doi:10.1017/S1743921312010769

Jiménez-Hernández P., Arthur S. J., Toalá J. A., 2020, MNRAS, 497, 4128. doi:10.1093/mnras/staa2272

Jiménez-Hernández P., Arthur S. J., Toalá J. A., Marston A. P., 2021, MNRAS, 507, 3030. doi:10.1093/mnras/stab2332

Jones A. P., Tielens A. G. G. M., Hollenbach D. J., 1996, ApJ, 469, 740. doi:10.1086/177823

Kamiński T., 2019, A&A, 627, A114. doi:10.1051/0004-6361/201935408

Kashi A., Soker N., 2010, arXiv, arXiv:1011.1222

Kervella P., Perrin G., Chiavassa A., Ridgway S. T., Cami J., Haubois X., Verhoelst T., 2011, A&A, 531, A117. doi:10.1051/0004-6361/201116962

Kessler M. F., Steinz J. A., Anderegg M. E., Clavel J., Drechsel G., Estaria P., Faelker J., et al., 1996, A&A, 315, L27

Kirchschlager F., Schmidt F. D., Barlow M. J., Fogerty E. L., Bevan A., Priestley F. D., 2019, MNRAS, 489, 4465. doi:10.1093/mnras/stz2399

Kochanek C. S., 2011, ApJ, 743, 73. doi:10.1088/0004-637X/743/1/73

Kruegel E., 2003, pid..book

Kwitter K. B., 1984, ApJ, 287, 840. doi:10.1086/162742

Langer N., 1995, IAUS, 163, 15

Langer N., 2012, ARA&A, 50, 107. doi:10.1146/annurev-astro-081811-125534

Laplace E., Götberg Y., de Mink S. E., Justham S., Farmer R., 2020, A&A, 637, A6. doi:10.1051/0004-6361/201937300

Lau R. M., Eldridge J. J., Hankins M. J., Lamberts A., Sakon I., Williams P. M., 2020, ApJ, 898, 74. doi:10.3847/1538-4357/ab9cb5

Ledoux P., 1947, ApJ, 105, 305. doi:10.1086/144905

Lesaffre P., Han Z., Tout C. A., Podsiadlowski P., Martin R. G., 2006, MNRAS, 368, 187. doi:10.1111/j.1365-2966.2006.10068.x

Lü G., Zhu C., Podsiadlowski P., 2013, ApJ, 768, 193. doi:10.1088/0004-637X/768/2/193

Luri X., Brown A. G. A., Sarro L. M., Arenou F., Bailer-Jones C. A. L., Castro-Ginard A., de Bruijne J., et al., 2018, A&A, 616, A9. doi:10.1051/0004-6361/201832964

Luridiana V., Morisset C., Shaw R. A., 2015, A&A, 573, A42. doi:10.1051/0004-6361/201323152

Maeder A., Meynet G., 2000, A&A, 361, 159

Marchenko S. V., Moffat A. F. J., Crowther P. A., 2010, ApJL, 724, L90. doi:10.1088/2041-8205/724/1/L90

Marston A. P., 1991, ApJ, 366, 181. doi:10.1086/169550

Marston A. P., Yocum D. R., Garcia-Segura G., Chu Y.-H., 1994, ApJS, 95, 151. doi:10.1086/192097

Mason B. D., Hartkopf W. I., Gies D. R., Henry T. J., Helsel J. W., 2009, AJ, 137, 3358. doi:10.1088/0004-6256/137/2/3358

Mathis J. S., Cassinelli J. P., van der Hucht K. A., Prusti T., Wesselius P. R., Williams P. M., 1992, ApJ, 384, 197. doi:10.1086/170863

Mathis J. S., Rumpl W., Nordsieck K. H., 1977, ApJ, 217, 425. doi:10.1086/155591

McMullin J. P., Waters B., Schiebel D., Young W., Golap K., 2007, ASPC, 376, 127

Méndez-Delgado J. E., Esteban C., García-Rojas J., Arellano-Córdova K. Z., Valerdi M., 2020, MNRAS, 496, 2726. doi:10.1093/mnras/staa1705

Merrill P. W., 1938, PASP, 50, 350. doi:10.1086/124982

Minkowski R., 1946, PASP, 58, 305. doi:10.1086/125855

Moffat A. F. J., Isserstedt J., 1980, A&A, 91, 147

Morisset C., 2006, IAUS, 234, 467. doi:10.1017/S1743921306003772

Morris P. W., Gull T. R., Hillier D. J., Barlow M. J., Royer P., Nielsen K., Black J., et al., 2017, ApJ, 842, 79. doi:10.3847/1538-4357/aa71b3

Neugebauer G., Habing H. J., van Duinen R., Aumann H. H., Baud B., Beichman C. A., Beintema D. A., et al., 1984, ApJL, 278, L1. doi:10.1086/184209

Nota A., 1999, LNP, 62. doi:10.1007/BFb0106356

Nota A., Clampin M., Sirianni M., Greenfield P., Golimowski D. A., 1995, IAUS, 163, 78

Onaka T., de Jong T., Willems F. J., 1989, A&A, 218, 169

Ossenkopf V., Henning T., Mathis J. S., 1992, A&A, 261, 567

Paczynski B., 1976, IAUS, 73, 75

Parker Q. A., Phillipps S., Pierce M. J., Hartley M., Hambly N. C., Read M. A., MacGillivray H. T., et al., 2005, MNRAS, 362, 689. doi:10.1111/j.1365-2966.2005.09350.x

Paxton B., Bildsten L., Dotter A., Herwig F., Lesaffre P., Timmes F., 2011, ApJS, 192, 3. doi:10.1088/0067-0049/192/1/3

Paxton B., Cantiello M., Arras P., Bildsten L., Brown E. F., Dotter A., Mankovich C., et al., 2013, ApJS, 208, 4. doi:10.1088/0067-0049/208/1/4

Paxton B., Marchant P., Schwab J., Bauer E. B., Bildsten L., Cantiello M., Dessart L., et al., 2015, ApJS, 220, 15. doi:10.1088/0067-0049/220/1/15

Paxton B., Schwab J., Bauer E. B., Bildsten L., Blinnikov S., Duffell P., Farmer R., et al., 2018, ApJS, 234, 34. doi:10.3847/1538-4365/aaa5a8

Perek L., Kohoutek L., 1967, BAICz, 18, 252

Pilbratt G. L., Riedinger J. R., Passvogel T., Crone G., Doyle D., Gageur U., Heras A. M., et al., 2010, A&A, 518, L1. doi:10.1051/0004-6361/201014759

Pittard J. M., Parkin E. R., 2016, MNRAS, 457, 4470. doi:10.1093/mnras/stw025

Podsiadlowski P., Joss P. C., Hsu J. J. L., 1992, ApJ, 391, 246. doi:10.1086/171341

Podsiadlowski P., Ivanova N., Justham S., Rappaport S., 2010, MNRAS, 406, 840. doi:10.1111/j.1365-2966.2010.16751.x

Podsiadlowski P., Rappaport S., King A. R., D'Antona F., Burderi L., 2001, ASPC, 229

Ramiaramanantsoa T., Ignace R., Moffat A. F. J., St-Louis N., Shkolnik E. L., Popowicz A., Kuschnig R., et al., 2019, MNRAS, 490, 5921. doi:10.1093/mnras/stz2895

Rate G., Crowther P. A., 2020, MNRAS, 493, 1512. doi:10.1093/mnras/stz3614

Reyes-Pérez J., Morisset C., Peña M., Mesa-Delgado A., 2015, MNRAS, 452, 1764. doi:10.1093/mnras/stv1423

Rogers F. J., Nayfonov A., 2002, ApJ, 576, 1064. doi:10.1086/341894

Rosa M. R., Mathis J. S., 1990, ASPC, 7, 135

Rubio G., Toalá J. A., Jiménez-Hernández P., Ramos-Larios G., Guerrero M. A., Gómez-González V. M. A., Santamaría E., et al., 2020, MNRAS, 499, 415. doi:10.1093/mnras/staa2837

Sana H., de Mink S. E., de Koter A., Langer N., Evans C. J., Gieles M., Gosset E., et al., 2012, Sci, 337, 444. doi:10.1126/science.1223344

Schmutz W., Hamann W.-R., Wessolowski U., 1989, A&A, 210, 236

Scicluna P., Siebenmorgen R., Wesson R., Blommaert J. A. D. L., Kasper M., Voshchinnikov N. V., Wolf S., 2015, A&A, 584, L10. doi:10.1051/0004-6361/201527563

Siebenmorgen R., Voshchinnikov N. V., Bagnulo S., 2014, A&A, 561, A82. doi:10.1051/0004-6361/201321716

Sirianni M., Nota A., Pasquali A., Clampin M., 1998, A&A, 335, 1029

Slavin J. D., Dwek E., Mac Low M.-M., Hill A. S., 2020, ApJ, 902, 135. doi:10.3847/1538-4357/abb5a4

Smith N., 2014, ARA&A, 52, 487. doi:10.1146/annurev-astro-081913-040025

Smith L. F., Batchelor R. A., 1970, AuJPh, 23, 203. doi:10.1071/PH700203

Smith J. D. T., Armus L., Dale D. A., Roussel H., Sheth K., Buckalew B. A., Jarrett T. H., et al., 2007, PASP, 119, 1133. doi:10.1086/522634

Smith L. F., Aller L. H., 1969, ApJ, 157, 1245. doi:10.1086/150151

Smith L. J., Pettini M., Dyson J. E., Hartquist T. W., 1984, MNRAS, 211, 679. doi:10.1093/mnras/211.3.679

Smith L. J., Pettini M., Dyson J. E., Hartquist T. W., 1988, MNRAS, 234, 625. doi:10.1093/mnras/234.3.625

Smith L. F., Shara M. M., Moffat A. F. J., 1996, MNRAS, 281, 163. doi:10.1093/mnras/281.1.163

Solf J., Carsenty U., 1982, A&A, 116, 54

St-Louis N., Sévigny M., Drissen L., Martin T., 2017, IAUS, 329, 446. doi:10.1017/S1743921317003155

Steffen W., Koning N., Wenger S., Morisset C., Magnor M., 2011, ITVCG, 17, 454. doi:10.1109/TVCG.2010.62

Stellingwerf R. F., 1975, ApJ, 195, 441. doi:10.1086/153343

Stock D. J., Barlow M. J., 2010, MNRAS, 409, 1429. doi:10.1111/j.1365-2966.2010.17124.x

Stock D. J., Barlow M. J., Wesson R., 2011, MNRAS, 418, 2532. doi:10.1111/j.1365-2966.2011.19643.x

Tamanai A., Pucci A., Dohmen R., Gail H.-P., 2017, ApJ, 845, 6. doi:10.3847/1538-4357/aa7d08

Temi P., Marcum P. M., Young E., Adams J. D., Adams S., Andersson B.-G., Becklin E. E., et al., 2014, ApJS, 212, 24. doi:10.1088/0067-0049/212/2/24

Tielens A. G. G. M., Allamandola L. J., 1987, ASSL, 134, 397. doi:10.1007/978-94-009-3861-8_16

Toalá J. A., Oskinova L. M., Hamann W.-R., Ignace R., Sander A. A. C., Shenar T., Todt H., et al., 2018, ApJL, 869, L11. doi:10.3847/2041-8213/aaf39d

Toalá J. A., Arthur S. J., 2011, ApJ, 737, 100. doi:10.1088/0004-637X/737/2/100

Toalá J. A., Guerrero M. A., Ramos-Larios G., Guzmán V., 2015, A&A, 578, A66. doi:10.1051/0004-6361/201525706

Ueta T., Meixner M., 2003, ApJ, 586, 1338. doi:10.1086/367818

Usov V. V., 1991, MNRAS, 252, 49. doi:10.1093/mnras/252.1.49

Vamvatira-Nakou C., Hutsemékers D., Royer P., Waelkens C., Groenewegen M. A. T., Barlow M. J., 2016, A&A, 588, A92. doi:10.1051/0004-6361/201527667

van Buren D., McCray R., 1988, ApJL, 329, L93. doi:10.1086/185184

van den Heuvel E. P. J., Heise J., 1972, NPhS, 239, 67. doi:10.1038/physci239067a0

Verhoelst T., van der Zypen N., Hony S., Decin L., Cami J., Eriksson K., 2009, A&A, 498, 127. doi:10.1051/0004-6361/20079063

Vink J. S., 2017, A&A, 607, L8. doi:10.1051/0004-6361/201731902

Vink J. S., Gräfener G., 2012, ApJL, 751, L34. doi:10.1088/2041-8205/751/2/L34

Wachter S., Mauerhan J. C., Van Dyk S. D., Hoard D. W., Kafka S., Morris P. W., 2010, AJ, 139, 2330. doi:10.1088/0004-6256/139/6/2330

Weis K., 2001, RvMA, 14, 261

Weingartner J. C., Draine B. T., 2001, ApJ, 548, 296. doi:10.1086/318651

Wellstein S., Langer N., Braun H., 2001, A&A, 369, 939. doi:10.1051/0004-6361:20010151

Werner M. W., Roellig T. L., Low F. J., Rieke G. H., Rieke M., Hoffmann W. F., Young E., et al., 2004, ApJS, 154, 1. doi:10.1086/422992

Whittet D. C. B., 2003, dge..conf

Williams P. M., 2019, MNRAS, 488, 1282. doi:10.1093/mnras/stz1784

Wilson T. L., Rohlfs K., Hüttemeister S., 2009, tra..book. doi:10.1007/978-3-540-85122-6

Wright E. L., Eisenhardt P. R. M., Mainzer A. K., Ressler M. E., Cutri R. M., Jarrett T., Kirkpatrick J. D., et al., 2010, AJ, 140, 1868. doi:10.1088/0004-6256/140/6/1868

Young E. T., Becklin E. E., Marcum P. M., Roellig T. L., De Buizer J. M., Herter T. L., Güsten R., et al., 2012, ApJL, 749, L17. doi:10.1088/2041-8205/749/2/L17

Zavala S., Toalá J. A., Santamaría E., Ramos-Larios G., Sabin L., Quino-Mendoza J. A., Rubio G., et al., 2022, MNRAS.tmp. doi:10.1093/mnras/stac1097

Zubko V. G., Krełowski J., Wegner W., 1996, MNRAS, 283, 577. doi:10.1093/mnras/283.2.577

Declaration of Authorship

I hereby declare that this thesis is my own unaided work. All direct or indirect sources used are acknowledged as references.

Morelia, September 22, 2022   _____

Palmira Jiménez Hernández